Optical and Electrical Properties of Metal-Polymer Nanocomposites Prepared by Vapor-Phase Co-evaporation

Dissertation

Zur Erlangung des akademischen Grades
Doktor der Ingenieurwissenschaften
(Dr.-Ing.)
der Technischen Fakultät
der Christian-Albrechts-Universität zu Kiel

Haile Takele

Kiel
2008

1. Gutachter:	Prof. Dr. Franz Faupel
2. Gutachter:	Prof. Dr. Wolfgang Jäger
Datum der mündlichen Prüfung:	14.03.2008

Acknowledgments

In this page, I would like to express my deep gratitude to many people who contributed through their support, experience and friendship in the work described in this thesis.

First and foremost, my sincerest acknowledgment and gratitude to Prof. Dr. Franz Faupel for giving me the opportunity to work in his group, and allowing me to perform interesting research.

Particular thanks to Dr. Vladimir Zaporojtchenko for his guidance and support throughout my research. This dissertation would never come to pass without his patience, enthusiasm, and encouragement. I greatly appreciate his planning and direction in those early years and helpful discussions through out my work.

I would like to express my especial gratefulness to Dipl.-Ing. Stefan Rehders for constructing the deposition chamber and for his expertise in solving technical problems; Thank you for your helpfulness. Dipl.-Ing. Rainer Kloth for fast computer problem solving.

For their specific contributions to the work contained herein during characterization and paper review, hearty, I thank Dr. Ulrich Schürmann, Dipl.-Ing. Henry Greve, Dipl.-Ing. Christian Hanisch, M.Sc. Venkata Sai Kiran Chakravadhanula, M.Sc. Seid Jebril, M.Sc. Amit Kulkarni, M.Sc. Mady Elbahri, Dr. Thomas Strunskus, Dipl.-Min. Marlies Schwitzke, Dr. Jörn Kanzow, and Dr. Yurgita Zekonyte.

Many thanks to Dr. Klaus Rätzke, Prof. Dr. Rainer Adelung, Dipl.-Geol. Beate Minten, and Dipl.-Chem. Sieglinde Kastaun. Moreover, I would like to extend my sincere appreciation to the current and former group members, Dipl.-Ing. Sebastian Wille, Msc. Michael Scharnberg, M.Sc. Muhammad Qasim Shaikh, Dipl.-Phys. Tomislav Hrkac, Dipl.-Ing. Jan Kruse, Dipl.-Ing. Alexander Bartsch, Dipl.-Chem. Kai Dolgner, Dr. Abhijit Biswas, Dr. Rainer Kunz, and Dr. Jörn Erichsen.

Certainly, I greatly appreciate the financial support extended to me by the German Research Foundation (DFG). Thank you Deutchland!!!

Finally and firstly, this dissertation is dedicated to my wife Teje Amisalu, whose love, hard work, and trust have made the last four years a joy; and, to our

child Rahel Haile, who made our life relentlessly enjoyable since the middle of my PhD work. Finally I express my deep gratitude to my father Takele Beyene and my mother Yalga Tadesse for the support over the years. Hearty thanks to Mr. Beyene Aleme for his support and Priest Birhanemeskel Tedla.

Contents

1 Introduction

Nanostructures are functional structures with at least one characteristic dimension being between $1\,nm$ and $100\,nm$. Such materials and systems can be designed to exhibit novel and significantly improved physical, chemical and biological properties as a result of the limited size of their constituent particles or molecules. Nowadays, there are different types of nanostructured materials and systems essentially differing in the number of dimensions which lie within the nanometer range: such as systems confined to one dimension (nanofilms, nanolayers), systems confined to two dimensions (nanowires, nanorods, nanocolumns, nanotubes), and systems confined to three dimensions (nanoclusters of different shapes).

The term "nanocomposites" has been used to identify a class of materials having a microstructural base where one constituent is interspersed in the matrix of the other. The most typical examples are inhomogeneous materials consisting of a dispersion of nanoparticles (metals, semiconductors, magnetic materials) in an insulating matrix such as polymers, ceramics, and glasses. These materials have been found to be biphasic without or weak chemical bonds between the two components. Such composite systems have significant optical and electrical properties that depend on the doping level of the composite material and the matrix structure.

In the last two decades, nanocomposite films consisting of metal nanoparticles dispersed in a matrix of insulating materials such as polymers, ceramics or glasses have generated an increasing interest as an advanced technological materials because of their unique physical properties. Such nanocomposites can be used as a material for novel functional applications in optics [1], electronics [2], magnetics [3], medicine [4], etc.

When a nanocomposite containing metallic nanoclusters (typically, Au, Ag,

and Cu) is exposed to light, they exhibit a strong absorption maximum at a particular wavelength due to a photon induced oscillation of electron charge density (Surface Plasmon) [5, 6]. The excitation of the surface plasmon is found to be an extinction maximum or transmission minimum. The spectral position, the relative intensity, and the bandwidth (full width at half maximum) of the plasmon band depend on the dielectric properties of the metal and the surrounding medium, the amount of particles in the composite film, particle size and shape, particle-particle interactions and the distribution of the particles inside the insulating material [6–8]. The sensitivity of the surface plasmon band for small variations of these parameters contributes to the application of the nanocomposites in various areas such as color filters [9–11], optical switching and optical limiting devices [12], optical and biosensors [13, 14], absorption elements of the solar cells [15], photonic bandgap tuning [16], Bragg reflectors [17, 18], and surface enhanced Raman spectroscopy [19].

Polymer based nanocomposite materials show great promise as they can provide the necessary stability and processability for these important applications. The general principles in the construction of optical composites involve the mixing of optically functional materials within a processable matrix. Thus, noble metal-polymer composites are interesting materials to produce optically and electrically active media. Polymers are particularly attractive as the host of the metal nanoparticles to stabilize the particle size. They are generally low-cost materials, versatile, and can be easily processed into thin films. The linear optical properties (extinction, absorption, and scattering of light) and the electrical conductivity of the composites are strongly related to their microstructure [11, 12].

The fundamental motivation of this research is based on the dramatic change in the physical properties of polymer composites containing noble metal nanoclusters and their use for functional applications in optics and electronics. Therefore, the research was focused on the development of a well controlled synthesis of polymer/metal nanocomposite thin films and the study of the optical and electrical properties of these composites.

The dissertation is organized into eight chapters including this one. Chapter 2 introduces the basic theories about the optical and electrical properties of

metallic nanoparticles. In chapter 3 the methods for vapor phase deposition of metals and polymers are described as well as the nanoparticle preparation in the polymer matrix by co-evaporation, which was used extensively in this work. In chapter 4, the methods developed and the basic principles of the techniques used to characterize the morphology, the chemical and physical properties of composite films are demonstrated.

The following three chapters include experimental results and discussion. The nucleation and growth of metallic nanoclusters in various polymers prepared by co-evaporation are presented in chapter 5. Chapter 6 and 7 describe the most important obtained results in optical and electrical properties of metallic nanoparticles in polymers, respectively. The last chapter 8 concludes the dissertation with a summary of the principal results and a brief discussion of the experiments.

The unique contribution of the work described in this dissertation are the following:

- Successful preparation of polymer composites containing metallic nanoparticles by vapor phase co-evaporation technique. Simultaneous deposition of metal atoms and polymer molecules evaporated from two independent sources were used to produce monometallic polymer composites. In addition, from both the scientific and technological views, bimetallic nanoparticles are of great interest due to the potential application of the plasmonic properties of the particles. To my knowledge, the unique preparation of bimetallic nanoparticles in polymers prepared by simultaneous deposition of two different metal atoms and polymer molecules from three independent sources is presented in this work for the first time.

- A new strategy was developed in order to determine the volume percentage of metal nanoparticles in the composite film. The physical properties exhibited by the composite film are mainly described in terms of the amount of metal nanoparticles in the composite film which requires an improved method to quantify this more accurately.

- A controlled growth of Au and Ag nanoclusters in polymers such as Teflon AF 1600 (Teflon), Poly(α-methylstyrene)(PAMS), Polyamid 6 (Nylon), and

Poly(methyl metacrylate)(PMMA) during the co-evaporation was studied in depth. Since the interaction of noble metal atoms with polymer molecules are very weak, the production of controlled metallic nanoclusters in polymers is very challengable. The sticking coefficient of metal atoms on polymer surfaces is a key parameter for a controlled growth and it was studied in relation with the type of metal-polymer combination, the ratio between the deposition rates of metal atoms and the polymer molecules, and the substrate temperature during the co-deposition process.

- The change in the microstructure of metal-polymer nanocomposites upon heat treatment was studied and is presented in this thesis.

- Plasmonic properties of Ag and Au nanoclusters in various polymer matrices (Teflon, PAMS, Nylon, and PMMA) were studied in relation with their microstructure, mainly to the metal volume filling factor, size of the clusters, and interparticle distance.

- Plasmonic properties of polymer composites containing Ag and Au nanoparticles and their changes upon elevated temperature during deposition and post deposition heat treatment are presented in this work.

- Tuning of plasmonic properties in polymer nanocomposites with Ag-Au and Ag-Cu bimetallic nanoclusters was studied.

- Electrical properties of Au and Ag nanoparticles embedded in a polymer matrix was studied with respect to the microstructure of the composites and their change upon annealing.

2 Theoretical Considerations

2.1 Optical Properties of Metal Nanoparticles

2.1.1 The basics of electromagnetic wave interactions

The starting point of the electromagnetic theory of propagation of electromagnetic radiation in material media is the Maxwell's equations. The Maxwell equations (2.1 to 2.6) which describes the propagation of an electromagnetic wave in a metal, link the electric field $\boldsymbol{E}$, the magnetic induction $\boldsymbol{B}$, the electric polarisation $\boldsymbol{P}$, the electric displacement $\boldsymbol{D}$, the magnetisation $\boldsymbol{M}$, the permittivity ϵ_0 and permeability μ_0 of free space. The electric current density $\boldsymbol{j}$ and the electric charge density ρ are usually for that of free electrons.

$$\nabla \cdot \boldsymbol{B} = 0 \tag{2.1}$$

$$\nabla \cdot \boldsymbol{D} = \rho \tag{2.2}$$

$$\nabla \times \boldsymbol{E} = -\frac{\partial \boldsymbol{B}}{\partial t} \tag{2.3}$$

$$\nabla \times \boldsymbol{H} = \boldsymbol{j} + \frac{\partial \boldsymbol{D}}{\partial t} \tag{2.4}$$

The electric displacement $\boldsymbol{D}$, magnetic field $\boldsymbol{H}$, and the current density $\boldsymbol{j}$ are defined by constitutive equations

$$\boldsymbol{D} = \epsilon_0 \boldsymbol{E} + \boldsymbol{P} = \epsilon_0 \epsilon_\infty \boldsymbol{E} \tag{2.5}$$

$$\boldsymbol{B} = \mu_0(\boldsymbol{H} + \boldsymbol{M}) \tag{2.6}$$

$$\boldsymbol{j} = \sigma \boldsymbol{E} \tag{2.7}$$

Here, the conductivity of the medium, σ, and the dielectric constant of the medium ϵ_∞ are phenomenological coefficients which depend on the medium (supposed homogeneous and isotropic) and the frequency.

Assuming the medium as non-magnetic ($\boldsymbol{M} = 0$) and there is no charge accumulation in the metal (ρ=0) for the sake of simplicity. Thus, after substitution of equations 2.5 - 2.7, the electromagnetic wave can be derived

$$\nabla \times \nabla \times \boldsymbol{E} = \nabla\nabla \cdot \boldsymbol{E} - \nabla^2 \boldsymbol{E} = -\mu_0 \sigma \left(\frac{\partial \boldsymbol{E}}{\partial t} \right) - \mu_0 \epsilon_0 \epsilon_\infty \left(\frac{\partial^2 \boldsymbol{E}}{\partial t^2} \right) \tag{2.8}$$

Furthermore, by taking the electric field as periodic, it can be decomposed in time-harmonic functions by the Fourier transform, $\boldsymbol{E}(\omega) = \boldsymbol{E}_0 e^{-i\omega t}$ (complex representation). Thus, equation 2.8 becomes

$$\nabla^2 \boldsymbol{E} = -\mu_0 \epsilon_0 \omega^2 \left[\epsilon_\infty + \frac{i\sigma(\omega)}{\omega \epsilon_0} \right] \boldsymbol{E}. \tag{2.9}$$

For a wave propagating in the free space($\sigma(\omega) = 0$,$\epsilon_\infty = 1$), and equation 2.9 can be reduced to:

$$\nabla^2 \boldsymbol{E} = -\mu_0 \epsilon_0 \omega^2 \boldsymbol{E}. \tag{2.10}$$

If the wave propagates in a non-magnetic medium, the frequency dependent dielectric constant of the medium $\epsilon(\omega)$ in the presence of a wave can be expressed as

$$\epsilon(\omega) = \epsilon_\infty + \frac{i\sigma(\omega)}{\omega \epsilon_0}. \tag{2.11}$$

Although the problem in free space can be solved completely, $\epsilon(\omega)$ and $\sigma(\omega)$ are more complicated to determine in other media. Various experimental investigations and theoretical developments have been carried out in order to determine these values. The Drude theory describes the mechanics of the conduction electrons inside a metal. These are considered as free and independent. The motion of a whole electron cloud is then the sum of the motion of the individual electrons: the coupling between them is thus considered as maximum when the electrons acting all in phase. The motion of one electron is described by equation 2.12 where m_{eff} stands for the effective mass of the electron, ν is the electron

speed and e the charge of the electron:

$$m_{eff}\left(\frac{d\nu}{dt}\right) + m_{eff}\Gamma\nu = e\boldsymbol{E} \tag{2.12}$$

The second term is a viscous friction due to different factors such as free electron inelastic collisions but also electron phonon coupling, defects, impurities, etc. Γ is the corresponding damping constant. Compared to that of the electric field, the force exerted on the electrons by the magnetic field is negligible since electrons are moving very slowly compared to light. Based on $\boldsymbol{E}(\omega) = \boldsymbol{E}_0 e^{-i\omega t}$, ν will also be sinusoidal $\nu = \nu_0 e^{-i\omega t}$ and the substitution of this term in equation 2.12:

$$\left(-i\omega m_{eff} + m_{eff}\Gamma\right)\nu_0 e^{-i\omega t} = e\boldsymbol{E}_0 e^{-i\omega t} \tag{2.13}$$

hence

$$\nu_0 = \frac{e}{m_{eff}\Gamma - i\omega m_{eff}}\boldsymbol{E}_0 \tag{2.14}$$

As a result of the individual motion of electrons with electron density n, $\boldsymbol{j}$ can be expressed as

$$\boldsymbol{j} = en\nu = \frac{ne^2}{m_{eff}\Gamma - i\omega m_{eff}}\boldsymbol{E}_0 = \sigma(\omega)\boldsymbol{E}_0 \tag{2.15}$$

$$\sigma(\omega) = \frac{ne^2}{m_{eff}\Gamma - i\omega m_{eff}} \tag{2.16}$$

Thus, from equations 2.16 and 2.11, one can express the dielectric function $\epsilon(\omega) = \epsilon_1(\omega) + i\epsilon_2(\omega)$ (where ϵ_1 and ϵ_2 are the real and imaginary part of the dielectric function, respectively) as a function of known constants: ϵ_∞, n, e, m_{eff} and ϵ_0, of the frequency ω and of Γ as

$$\epsilon\left(\omega\right) = \epsilon_\infty - \frac{{\omega_p}^2}{\omega^2 + i\omega\Gamma} = \epsilon_\infty - \frac{{\omega_p}^2}{\omega^2 + \Gamma^2} + i\frac{{\omega_p}^2\Gamma}{\omega\left(\omega^2 + \Gamma^2\right)}, \tag{2.17}$$

where ${\omega_p}^2 = \frac{ne^2}{\epsilon_0 m_{eff}}$ is the Drude plasma frequency. The relaxation constant Γ can be related to the electron mean free path ℓ by $\Gamma = \upsilon_F/\ell$, where υ_F is the Fermi velocity. For $\omega \gg \Gamma^{-1}$ the real and imaginary part of $\epsilon(\omega)$ for free-electron

metals can be written as

$$\epsilon_1(\omega) \approx 1 - \frac{{\omega_p}^2}{\omega^2}, \tag{2.18}$$

$$\epsilon_2(\omega) \approx 1 - \frac{{\omega_p}^2}{\omega^3}\Gamma. \tag{2.19}$$

2.1.2 Optical properties of a linear isotropic medium: The dispersion, absorption and reflection of light

Let us denote the electric field of the incident electromagnetic wave by vector $\boldsymbol{E}_0$ with frequency ω in a medium with linear susceptibility χ. It is common to express the dielectric function $\epsilon(\omega)$ in terms of the electric susceptibility χ to give $\epsilon(\omega) = 1 + \chi(\omega)$ where χ is the susceptibility. From the electromagnetic wave equation 2.8, the electromagnetic wave propagating in the medium in one direction x with the electric field strength can be expressed as

$$\boldsymbol{E}(x,t) = \boldsymbol{E}_0 exp(ikx - i\omega t) \tag{2.20}$$

where $\boldsymbol{E}_0$ is an electric field amplitude of oscillating electromagnetic wave. Here the intensity of light is assumed to be low enough to exclude the nonlinear interactions. The wave vector k, which in general case can be given as $k = k' + ik''$, where k' and k'' are real and imaginary part of the wave vector. Thus, using the wave vector equation, we can rewrite equation 2.20 as

$$\boldsymbol{E}(x,t) = \boldsymbol{E}_0 exp(-k''x) exp(ik'x - i\omega t). \tag{2.21}$$

Then, k'' is responsible for the damping of the electromagnetic wave in the medium and defines the amplitude, while the real part k' is combined with the phase of the electromagnetic wave. Moreover, the absorption coefficient can be expressed via imaginary part of the wave vector as

$$\alpha = 2k'' \tag{2.22}$$

Substituting equation 2.20 in equation 2.8 and taking into account $\nabla \cdot \boldsymbol{E} = 0$

in homogeneous medium with no external charges, then

$$k^2 = \omega^2 \mu_0 \epsilon_0 \epsilon(\omega) = \frac{\omega^2}{c^2} \epsilon(\omega) \tag{2.23}$$

where

$$\epsilon(\omega) = \epsilon_1 + i\epsilon_2 = (1 + \chi(\omega)) + i\frac{\sigma(\omega)}{\epsilon_0 \omega} = (1 + \chi'(\omega)) + i\left(\chi''(\omega) + \frac{\sigma(\omega)}{\epsilon_0 \omega}\right) \tag{2.24}$$

is a relative complex dielectric permittivity of the medium and $c = 1/\sqrt{\mu_0 \epsilon_0}$ is the light velocity in the vacuum, $\chi(\omega) = \chi'(\omega) + i\chi''(\omega)$ is the complex linear susceptibility of the medium. The linear susceptibility can be expressed via Lorenz function as

$$\chi(\omega) = \frac{Ne^2}{m\epsilon_0 \left[({\omega_0}^2 - \omega^2) + i\omega\Gamma\right]}, \tag{2.25}$$

where N is the concentration of electrons, e is the charge of the electron, m is the mass of the electron, ω_0 is the frequency of the electron motion and Γ is the damping term.

By analogy with complex wave vector and using equation 2.23, the complex index of refraction of a medium can be defined as

$$n(\omega) = n' + in'' = \sqrt{\epsilon(\omega)}, \tag{2.26}$$

where $k' = \frac{\omega}{c} n'$ and $k'' = \frac{\omega}{c} n''$. Hence, using equations 2.22, 2.23, and 2.26 the absorption coefficient and refractive index of the medium can be determined as

$$\alpha(\omega) = \frac{2\omega}{c} Im\sqrt{\epsilon(\omega)}, \tag{2.27}$$

$$n'(\omega) = Re\sqrt{\epsilon(\omega)}. \tag{2.28}$$

Moreover, from equations 2.23 and 2.24, we can obtain a relation between the wave vector and imaginary part of dielectric permittivity as

$$2k'k'' = (\frac{\omega^2}{c^2})\epsilon_2 \tag{2.29}$$

Thus, by using equation 2.22 and the expression for real part of refractive index,

it is possible to derive the following expression for absorption coefficient:

$$\alpha = (\frac{\omega}{cn'})\epsilon_2. \tag{2.30}$$

Equation 2.30 indicates that the imaginary part of the dielectric permittivity is responsible for the damping of the electromagnetic wave in the medium. Therefore, the absorption coefficient and refractive index are defined by the dielectric properties of the medium. Furthermore, the absorption is responsible for the attenuation of the amplitude of the electromagnetic wave propagating in the medium, and refractive index defines the phase of this electromagnetic wave. Effects observed on the boundary of two media (refraction and reflection) are also caused by the linear optical response of the media.

2.1.3 Optical properties of composite medium containing metal nanoparticles: Surface plasmon resonance

The theoretical discussion and derivations performed above for a linear isotropic medium are valid also for the nanocomposite materials. However, interaction of an electromagnetic wave with nanostructures reveals novel optical phenomena indicating unrivaled optical properties of these materials caused by different intrinsic and extrinsic size effects in the clusters with size less than the wavelength. As a consequence of reducing the size and the dimensionality of a material, its electronic properties change drastically as the density of states and the spatial length scale of the electronic motion are reduced with decreasing size [20, 21].

Propagating electromagnetic wave in the dielectric medium with incorporated spherical metal nanoparticle causes displacement of conduction electrons relative to the positively charged ionic core and the Columb restoring force causes for oscillation of the conducting electrons on the surface. The oscillation modes comprise an electromagnetic field coupled to the oscillations of conduction electrons and are called surface plasmons. In simple terms, the formation of a surface plasmon can be seen when the electric field of the incoming radiation induces the formation of a dipole in the nanoparticle. There is a restoring force which tries to compensate it, so that a unique resonance frequency matches this electron oscillation within the nanoparticle (Figure 2.1). They are characterized by strong field

enhancement at the interface, while the electric field vector decays exponentially away from the surface (in the nm range) [22, 23]. When the dimensions of the conductor are reduced, boundary and surface effects become very dominant, and for this reason, the optical properties of small metal nanoparticles are dominated by such a collective oscillation of conduction electrons in resonance with incident electromagnetic radiation.

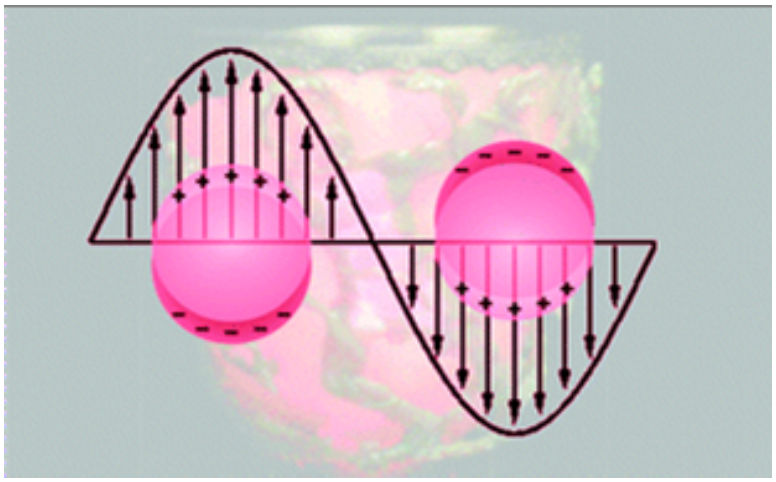

Figure 2.1: *Schematic description of the electronic cloud displacements in nanoparticles under the effects of an electromagnetic wave.*

This dipolar charge repartition imposes a new force on the electron cloud and the electrons undergo a restoring force which interacts with the external electric field. Thus, the position x of an electron placed in the oscillating cloud of a nanoparticle is then governed by equation 2.31 where $\boldsymbol{K}$ is the restoring force.

$$m_{eff}\frac{d^2x}{dt^2} + m_{eff}\Gamma\frac{dx}{dt} + \boldsymbol{K}x = e\boldsymbol{E} \tag{2.31}$$

This approach has never been used for solving the problem, but it is a good model for understanding the surface plasmon band. Nevertheless, the equation describes the movement of a forced, damped harmonic oscillators which is equivalent to classical mechanical oscillator.

In 1908 Mie proposed a solution of Maxwell's equations, which explains the origin of the surface plasmon resonance in extinction spectra and coloration of the metal colloids. Relative simplicity and versatility are the advantage of the

classical Mie theory, which assumes that the particle and the surrounding medium are homogeneous and can be described by bulk optical dielectric functions [6, 8]. Considering the case of spherical nanoparticles much smaller than the wavelength of the electromagnetic wave, the electrostatic approximation is valid and the dipole moment of the embedded in dielectric sphere can be given as:

$$\boldsymbol{P}(\omega) = \alpha\epsilon_0\boldsymbol{E}_0(\omega) = 4\pi\epsilon_0 R^3 \frac{\epsilon_m(\omega) - \epsilon_h}{\epsilon_m(\omega) + 2\epsilon_h}\boldsymbol{E}_0(\omega) \tag{2.32}$$

where α is the polarisability of the sphere, R is the radius of the nanoparticle, $\boldsymbol{E}_0(\omega)$ electric field strength of an incident electromagnetic wave, ϵ_0 electric permittivity of vacuum, $\epsilon_m(\omega)$ and ϵ_h are the relative complex electric permittivity of metal and the dielectric host, respectively.

If the metal inclusion is placed in a transparent dielectric host owing the electric permittivity with predominant real part ($Im[\epsilon_h] \rightarrow 0$), then using the equations 2.30 and 2.32, the absorption cross section of the spherical nanoparticle can be derived as

$$\sigma(\omega) = \frac{\omega}{c\sqrt{\epsilon_h}} Im\left[\alpha(\omega)\right] = 12\pi R^3 \frac{\omega\sqrt[3]{\epsilon_h}}{c} \frac{\epsilon_2(\omega)}{\left[\epsilon_1(\omega) + 2\epsilon_h\right]^2 + \epsilon_2(\omega)^2}. \tag{2.33}$$

The Mie theory which holds for isolated particles whose interaction can be neglected then reduces to the following relationship for the extinction cross-section, σ_{ext} ($\sigma_{ext} = \sigma_{abs} + \sigma_{sca}$) ($\sigma_{abs}$ - absorption cross-section, σ_{sca}- scattering cross-section) for metallic nanoparticle as:

$$\sigma_{ext}(\omega) = 9\left(\frac{\omega}{c}\right) V_0 {\epsilon_h}^{3/2} \frac{\epsilon_2(\omega)}{\left[\epsilon_1(\omega) + 2\epsilon_h\right]^2 + \epsilon_2(\omega)^2} \tag{2.34}$$

where $V_0 = (4\pi/3)R^3$ denotes the particle volume, ω is the angular frequency of the exciting radiation, $c = \frac{\omega}{2\pi}\lambda$ is the speed of light in vacuum. Thus, equation 2.34 can be rewrite as

$$\sigma_{ext}(\omega) = \frac{24\pi^2 R^3 {\epsilon_h}^{3/2}}{\lambda} \frac{\epsilon_2(\omega)}{\left[\epsilon_1(\omega) + 2\epsilon_h\right]^2 + \epsilon_2(\omega)^2} \tag{2.35}$$

From equation 2.34, the well known Mie resonance occurs at the surface

plasmon frequency ω_{sp} under the following condition:

$$[\epsilon_1(\omega) + 2\epsilon_h]^2 + \epsilon_2(\omega)^2 \rightarrow Minimum \tag{2.36}$$

If ϵ_2 is small in comparison with ϵ_1 or weakly dependent on ω, then equation 2.36 can be written as:

$$\epsilon_1(\omega_{sp}) = -2\epsilon_h \tag{2.37}$$

Thus, if the condition in equation 2.37 is complied, the dipole moment and local electric field in vicinity of the nanosphere grow resonantly and can achieve magnitudes in many orders overcoming the filed of the incident wave. This phenomena is responsible for the surface plasmon absorption band.

Nevertheless there are different nomenclatures of plasmon types which can be confusing. There are three classes of plasmons (Volume or bulk, Surface, and Localized) depending on the geometry of the metal under study. The volume or bulk plasmon refers to the collective longitudinal oscillation of electrons that occurs within the bulk of the metal (beyond the penetration depth or skin depth of any optical field, i.e. in the order of $20 - 80\ nm$). Volume plasmons have the highest energy and typically measured by electron energy loss spectroscopy (EELS).

The surface plasmon is a collective longitudinal oscillation of electrons that occurs at a boundary between a metal and a dielectric. A related excitation sometimes confused with the surface plasmon is the surface plasmon-polariton. The difference is that the polariton excitation is coupled with photons, whereas a plasmon can also be exited by electrons or other radiation. The localized plasmon is essentially a special case of the surface plasmon-polariton in which the excitation is localised in three dimensions. This is precisely the case with a metal nanoparticle, and it is the type of plasmon to which we will refer mostly. Many alternate terms are given in the literature for "Localized Surface Plasmon Resonance"(LSPR), such as Particle Plasmon, Mie Resonance (historical choice, but valid only for spheres), Surface Plasmon Resonancs (SPR)(the most common term), Surface Plasmon-Polariton, and Localized Surface Plasmon-Polariton Resonance.

2.1.3.1 Analysis of surface plasmon resonance

The optical properties of nanoparticles differ substantially from the optical properties of bulk materials. Under the influence of an electric field, there is a plasmon excitation of electrons at the particle surface. This causes to an optical absorption at a certain energy of the incident light. Surface plasmons are collective excitations of the electrons at the interface between a conductor and an insulator (see above). They are described by evanescent electromagnatic waves that are not necessarily located at the interface. When a particle is under the action of an electromagnetic field, its electrons start to oscillate, transforming energy from the incident electromagnetic wave into, for example, thermal energy in an absorption process. The electrons can also be accelerated, and then, they can radiate energy in a scattering process. The attenuation by the sum of scattering and absorption of an electromagnetic wave going through a material is called the electromagnetic extinction.

Mie was the first to describe the optical properties of nanoparticles quantitatively by solving the Maxwell equations for the optical response of spherical particles with arbitrary size immersed in a homogeneous medium, and subjected to a plane monochromatic wave as shown in section 2.1.3 equation 2.35. On the other hand, rigorous solutions of the Maxwell equations for nonspherical particles are not straight forward and has provided new challenge for theory. Nevertheless, the Mie's theory has remained important for long time because of its simple and exact solution to the Maxwell's equations that is relevant to non-interacting spherical particles. Note that, most of the standard colloidal preparations yield particles that are approximately spherical, and the concentration is low enough to neglect interaction between the particles.

The dielectric functions $\epsilon(\omega)$ can be written as a combination of an interband and intraband electron transition, which we can assume as additive [24]

$$\epsilon(\omega) = \epsilon_{inter}(\omega) + \epsilon_{intra}(\omega) \tag{2.38}$$

Interband contribution are due to electron transitions from occupied to empty bands separated by an energy gap. The electrons are bound by restoring force given by the energy difference between ground and excited electronic states

in metals, usually at the ultra violet (UV) region. Intraband contributions come from electron transitions at the Fermi level in incompletely filled bands, or when a filled band overlaps in energy with an empty band. These transitions also provide an absorption mechanism but at lower energies. The contribution due to the free conduction electrons can be described by the Drude model

$$\epsilon_{intra}(\omega) = 1 - \frac{{\omega_p}^2}{\omega^2 + i\Gamma\omega} \tag{2.39}$$

where ω_p is the bulk plasma frequency (${\omega_p}^2 = ne^2/\epsilon_0 m_{eff}$) expressed in terms of the free electron density n, the electron charge e, the vacuum permittivity ϵ_0, and the electron effective mass m_{eff}. The damping constant Γ is related with the life time of all electron scattering processes in the bulk material that are mainly due to electron-electron, electron-phonon, electron-defect scattering. For a small particle, the electron-surface scattering also becomes dominant, since the mean free path of the conduction electrons, typically in the range of tens of nanometers in noble metals, is limited by the particle boundaries.

When the particles are not too small one can correct the dielectric function approximately by modifying the value of Γ. For very small particles ($R < 50\ A$) the correction (sometimes referred as quantum size effects) can be complicated and can result in band narrowing, band splitting, and frequency shifts in either direction from that of the SP band center of bulk particles. Particles comprised of only a few atoms are, of course, best treated as large molecules. For particles that are not too small, Γ can be related to the particlet's size by the well-known expression

$$\Gamma(R) = \Gamma_b + \frac{A\upsilon_F}{R} \tag{2.40}$$

where the bulk damping constant $\Gamma_b = \upsilon_F/l_b$ (l_b bulk mean free path of electrons), υ_F is the velocity of the electrons at the Fermi energy, and A is a geometric factor that relates the appropriate electronic mean free path to the particlet's average radius. The expression implies that electrons in a small particle sustain scattering processes with a mean-free path of the order of radius of the particle in addition to the electronic scattering processes occurring in the bulk metal. Thus, it contains information on the scattering processes involved during optical excitation and relates to the width of the surface plasmon resonance.

As a result, well separated metallic nanoparticles and nanostructures, with dimensions significantly smaller than the wavelength of the exciting light, are characterized by a broad, intense absorption band in the visible range of the spectrum. The bandwidth, the peak height, and the position of the absorption maximum depend markedly on the substance, size, size distribution, shape, interparticle separation, the surface state, surface coverage, the surrounding environment of the given nanoparticles and nanostructures.

Substance: By substance we refer to the particular metal constituting the particle, specifying the material dielectric function. For instance, assuming all parameter are equal, the LSPR of silver will occur at the shortest wavelength (highest energy), followed by gold, then copper at the longest wavelength (lowest energy). For the ideal case of spheres in vacuum, silver also has the strongest (brightest) resonance by more than an order of magnitude; gold is slightly stronger than copper. These differences relate directly to the different dielectric functions of each metal. The different LSPR spectral positions and strengths are related to the differing onset of interband transitions in each (Ag at round 4 eV, and Cu at about 2 eV). It should be noted, therefore, that the Mie resonances in noble metals are not truly free-electron-like, but rather "hybrid" resonances with contributions from d-band and conduction-band electrons [8].

Effect of the surrounding dielectric environment: Based on the expression of the Mie extinction cross-section (eqn. 2.35), the dielectric constant of the surounding medium plays a predominant role in determining both the plasmon peak position and intensity. The dielectric environment of the particle helps to determine the strength of the restoring force that the electrons experience. Changing the medium surrounding the nanoparticles for another medium having a markedly different refractive index strongly alters the plasmon behaviour of the the nanoparticles. In general, for non absorbing surrounding, an increase in the index of of refraction of the surroundings red-shifts the LSPR [25, 26]. The spatial distribution of the surroundings matters as well: it makes a difference whether a nanoparticle is embedded in the medium or resting on the surface of the medium [6].

Size and shape effect: As the size effects (R) of the nanoparticles appears in eqn. 2.35, the Mie surface plasmon band theory predicts a size dependence of

the intensity of Surface Plasmon Band. Position and bandwidth are also affected by R, but through intrinsic effects, which means that R modifies the expression of the dielectric constant of the metal and thus alters the resonance condition expressed as $\epsilon_1 = -2\epsilon_m$. However, the size effects are dependence on R, both a blue-shift and a red-shift have been observed with decreasing particle size, but the most typical occurrence is that the SPR will blueshift with decreasing size [27, 28]. The size dependence of the dielectric constant is introduced as the diameter of the particle becomes smaller than the mean free path of the conduction electrons (typically of 50 nm). Both theoretical and experimental results also indicted a $1/R$ dependence of the bandwidth due to surface scattering [29].

Due to the intrinsic complexity of the problem and synthesis limitation, the shape effects has been far less studied. However, recently a strong shape dependent of the LSPR of nanoparticles is reported [24]. Nanoparticles featuring original shapes such as rods, disk, squares, triangles, stars and others were exhibited from double to multiple resonance bands. If the orientation of the observed nanorods is arbitrary, the optical signature is the existence of two bands, one corresponding to the longitudinal mode and the other to the transverse one [30, 31].

Influence of the interparticle distance: As a result of the dipole-dipole interaction between the nanoparticles, the distance between the neighboring nanoparticles have a significant role on the surface plasmon band. The surface plasmon band broadens and shifts to higher wavelength when the interparticle spacing becomes smaller [25, 32].

2.2 Various Models and Percolation Theory

2.2.1 The effective medium models

Beside the synthesis of composite materials consisting of metal nanoparticles in a dielectric matrix, a number of theoretical models and theories have been developed in order to describe their optical response. As mentioned before, Mie first provided the complete solution concerning the absorption and scattering of light by a spherical single metallic particle. Later models accounting for the col-

lective properties of metal particles in composites were developed, such as the Maxwell-Garnett(MG) theory and the Bruggeman effective medium approximation(EMA).

Figure 2.2 shows the most commonly encountered structures of composite materials, the Maxwell Garnett geometry consists of small inclusion particles embedded in a host material(a) and the Bruggeman geometry consists of two intermixed components(b). These two model geometries are the structures most often encountered in theoretical discussions of composite materials [33–35].

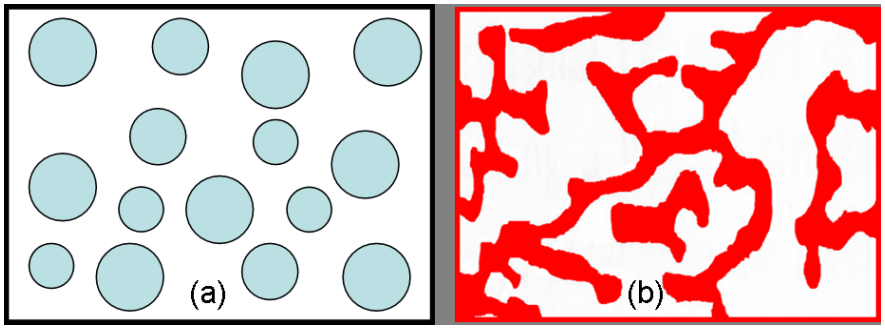

Figure 2.2: *Some examples of composite material structures (a) Maxwell Garnett and (b) Bruggeman geometry.*

The effective medium approach is characterized by a priori statistical cluster distributions which are included in the calculation of a proper effective dielectric function of the whole sample by assuming mean electric fields [36–38]. The effective medium approach is principally based on two assumptions: i) the inhomogeneities are so large that each point in the material can be associated with the macroscopic dielectric function; ii) the system can be described as an effective medium if the random unit region, embedded in the effective medium, is not detectable in an experiment using electromagnetic radiation confined to a specified wavelength range [39].

With these theories, an effective dielectric function is calculated from the dielectric functions of both basic materials by using the volume filling factor. The Maxwell-Garnett (MG) theory has been derived for topologically asymmetric composites, where one constituent predominates and forms a host medium (dielectric) for small grains of the other constituent (metal) embedded in it. In

this case, the size of the embedded spherical particle R and the interparticle separation d are reasonably well-defined and all much less than the wavelength of light λ. This condition guarantees that the scattering due to the inhomogeneities resulting from the composite nature of the material will be negligible, and leads to an effective medium with a dielectric constant ϵ_{eff}.

The MG theory relates ϵ_{eff} to the dielectric constant of embedded metal nanoparticles ϵ_m and the dielectric constant of the host material ϵ_h [35, 40–42]. The derivation of the MG result deduces from the familiar Clausius-Mosotti equation (eqn. 2.41) and the polarizability $\alpha(\omega)$ (eqn. 2.42), itself derived from eqn. 2.32.

$$\frac{\epsilon(\omega)-1}{\epsilon(\omega)+2} = \frac{4\pi}{3}\frac{N}{V}\alpha(\omega) \tag{2.41}$$

$$\alpha(\omega) = R^3\frac{\epsilon_m-\epsilon_h}{\epsilon_m+2\epsilon_h} \tag{2.42}$$

To determine ϵ_{eff} in the MG geometry, one would naturally use this expression for the polarizability and take into account the fact that the inclusion spheres are not in vacuum but in a host material with dielectric constant ϵ_h, and given as

$$\frac{\epsilon_{eff}-\epsilon_h}{\epsilon_{eff}+2\epsilon_h} = f\frac{\epsilon_m-\epsilon_h}{\epsilon_m+2\epsilon_h}, \tag{2.43}$$

where $f = 4\pi NR^3/V$ is the fill fraction of the inclusion.

One can apply these same arguments to consider two (or more) inclusions with fill fractions f_1 and f_2 and the dielectric constants ϵ_1 and ϵ_2, respectively, in a host medium. Thus, the result is given as:

$$\frac{\epsilon_{eff}-\epsilon_h}{\epsilon_{eff}+2\epsilon_h} = f_1\frac{\epsilon_1-\epsilon_h}{\epsilon_1+2\epsilon_h} + f_2\frac{\epsilon_2-\epsilon_h}{\epsilon_2+2\epsilon_h}. \tag{2.44}$$

The Bruggeman geometry adopts an assumption that both materials are interdispersed in a topologically equivalent manner. The theory is thus symmetrical. Therefore, the host medium should here be thought of as the effective medium itself, for it is only within this effective medium that each constituent can be properly thought of as embedded. Thus eqn. 2.44 becomes eqn. 2.45,

with $\epsilon_h = \epsilon_{eff}$

$$0 = f_1 \frac{\epsilon_1 - \epsilon_h}{\epsilon_1 + 2\epsilon_h} + f_2 \frac{\epsilon_2 - \epsilon_h}{\epsilon_2 + 2\epsilon_h}. \tag{2.45}$$

Moreover, for the case where the particles do not have a spherical shape, various extensions of the MG theory for nonspherical particles were introduced as shown in eqn. 2.46

$$\frac{\epsilon_{eff} - \epsilon_h}{\epsilon_h + L\left[\epsilon_{eff} - \epsilon_h\right]} = f \frac{\epsilon_m - \epsilon_h}{\epsilon_h + L\left[\epsilon_m - \epsilon_h\right]}. \tag{2.46}$$

where L is the depolarization factor describes the ratio between the axes of the ellipsoids ($0 \leq L \leq 1$).

In general both the MG and EMA models are limited to systems with low metal or nanoparticle concentration up to 5 % and fall short of a correct prediction of the far infrared absorption even in these low metal concentration region. With an increase in the filling factor of metal inclusions in the dielectric matrix the interparticle distance becomes smaller and leads to an interaction between the nanoparticles. As a result, the EMA theory will be terminated to well describe the experimental results obtained for higher filling factors due to the multi-polar polarizability contributions.

Recently a modified EMA theory which fits well for up to 20 % is reported [43, 44] and the experimental results presented in this work were used to check the accuarcy of the improved theory (see section 6.1.1.1). This modified theory helps to expand the applicability limits of the EMA to higher metal concentrations.

2.2.2 Percolation

In abstract terms percolation is the passage of an influence through a medium which is irregular structured in the sense that through some regions the influence can pass more easily than in others and in some places not at all [45]. The fundamental question is that whether this disorder of the medium has some probability distribution so that the influence move infinite distance through the medium at a certain values.

For simplicity of the problems one can consider two dimensional case of

clusters distributed in an empty sites with a probability p that a site is occupied. The section of the lattice is finite with L^2 sites and to obtain properties independent of the existence of the boundaries, $L^2 \to \infty$ at suitable points in the theory.

A cluster is a group of sites such that each member is nearest neighbor to at least one other member of the group. If an influence could travel only between nearest neighbors, infinite cluster would enable the influence to percolate across the system and is therefore called a percolating cluster. Finite clusters will not contribute to percolation. The percolation probability $P(p)$, is the probability that an occupied site is in the percolating cluster. This probability will be zero if p is too small. In an infinite lattice, $P(p)$ rises from zero as p increases above a critical value p_c. One is interested in how many objects can form a cluster of communication and, especially, when and how the cluster become infinite. The control parameter is evidently the density n of the objects (their average number per unit volume), or the dimensionless filling factor. The percolation threshold corresponds to the minimum concentration at which an infinite cluster spans the space [46].

An important problem in describing the transport properties of random multiphase materials is the prediction of the percolation thresholds as a function of volume fraction, interparticle interaction, shape, and orientation of the component phases or particle of the random material. An idealized model of percolation is that of completely permeable objects, whose free overlap as more and more objects are randomly added to a matrix eventually results in a geometrical connected phase as shown in figure 2.3.

Moreover, the shape of the clusters affect the percolation [47]. Figure 2.4 shows the inverse of P_c plotted against the aspect ratio a/b of ellipsoids. In the extreme oblate and prolate limit, it is clear that $1/P_c$ scales linearly in the inverse of the aspect ratio. The ratio of the ellipsoidal radii a/b varies from 1/2000 to 500. For spherical clusters with $a/b = 1$, the value of p_c becomes 0.29.

In addition, the size distribution of clusters determine the percolation point. A broad distribution of nanoparticles lead to a shift of the percolation point to higher metal filling factor.

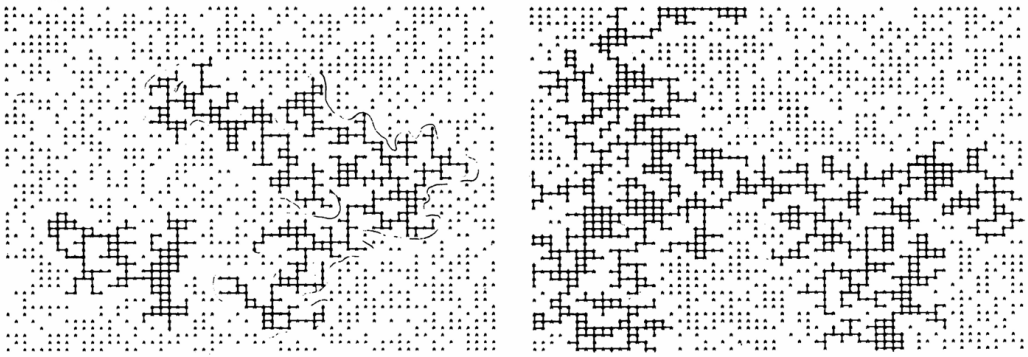

Figure 2.3: *An illustration of bond percolation for a two-dimensional lattice under (left) and over (right) the critical percolation.*

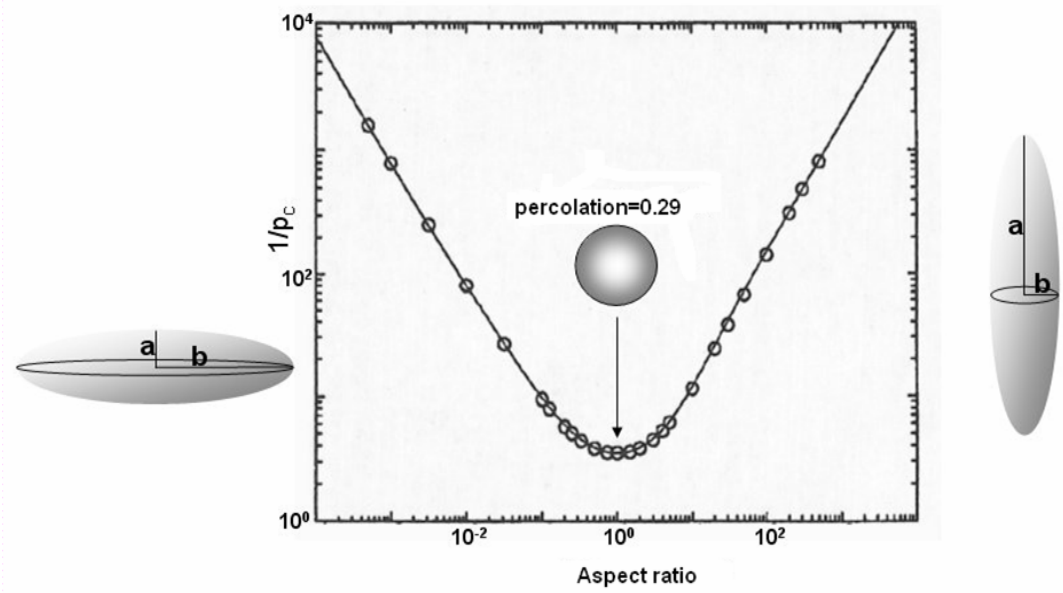

Figure 2.4: *Inverse of the critical volume fraction for percolation ($1/p_c$) plotted vs aspect ratio of ellipsoids of revolution.*

3 Experimental

3.1 Introduction

The synthesis of metallic nanoclusters has been the focus of the research work in the field of nanotechnology in the last three decades. At present, among the various techniques developed for the synthesis of nanoclusters, chemical preparation, electrochemical deposition, laser ablation, vacuum deposition (evaporation or sputtering), and electron-beam lithography are the most recent advances of this time. In this work, vacuum deposition (evaporation), which involves the condensation of a metal shot placed on a heating element [48, 49], was implemented to prepare nanoclusters. Here, vapor-phase co-deposition of metal atoms and polymer molecules was used to synthesize polymer composites containing nano-sized metallic particles. The mechanism of metal and polymer evaporation, and as well as the experimental procedures and parameters to produce polymer-metal nanocomposites will be described in this section.

3.2 Evaporation Chamber

All the experiments in this work were carried out by using a home made evaporation chamber facility at the Chair for Multicomponent Materials, Kiel University. The chamber is originally constructed to evaporate metals and polymers from distinct heatable sources and it has a potential to evaporate five different materials simultaneously. The cross-sectional view and image of the interior part of the chamber are shown in figure 3.1, and 3.2, respectively.

The chamber consists of the evaporators, the sample holder, and the quartz crystal microbalance for an in-situ monitoring of the film thickness. Moreover, it

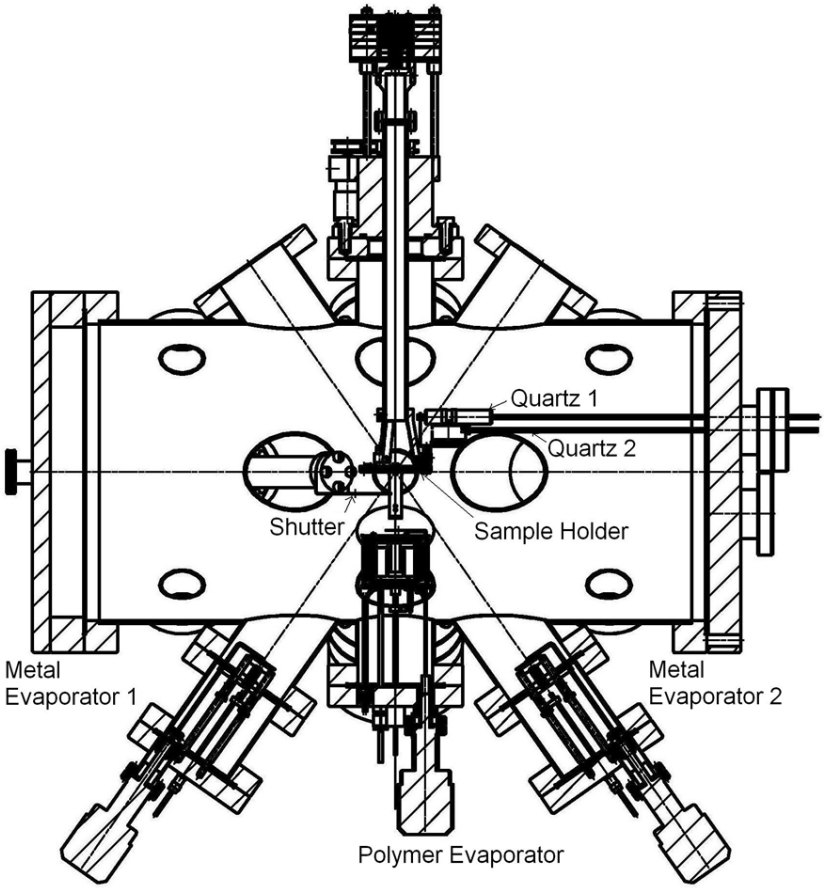

Figure 3.1: *Cross-sectional view of the chamber which includes two metal evaporators and one central polymer evaporator.*

contains an electrical power feed through in order to bring power to the vacuum vessel to heat the evaporator and/or to heat the substrate holder. The physical vapor deposition process employed in this work always takes place in a high vacuum environment. A rotation pump (Pfeiffer DUO 005 M), to generate the pre-vacuum (10^{-1} *torr*) together with a turbomolecular pump (Pfeiffer TMU 260) were used for creating the end-vacuum in the range of $10^{-7} - 10^{-8}$ *torr*. A relatively good vacuum condition is required to reduce collision of the transported material with the residual gas. Thus, the reduction in the rate of deposition and oxidation of the materials were prevented.

The heatable substrate holder was positioned to achieve an optimal uniform film thickness received from both metal and polymer vapor. In this case, a

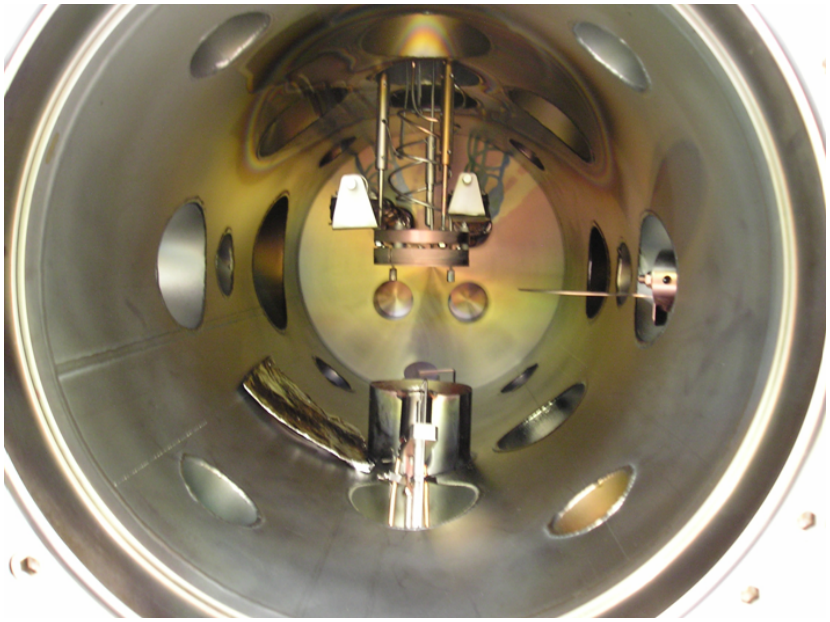

Figure 3.2: *Photo of the internal part of the deposition chamber.*

flat plate substrate holder (with a diameter of 6 *cm* and thickness 2 *cm*) made of copper was used to host the substrates to achieve a relatively uniform film thickness and heat transfer. Though, maintaining the film uniformity is always desirable, but not necessarily required for this research.

In this method, the thickness and metal volume fraction in the polymer composite film are strongly related with the geometrical effect of the chamber such as the angle of deposition and the distance between the source and substrate. Assuming, a point source which is perpendicular to the sample holder $\phi = 0$ and $cos\theta = h/l$, and the surface source where $cos\theta = cos\phi = h/l$, the thickness of the film is given by 3.1 ans 3.2, respectively.

$$\frac{d}{d_0} = \frac{1}{\{1 + (\frac{l}{h})^2\}^{\frac{3}{2}}} \tag{3.1}$$

$$\frac{d}{d_0} = \frac{1}{\{1 + (\frac{l}{h})^2\}^{2}} \tag{3.2}$$

where h and l are the perpendicular distance from point source to the center of

the substrate holder and the distance from source to a point on the substrate, respectively. Noting that $r = \{h^2 + l^2\}^{\frac{1}{2}}$, and the thickest deposit d_0 occurs at $l = 0$. A comparison of equations 3.1 and 3.2 are shown in Figure 3.3, where it is apparent that less thickness uniformity can be expected with the surface source.

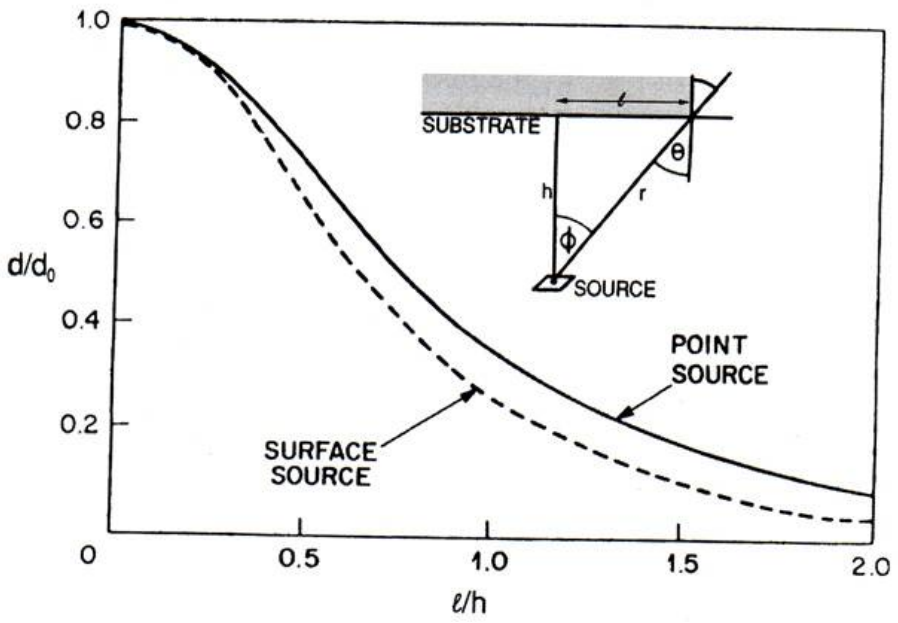

Figure 3.3: *Film thickness uniformity for point and surface sources [50].*

The preparation of metal-polymer nanocomposites requires evaporation of metals and polymers from two or more different sources simultaneously. In this case, the distance between the sources is also considered in addition to the source-substrate distance. A superposition of the solutions from two individual sources give the thickness variation in the composite films as shown in figure 3.4. In the home made experimental chamber shown in figure 3.1 a relatively more uniform film thickness of the composites is obtained by using a symmetrically opposite sources for the metal and polymer. Moreover, a rotatable sample holder can be used if the film thickness uniformity is more important than the gradient in concentration.

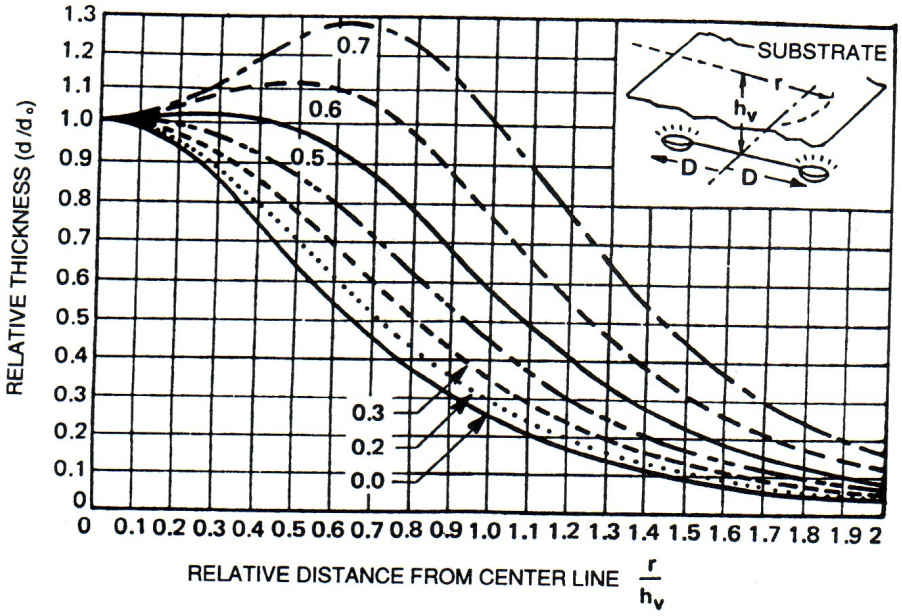

Figure 3.4: *Film thickness uniformity across a trip employing two evaporation sources for various values of D/h_v [50].*

3.3 Evaporation of Metals

3.3.1 Metals

Metals are characterized by the so-called metallic bond. In metals the outer valance electrons of each atom form part of a collective free electron cloud or gas that permeates the entire lattice. This free-electron gas has a strong electrostatic attraction with the positive ion cores. Nevertheless, there are also an electron-electron repulsive interactions.

Electrons of the metal indifferent from other solids have the ability to exhibit a property in response to the external applied electric fields, thermal gradients, and incident light. Here noble metals (Copper, Silver and Gold) in which the d-bands of the electronic structure are filled and do not cross the Fermi level are deposited, since they are chemically inert and show strong collective exitation in the visible region.

3.3.2 Evaporator cell and evaporation of metals

Metals, typically gold, silver and copper with 99.99% purity from Goodfellow industry are evaporated in a high vacuum chamber from an integral crucible-heater assembly. The external and internal schematic design of the metal evaporator are shown in figure 3.5 and 3.6, respectively.

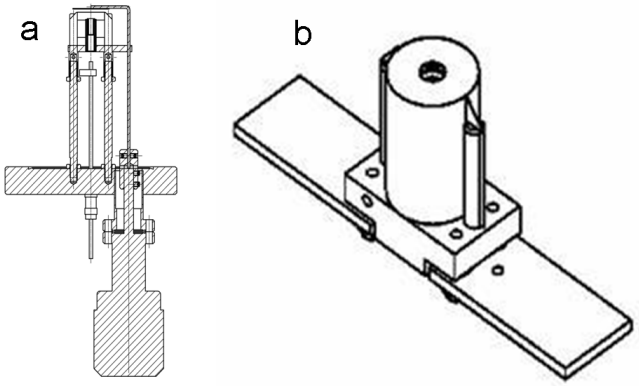

Figure 3.5: *External part of metal evaporator. (a) the whole body of the metal evaporator with a power feed through, (b) the shield that covers the crucible.*

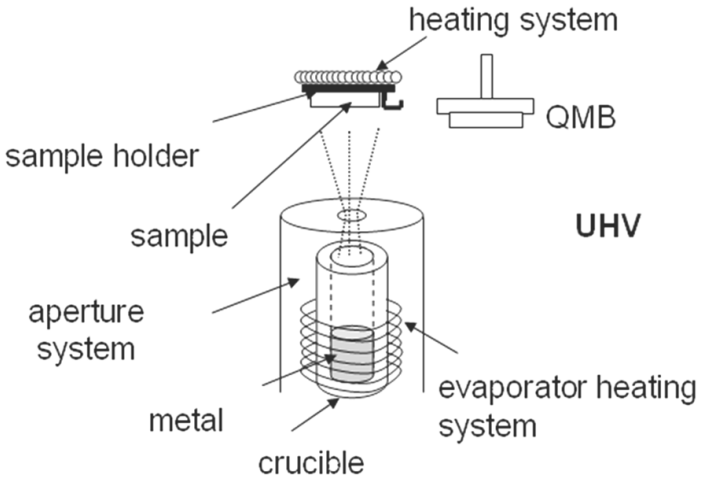

Figure 3.6: *Internal part of the metal evaporator cell*

The home made metal evaporator as shown in figure 3.6 is carefully designed

to reduce any possible thermal coupling problem. The Tantalum (Ta) heater coil filament was selected to carry the high current and generate the heat required to evaporate the charge. Ta is known for its high melting point, thermal shock resistance, and ductility among the refractory metals. In this design, the Ta heater coil is minimally supported within notched ceramic support rods to reduce heat sinking. The coil extends well below the bottom of the crucible so that the thermocouple touching the crucible bottom is immersed within the same heating environment as the crucible and thus stabilizes at the same temperature. Moreover, the coil is extended towards the crucible mouth, above the level of the charge, which leads the mouth of the crucible to be at higher temperature than the temperature of the charge. This prevents condensation of evaporant droplets at the mouth and also prevents evaporants which wet the crucible from migrating out of it. In addition, the radiation heat shielding consists of several wraps of corrugated Ta foil is used to reflects radiation from the coil and crucible, thereby improving source temperature and reducing out gassing of nearby hardware.

A cup shaped crucible sources (length=17mm, and inner diameter=3mm) made of aluminum oxide, molybdenum, and boron nitride were used as a source of the evaporant. The boron nitride crucible was found to be the best type for the evaporation of Au, Ag and Cu as compared to others. In some cases, diffusion of evaporant materials into the crucible material and crack formation in the crucible was observed in case of Au evaporant and molybdenum crucible. Crucible materials should be chosen whose residual contaminants are the least harmful to the film being deposited. However, much of the volatile contaminant were removed from the crucibles and associated components by firing it at a higher temperature than the desired evaporation temperature prior to the filling with new evaporant.

The crucible sources has converted to a Knudsen cell by adding a closely fitting cover with a small orifice to the crucible (Figure 3.7). In this case, the flux through the orifice in each direction (in and out) is equal to the impingement flux at the plane of the orifice. In the molecular flow region, the two fluxes are independent of each other since the molecules cross paths without colliding. In addition, an orifice at the top is small enough so that the resulting effusion ($Q_e << Q_v$) does not significantly reduce the pressure in the vapor phase ($P \approx P_v$). As is generally known, the equilibrium vapor pressure would be obtained in a

thermodynamically closed system, but it is not possible in practical evaporation. In evaporation, the environment of the vapor source acts as a vapor sink and the evaporant atoms condense on all parts that are at lower temperature than the vapor source.

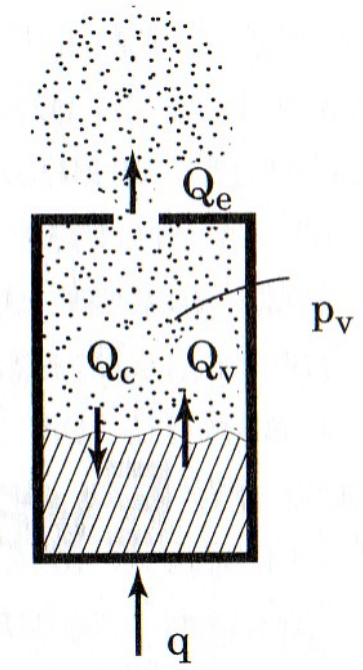

Figure 3.7: *Knudsencell*

Systematic investigations of evaporation rates in vacuum has been performed carefully mainly by Hertz, Knudsen and Langmuir. In these experiments, the evaporation rate is proportional to the difference between the equilibrium pressure, P_e, and the hydrostatic pressure, P_h, acting on the evaporant. These ideas led to the basic equation for the rate of evaporation,

$$\Phi_e = \frac{\alpha_e N_A (P_e - P_h)}{(2\pi MRT)^{\frac{1}{2}}} \tag{3.3}$$

where Φ_e is the evaporation flux in number of atoms (or molecules) per unit area, per unit time, and α_e is the coefficient of evaporation, which has a value between 0 and 1.

Practically, the rate of deposition of metal atoms in a resistively heated

evaporators is depend on the temperature of the crucible which itself controlled by the electrical power and exhibited an exponential relationship. For instance, the rate of deposition of Au atoms versus the electrical power applied to the evaporator is shown in figure 3.8.

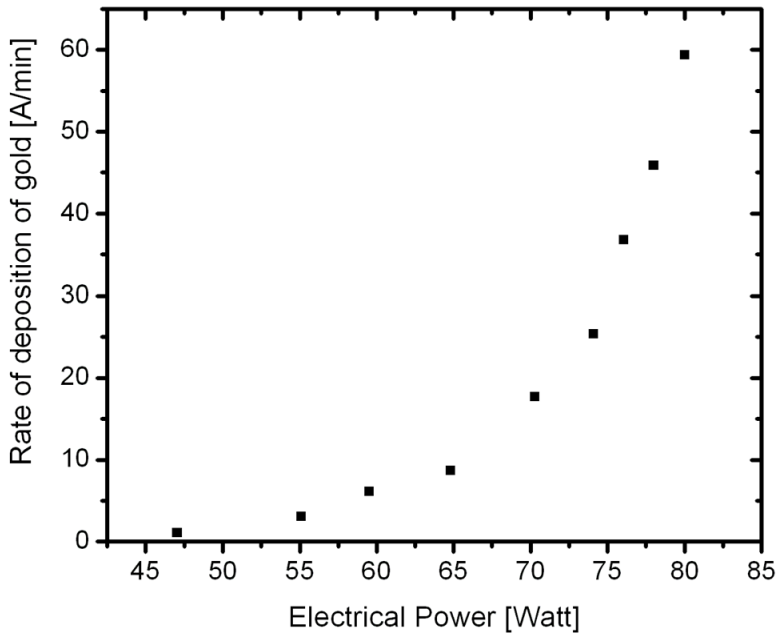

Figure 3.8: *Rate of deposition of gold versus the electrical power supplied to the metal evaporator.*

On the other hand, the rate of deposition of the metal atoms on the substrate exhibit a decrease with the deposition time as shown in figure 3.9. This is related with the amount of material in the crucible and it is an indication for the real evaporator used for the deposition of metal atoms not be considered as a point source rather as an open-tube type of effusion cell. In this case, the beam intensity varies with the level of the material inside the crucible [49]. Figure 3.10 shows some calculated beam intensity curves for L/a values varying from 0 to 10, where L is the distance from the melt to the top of the tube and a is the inner radius of the cell body. L will vary during evaporation.

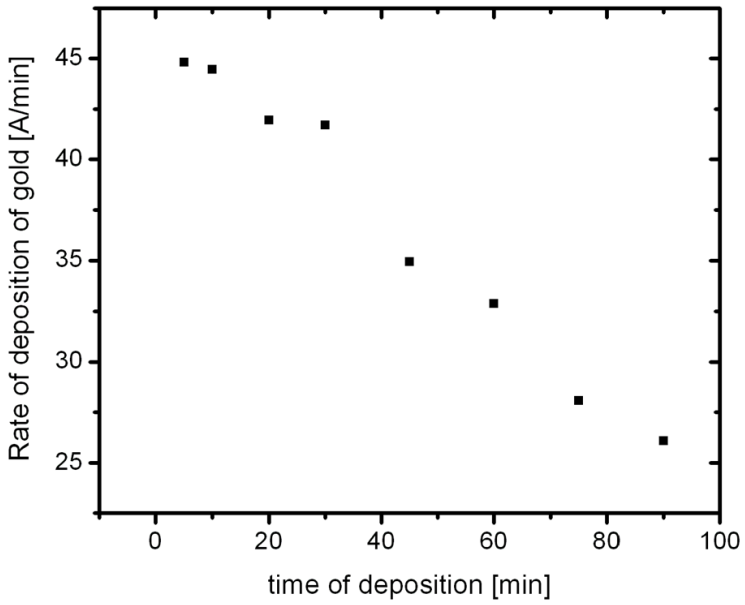

Figure 3.9: *Rate of deposition of gold versus time of deposition*

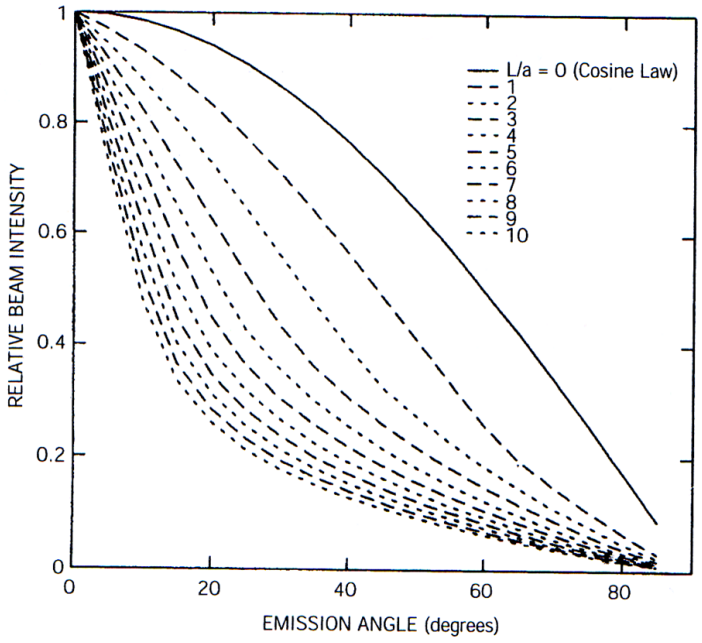

Figure 3.10: *The relative beam intensity of the open-tube effusion cell calculated for various tube length-to-tube radius ratios (L/a).*

3.4 Evaporation of Polymers

3.4.1 Polymers

A polymer is a substance composed of molecules which consist out of a long sequence of one or more species of atoms or group of atoms linked to each other by primary, usually covalent, bonds. In certain cases it is more accurate to call the structural unit a monomer residue because atoms are eliminated from the simple monomeric unit during the polymerization process. The essential requirement for a small molecule to qualify as a monomer or building block is the possession of two or more bonding sites, through which each can be linked to the other monomers to form the polymer chain.

Based on the underlying molecular structure, polymers are classified into three groups: thermoplastics, elastomers and thermosets. Thermoplastics are linear or weakly branched polymers with negligible entanglement. They can be crystalline or amorphous. Those which do crystallize invariably do not form perfectly crystalline materials but instead are semi-crystalline with both crystalline and amorphous regions. The crystalline phases of such polymers are characterized by their melting temperature (T_m). Many thermoplastics are completely amorphous polymers which exist as glassy solids. These polymers are characterized by their glass transition temperature (T_g), the temperature at which they transform from glassy state (hard) to the rubbery state (soft). Both T_m and T_g increase with increasing chain stiffness and increasing forces of intermolecular attraction. Elastomers are cross-linked rubbery polymers that can be stretched easily to high extensions and which rapidely recover their original dimensions when the applied stress is released. This property is a reflection of their molecular structure in which the network is of low crosslink density. Thermosets are rigid network polymers in which chain motion is greatly restricted by a high degree of cross-linking.

The transition from the glass to rubber-like state is an important feature of polymer behavior, marking as it does a region where dramatic changes in the physical properties, such as the specific volume, the modulus, the heat capacity, the refractive index, and thermal expansion coefficient, are observed. This transformation resembles phenomenologically as a second order transition due to

a more pronounced change of the heat capacity and volume thermal expansion coefficient at the vicinity of T_g.

One of the most frequently used methods of demonstrating and determining the T_g is to follow the change in the volume of the polymer as a function of temperature (Figure 3.11). In the regiments above and below the T_g there is a linear variation in specific volume with temperature, but in the vicinity of the T_g there is a change in the slope of the curve which occurs over several degree. Another characteristic of the T_g is that the exact temperature depends upon the rate at which the temperature is changed. It is found that the lower the cooling rate the lower the value of T_g.

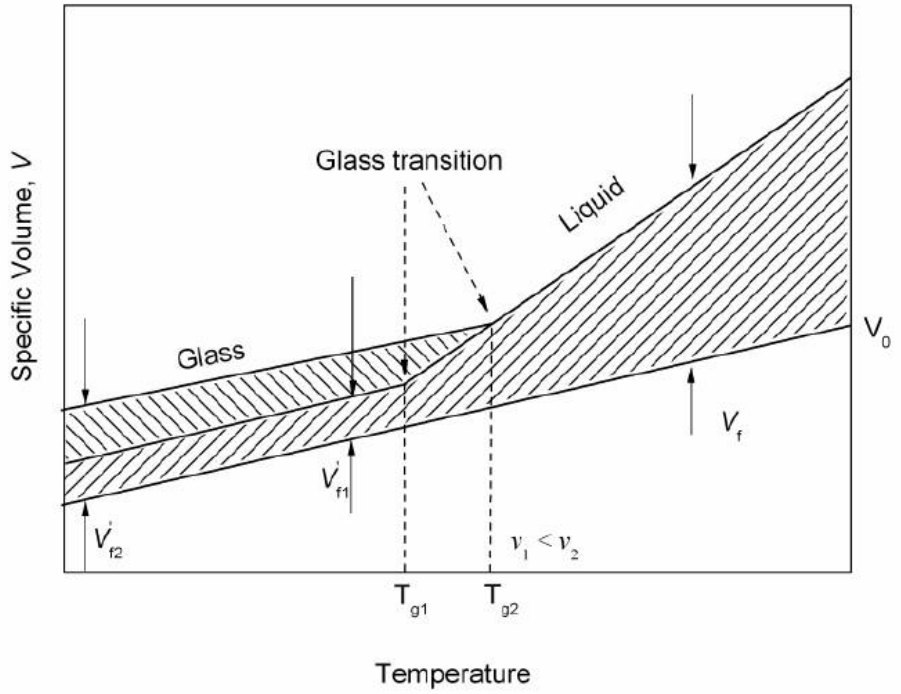

Figure 3.11: *Schematic illustration of the specific volume* **V** *and temperature of a polymer. The value of the glass transition temperature T_g depends on the cooling rate v(K/h).*

In order to analyze the glass transition temperature the concept of free volume is used. The free volume is the space in the solid or the liquid not occupied by polymer molecules, arising from the inefficient packing of disordered chains in the amorphous regions of a polymer sample. The specific volume of a sample

refers to the sum of the volume actually occupied by the polymer molecules and the free volume in the system, which are temperature dependent. The free volume is the measure of the space available for the polymer chain segments to undergo rotation and translation. In the liquid state or rubber-like states the amount of free volume will increase with temperature as the molecular motion increases. If the temperature is decreased, the free volume will contract and eventually reach a critical value when there is insufficient free space to allow large scale segmental motion to take place. The temperature at which this critical value is reached is the glass transition temperature. Below , T_g the free volume will remain essentially constant as the temperature decreases further since the chains have now been immobilized and frozen in position. The glass transition can then be visualized as the onset of co-ordinated segmental motion made possible by an increase of the holes in the polymer matrix to a size sufficient to allow this type of motion to occur.

As the glass transition temperature depends largely on the amount of thermal energy required to keep the polymer chains moving, it also depends upon the physical and chemical nature of the polymer molecules. The most important factors are chain flexibility, molecular structure, molar mass, branching and crosslinking. The flexibility of the chain is the most important factor influencing T_g. It is a measure of the ability of a chain to rotate about the constituent chain bonds, hence a flexible chain has a low T_g whereas a rigid chain has a high T_g. The value of T_g increases as the molar mass of the polymer is increased. A small number of branches tend to reduce the value of T_g, while a high density of branches has the same effect as side groups in restricting chain mobility and hence raising temperature. The presence of chemical cross-links in a polymer sample leads to an increase in the value of T_g, because of the reduced specific volume of the polymer leading to a restriction of molecular motion. If the density of cross-links is very high the temperature range of the transition is broadened and the glass transition may not occur at all.

Over the last decades, polymers have been used successfully in many industrial applications such as packaging, thin films, biomaterials, and coatings. Polymers have excellent bulk physical and chemical properties, are inexpensive and easy to process.

3.4.2 Evaporator cell and evaporation of polymers

A home made boat design evaporator (Figure 3.12 was used to evaporate polymers throughout this work. This evaporator cell contains labyrinth channels made of copper and only used for evaporating polymer. Copper has a high melting point as compared to the vaporization temperature of the polymer ($150 - 540\ ^{\circ}C$). Moreover, it has good thermal conductivity which enables to keep every part of the cell at uniform temperature. The cell is surrounded by the filament and the power supply controls the current passing the filament. A controller connects the nickel - chromium thermocouple attached to the wall of the cell and the power supply. Then the temperature can be adjusted by changing the current.

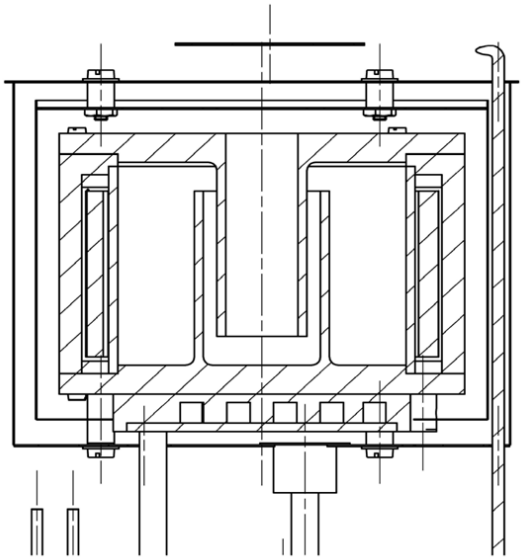

Figure 3.12: *A boat shaped polymer evaporator.*

The rate of deposition of polymers is controlled by the temperature of the cell and it is found that the relationship between the rate and temperature of the cell is not linear. For instance, the rate of deposition of Teflon atoms versus the temperature of the cell is demonstrated as shown in figure 3.13. Nevertheless, in contrast with the deposition rate of metal, the rate of deposition of polymers are more or less stable with the deposition time at a saturated temperature of the evaporator cell.

In this work, simple hydrocarbon polymers, or polymers consists of oxygen,

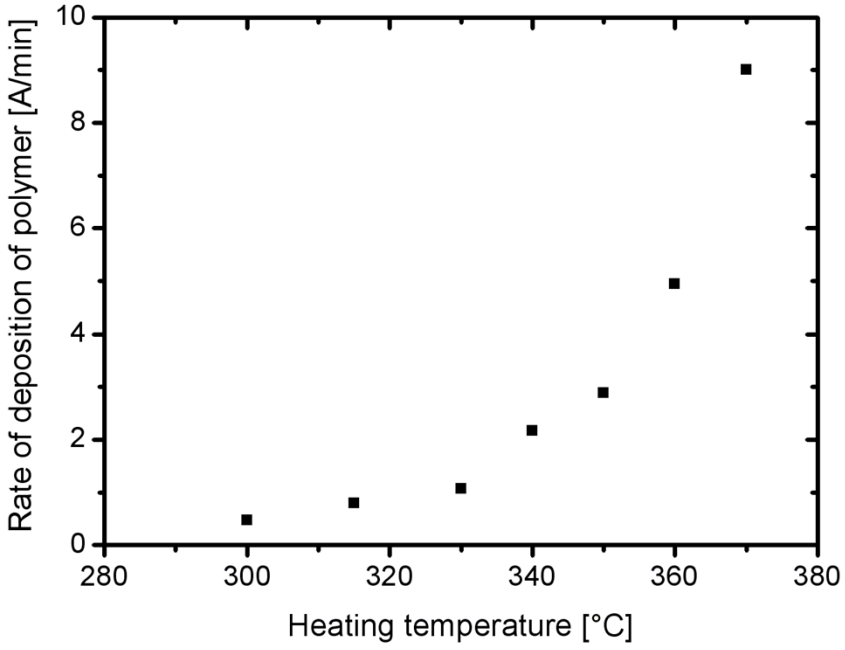

Figure 3.13: *Rate of deposition of Teflon AF versus heating temperature of the polymer evaporator cell.*

nitrogen, flouro groups or aromatic rings were evaporated. The candidate polymers used for this research are: Teflon AF 1600 (Teflon), Poly(α-methylstyrene) (PAMS), Polyamid 6 (Nylon), and Poly(methyl metacrylate) (PMMA). Their chemical structure are shown in figure 3.14. These materials are known in their physical properties such as outstanding optical clarity and transmission in the UV-Visible region, low refractive index, relatively high glass transition temperature, and high chemical resistance.

The cell must be filled with polymer powder or granulate. After applying a high current, the cell is heated up, the polymer melts and the vapor molecules follow the path to the desired exit. Compared with the metal evaporator this will give a high deposition rate and one must avoided the possible explosion. At sufficient rate of evaporation, molecules reach to the substrate and repolymerization occurs. Because of their complicated structures and physical properties of the polymer materials, the polymer thin films are always prepared by the solution method. However, this is not compatible with the vacuum process for the production of electronic devices.

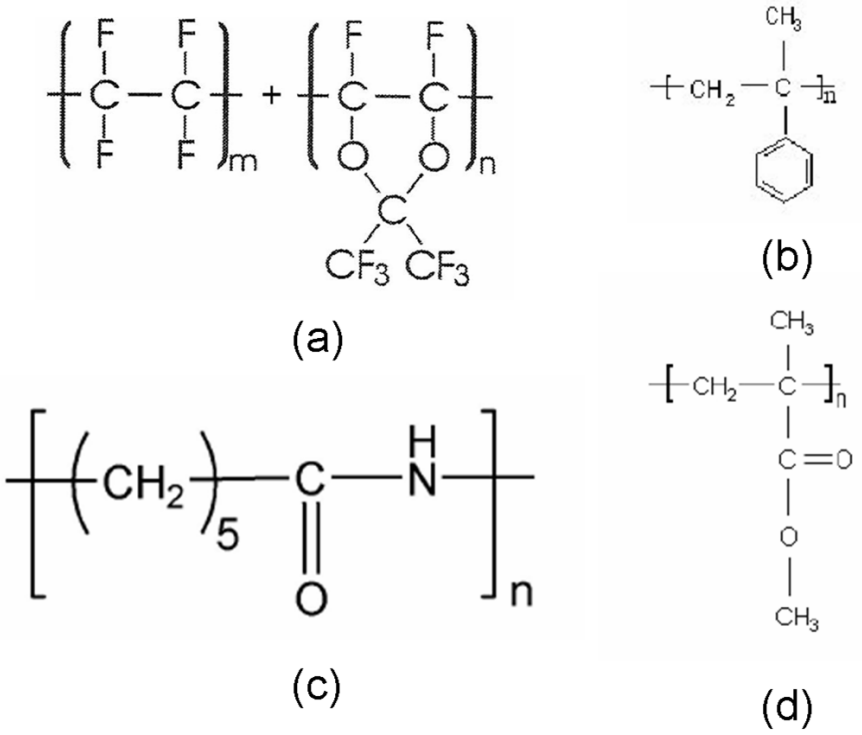

Figure 3.14: *Chemical structure of Teflon(a), PAMS(b), Nylon(c), and PMMA(d).*

During the decomposition, polymeric material itself is essentially unvolatile, and the quite large molecules must be broken down into smaller molecules that can vaporize. In most cases, a solid polymer breaks down into a variety of smaller molecular fragments. Each of the fragments has a different equilibrium vapor pressure. The lighter the molecular fragments vaporize immediately upon their creation while other heavier molecules remain in the condensed phase (solid or liquid) for some time. While remaining in the condensed phase, these heavier molecules may undergo further decomposition to lighter fragments which are then easily vaporized. Some polymers break down completely so that virtually no solid residue remains.

There are two strategies to produce a polymer thin films using the vapor phase deposition method. The first is based on the polycondensation and polyaddition systems. In polycondensation system, two kinds of bifunctional monomers

at their chain ends are coevaporated and polymerized on the substrate. Each monomers can be easily vaporized at relatively low temperatures in an evacuated chamber without any changes in the chemical structure. Up on the arrival on the substrate, the two monomers react easily at their chain ends to form oligomers, which will stay on the substrate for a long time because their vapor pressure decreases. In this case, the resultant polymer thin films include residual monomers and show poor molecular orientation. Moreover, the molecular weight of the deposited film is expected to be lower than the bulk due to unbalance stoichiometry.The second strategy is the thermal degradation of polymers, transport of the decomposition products from the source to the substrate, and repolymerization processes. However, evaporation only works for a few selected polymers with lower molecular weight.

3.5 Co-evaporation of Metals and Polymers

Co-deposition is a simultaneous deposition of two or more materials at the same time. Co-deposition allows the preparation of a single layer of films consist of two or more different materials together. This technique allows to produce metallic nanoclusters distributed in a polymer matrix by co-evaporation of one or more metal atoms along with a polymer from distinct sources.

3.5.1 Preparation of monometallic-polymer nanocomposites

Monometallic-polymer nanocomposites are composite materials which consists a single type of metal nanoclusters three dimensionally distributed in a polymer matrix. In this case, a single metal is evaporated simultaneously with a polymer in a controlled rate of deposition from two different sources. Mainly, Au or Ag (99.99% pure, Good Fellow Industries) was simultaniously evaporated with Teflon (granulates, Dupont), PAMS (granulates, ALDRICH), PMMA (powder, Scientific Polymer Products), or Nylon (granulates, Scientific Polymer Products) in a home made vacuum chamber which was intially evacuated to a pressure below 10^{-8} Pa.

Figure 3.1 shows the position of the different evaporators for the preparation

of metal-polymer nanocomposites. Two quartz crystal monitors were used for independent control of the deposition rates of metal and organic species. The metal atoms evaporated from evaporator source 1 was controlled with quartz 1. Whereas, the polymer which was evaporated simultaneously with the metal was placed at the middle and controlled by quartz 2.

Evaporation of metal and polymer at an incident angle of 60 $°C$ relative to the center of the substrate surface was used to achieve a metal concentration gradient in the composite film. This allowed to examine the optical and electrical properties of the nanocomposites within a wide range of metal contents prepared at the same conditions. Moreover, an angle incidence deposition helps to use the shadowing effect to cover even a very small portion of the substrate in μm label.

These composite films were deposited on different substrates (Silicon wafer, Glass, Kapton foil coated with evaporated aluminum or sputtered gold palladium, and/or carbon coated TEM grids). The variation in the substrate is due to the sample criteria for the characterization process. But to prevent the variation in thickness and microstructure of the composite films on the different substrate a thin film of polymer (10-15 nm) were deposited prior to the co-deposition. A typical sample setup for the deposition of metal-polymer nanocomposites was demonstrated in figure 3.15.

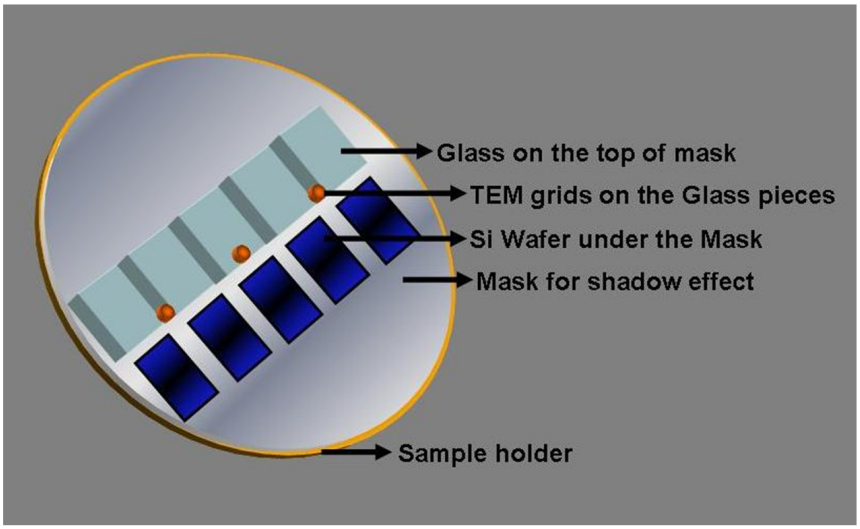

Figure 3.15: *Schematic of the typical sample setup for the deposition of nanocomposites.*

The physical properties of the metal-polymer nanocomposites is depend on the experimental parameters during deposition. The rate of deposition of both metal and polymer are the most significant parameters to determine the microstructure of the composites which are controlled during deposition. Moreover, one can also use the free parameters such as time of deposition and substrate temperature to control the microstructure of the film as well. A uniform rate of deposition is highly recommended for both materials in order to achieve a metal clusters uniformly distributed through out the polymer matrix in approximately uniform size and shape of the cluster.

The relative position of the sample on the sample holder has a significant role in both thickness and microstructure of the composite films. A normalized thickness plot of a metal and polymer films deposited on the substrate versus the position on the substrate holder along the axis of the two metal evaporators are shown in figure 3.16 (top). In addition, the thickness distribution perpendicular to the axis of the metal evaporators are shown in figure 3.16(below). The shape of the distribution curves were not varied for samples deposited at different rate of deposition and time for both metal and polymer films. Therefore, the gradient in the local deposition rate of metal and polymer on the substrate allows the production of composite films with various metal concentration in the film.

3.5.2 Preparation of bimetallic-polymer nanocomposites

The preparation of bimetallic clusters has been studied long ago by both chemical and physical deposition techniques with a large percentage of the contribution dedicated to the chemical process. Both techniques implement two basic strategies to wards the formation of bimetallic alloy nanoclusters.

1. Preparation of bimetallic clusters during the deposition processes
2. Preparation of a core-shell structure from a two step deposition and transfer in to an alloy clusters in various treatment

Link [51], Moskovits [52], and their co-workers prepared a Au-Ag alloy nanoparticles by co-reduction of metal salts consisting of Au and Ag using a reducing agent in a solution. Whereas, the preparation of core-shell structure

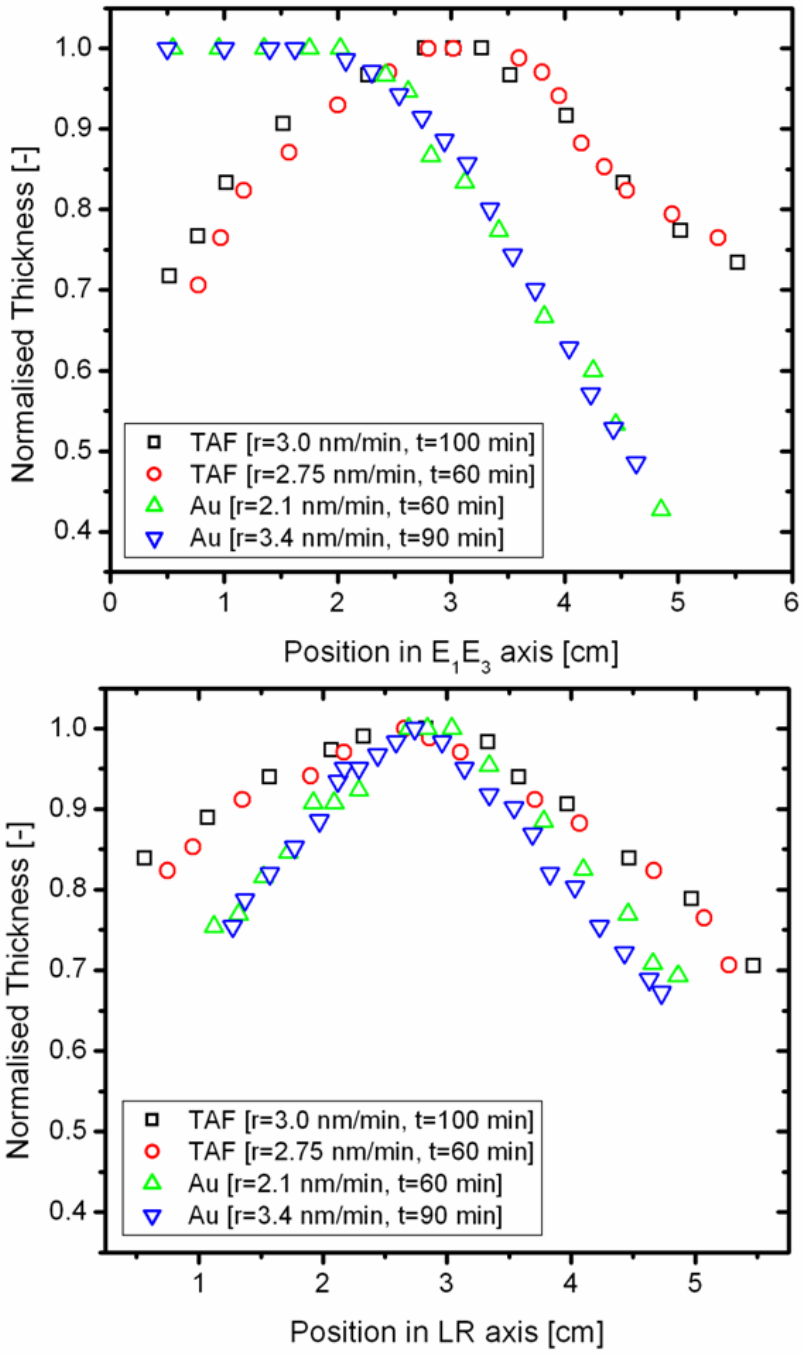

Figure 3.16: *Normalised thickness distribution of metal and polymer films along the axis of the two metal evaporators (top) and perpendicular to the axis of the metal evaporators (below).*

of Au and Ag by a two step reduction of metal salts and the transformation of this structure into alloyed nanoparticles using laser induced melting and chemical treatment were reported by Hodak [53] and Schierhorn [54], respectively. Nevertheless, these chemical methods were not successful to produce very small particles below 10 nm and involved many other draw backs [55].

Physical deposition techniques were also implemented to produce alloy nanoparticles in various researchers. Papavassiliou [56] was used evaporation of Au-Ag alloys of desired composition, which initially prepared by melting and mixing the Au and the Ag together in a silica crucible. Later Au-Ag and Ag-Cu bimetallic alloy nanoparticles were prepared by Cottancin [57]using laser-induced evaporation of an alloy target. Moreover, bimetallic clusters were produced by using alternative pulsed laser radiation from different targets by Gonzalo [58] and co-workers. The preparation of the Ag-Au core-shell structure prepared by using a two step evaporation method and transformation into completely alloyed bimetallic structure by heating the film at 300 $^{\circ}C$ was demonstrated by Baba [59] as well.

Here, in this work a novel technique was implemented to produce bimetallic alloy nanoparticles in different from the various research reports until now. Two different metals were evaporated from two distinct sources simultaniously. Two quartz crystal thickness monitors (1 and 2) were used to determine and control the rate of deposition of the metals independently during the experiment. A polymer was co-evaporated along with the two metals to support the three dimentional growth of alloy clusters and to be a dielectric host. The rate of deposition of the polymer was determined prior the co-deposition of all the three materials in one of the quartz monitors. This method of preparation allows one to produce bimetallic alloy nanoparticles with various alloy composition and metal concentration in the film in a well controlled manner. Independent control of the rate of deposition of metals during the co-deposition process makes our technique very interesting and effective for the production of bimetallic alloy nanoparticles in the polymer matrix.

In this work Au-Ag and Ag-cu alloy bimetallic nanoclusters in Teflon AF 1600 matrix were produced by co-evaporation technique explained above. The microstructure of this clusters and the physical properties will be discussed in

the following chapters.

The summary of materials used for polymer composites containing metal clusters during this work are given in the following table.

Table 3.1: *Materials used in this work*

Material	Description	Source	Form of use
Gold	wire ($purity = 99.99\%$, $d = 1\ mm$, $l = 1\ m$)	GoodFellow	Vapor deposited
Silver	wire ($purity = 99.99\ \%$, $d = 1\ mm$, $l = 1\ m$)	GoodFellow	Vapor deposited
Copper	wire ($purity = 99.99\ \%$, $d = 1\ mm$, $l = 0.5\ m$)	GoodFellow	Vapor deposited
Teflon AF 1600	granulate ($\rho = 19.8\ g/cc$, $M_w = 1\ mm$, $M_w/M_n = 1$)	DuPont	Vapor deposited
Poly-α-methylstyrol	granulate ($M_w = 9,000\ g/mol$)	Aldrich	Vapor deposited
Poly-methylmethacrylate	powder ($M_w = 35,000\ g/mol$, $M_w/M_n = 1$)	Scientific Polymer Products	Vapor deposited
Polyamid 6	granulate ($\rho = 19.8\ g/cc$, $M_w = 1\ mm$, $M_w/M_n = 1\ m$)	Scientific Polymer Products	Vapor deposited
Silicon	wafer ($d = 1\ mm$, $l = 125\ mm$, $t = 0.625\ mm$)	GoodFellow	Substrate
Glass	$dimensions = 76\ mm * 26\ mm$, $t = 1\ mm$	Eydam	Substrate
TEM-grid	carbon coated	Plano	substrate
Polyimid Kapton	foil ($\rho = 19.8\ g/cc$, $d = 1\ mm$, $l = 1\ m$)	GoodFellow	Substrate

4 Characterization

In the present chapter the fundamentals of the characterization methods for structural, chemical and physical properties of nanocomposites are briefly described. These includes, in situ film thickness monitoring using quartz crystal microbalance, postdeposition actual thickness measurement by profilometry, and relative atomic concentration measurements using energy dispersive x-ray analysis. Moreover, transmission electron microscopy is intensively used for the morphology characterization of the films. Functional properties particularly the optical and electrical behavior of the polymer-metal nanocomposites are investigated using UV-Visible spectroscopy and keithley picoammeter.

4.1 In Situ Film Thickness Monitoring

4.1.1 Quartz Crystal Microbalance

A quartz crystal microbalance (QCM) is a universally employed technique for in-situ monitoring of the thickness of the film. The QCM consists of a thin quartz crystal sandwiched between two metal electrods as shown in figure 4.1. Thus, an alternating electric field is applied across the crystal, causing vibrational motion of the crystal at its resonant frequency.

The basic working principle of the QCM is the converse piezoelectric effect in which application of a voltage across the crystal results in a corresponding mechanical strain. The crystal symmetry dictates that the strain induced in a piezoelectric material by an applied potential of one polarity will be equal and opposite in direction to that resulting from the opposite polarity. Application of an electric field across the crystal produces a shear strain proportional to the applied potential [60]. Therefore, an alternating potential across the crystal

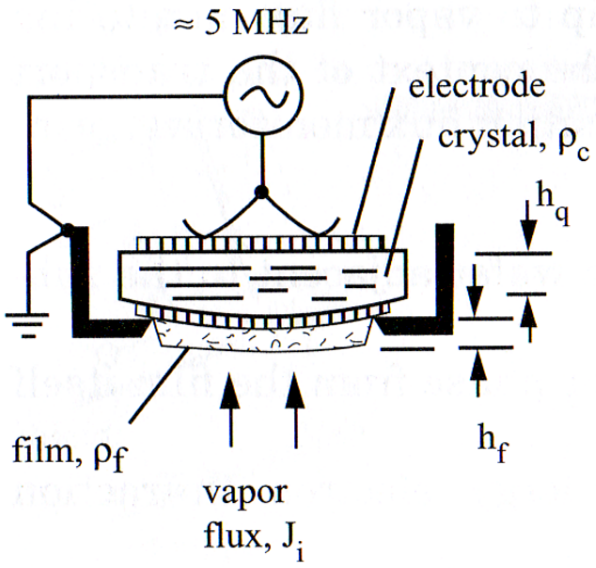

Figure 4.1: *Quartz-crystal deposition monitor in cross section*

causes vibrational motion in the quartz crystal with amplitude parallel to the surface of the crystal.

The extremely sensitive nature of the piezoelectric devices toward mass changes was first demonstrate by Sauerbey [61]. According to Sauerbeyts equation, the mass changes Δm at the surface of the QCM electrode surface causes a change in the oscillation frequency Δf of the crystal:

$$\Delta f = -C_f \, \Delta m \tag{4.1}$$

where C_f is the sensitivity factor for crystal used. Equation 4.1 relies on a linear sensitivity factor which is the fundamental property of the QCM crystal. In this case, the incremental change in mass due to the additional deposition is treated as though it was really increasing the thickness of the underlying quartz. The deposited film is considered to be rigid and so thin that it does not experience any shear forces during vibration.

The thickness of the film can be calculated by:

$$d_f = \frac{\Delta m}{\rho_f} \tag{4.2}$$

where d_f and ρ_f are the thickness of the film and the bulk density of deposited film, respectively. However, vacuum and gas phase thin film depositions exhibit more complicated frequency-mass correlations as shown in equation:

$$d_f = \frac{N_q \rho_q}{\pi \rho_f Z f_1} tan^{-}1 \left[Z \, tan \left(\frac{\pi (f_u f_1)}{f_u} \right) \right] \tag{4.3}$$

where N_q is the frequency constant of a quartz crystal, ρ_q is the density of the quartz ($2.684 g/cm^3$), f_1 and f_u are frequencies of loaded and unloaded crystals, respectively and Z is the Z-factor of the film material.

Rate computation is based on the rate of the change in thickness. However, instrumental calibration is affected by three different parameters, material density, material Z-factor, and tooling. Tooling is a deposition system geometry correction (location of sensor relative to substrates). Density and Z-factor are material factors.

The use of the material bulk density value will normally provide sufficient film thickness accuracy. In the case of Au, Ag, Cu, and Teflon, the Z-factors are given on the technical specifications of respective product. However, it is also possible to calculate the Z-factor by the following formula,

$$Z = \left[\frac{\rho_q G_q}{\rho_f G_f} \right]^{\frac{1}{2}} \tag{4.4}$$

where G_q and G_f are the shear moduli of the quartz and the film material (usually bulk values are taken for calculations), respectively. The accuracy of the mass load and thickness calculation mainly depends on how accurate the Z-factor and material density is known.
The correct tooling factor value is determined by:

$$Tooling\ \% = 100 \times \left(\frac{Substrate\,Thickness}{Displayed\,Thickness} \right) \tag{4.5}$$

4.2 Condensation Coefficient and Filling factor

During the co-evaporation process, the deposition rate of metal R_m and polymer R_p were monitored by two independent quartz crystal microbalance. The nominal or equivalent thickness $(R_m + R_p)t$, where t is the time of deposition, is a measure of the amount of composite film thickness. However, this result is not identical to the amount of composite film actually deposited onto the substrate. The actual measurement by surface profilometry is much lower than the quartz crystal microbalance and the difference is depend on the condensation coefficient, which is usually unknown, and needs to be determined. The condensation coefficient C, is defined as the ratio of the number of atoms actually deposited onto the surface to the total number of atoms arriving at the surface.

Previously, two different methods for determination of the condensation coefficient of metal atoms onto polymer surfaces were developed in our group. These include a very sensitive radiotracer method [62] and XPS method [63, 64]. In a radiotracer method, metal isotopes are evaporated onto polymer sample through an aperture, and re-emitted atoms are collected on a catcher plate ($C \approx 1$) which collects a constant fraction of the reemitted atoms as shown in figure 4.2. With this value, C follows from the ratio of the radioactivity on the catcher plate and on the sample. Moreover, sectioning of the catcher plate and counting the activity of the metal deposited on each section also yields the angular deposition of the reemitted atoms.

The second method XPS was developed in order to avoid the limitation of the first method of using radioactive isotopes. In this method intensities are calibrated by depositing metal atoms onto substrates such as metal or polyimide, where the condensation coefficient is known to be very close to unity at room temperature. This intensity acts as a point of reference and can be related to the nominal thickness monitored by the quartz microbalance. The XPS peak areas were used to calculate the C assuming the measured XPS intensity of a metal peak is proportional to the total number of metal atoms deposited on a surface. Cluster sizes are determined from intensity ratios of two metal X-ray photoelectron lines, which are well separated in their kinetic energy. The validity of this method was checked using the diameters of metal clusters obtained directly from TEM micrographs and shows a good agreement in all the cases.

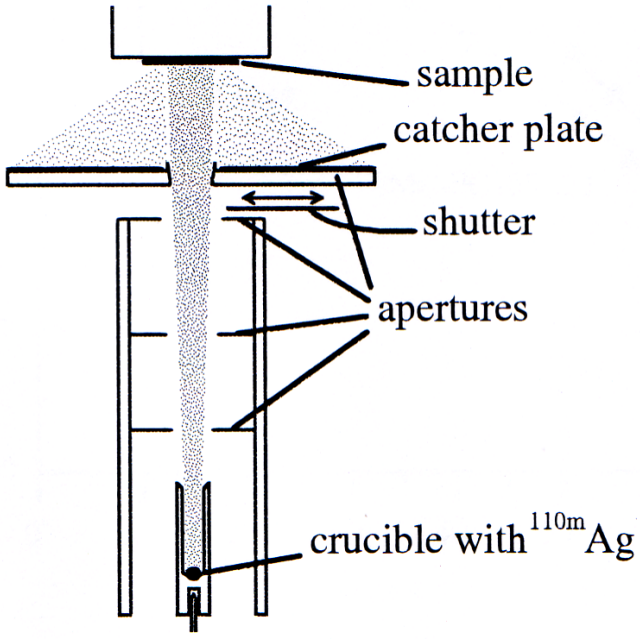

Figure 4.2: *Sketch of the setup for measuring condensation coefficients*

In this work, a third method is introduced to determine the condensation coefficient of metal atoms in polymers and the amount of metal volume concentration in the 3D composite films. As shown in the geometry of the deposition chamber in figure 3.1, metal deposition takes place at symmetrically opposite direction and at an incident angle of 60 ř relative to the substrate surface. This allows to determine the local rate of deposition of metal and polymer using a very thin narrow mask of width $0.75mm$ and thickness $0.33mm$ on top of the substrate. Thus, as a result of the shadowing effect, different regions that exposed only to the deposition of metal, polymer or both are exhibited. The microscopic picture and thickness profile in figure 4.3 clearly shows the thickness of pure metal and pure polymer film near the two opposite edges of the mask in a shadowed area of less than $30\mu m$ in width and the composite film around the mask. The sticking coefficient of metal atoms on metal and polymer molecules on polymers are known to be unity. Thus, the high Ag peak is due to the complete condensation of Ag on Ag. Whereas, the condensation coefficient of Ag on the growing composite is significantly very small to unity. Therefore, the local deposition rate of each component is determined from the pure metal and polymer film.

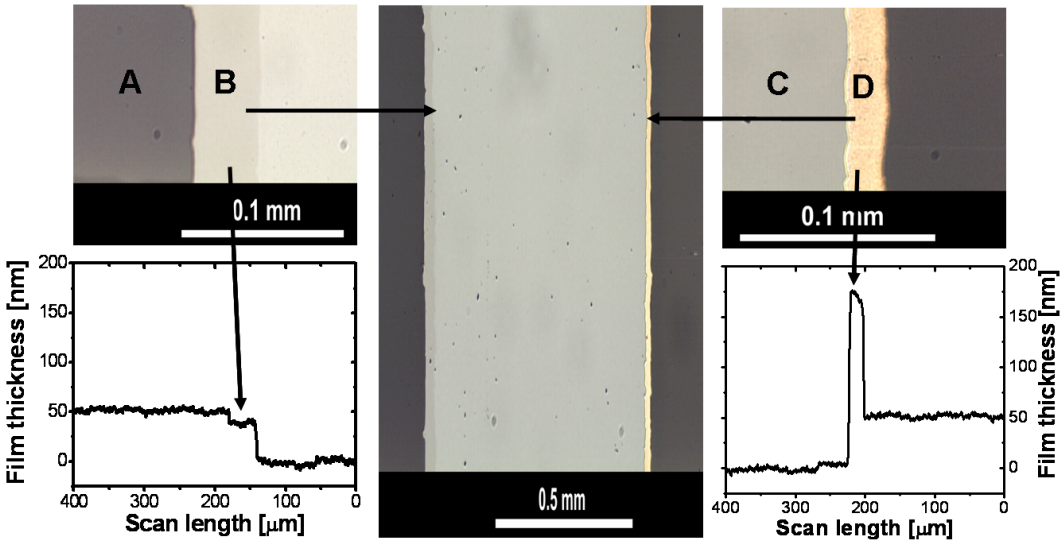

Figure 4.3: *Microscopic picture of Ag/Teflon nanocomposites around the masked region and the thickness profile to the left and right side of the mask. The various regions are (A) nanocomposite film, (B) Teflon film, (C) the substrate, and (D) Ag film.*

An energy dispersive X-ray Spectrometer (EDX) mounted in a scanning electron microscope (SEM) was used to determine the local atomic concentration of metal atoms in the composite films. A uniform metal film with the same thickness range as the composite film was used as the standard for EDX measurement. A comparison of the relative atomic concentration of the metal between the composite films and the standard film of known thickness is used to determine the atomic concentration in the composite film. The fluorescence and adsorption contributions in this range of film thickness ($40 - 70\ nm$) are very small, which was supported by the linear dependence of the metal intensities on the standard thickness.

Both the condensation coefficient of metals and metal content in the composite film were determined from the EDX analysis and thickness measurement by profilometry in combination. The condensation coefficient can be calculated from the ratio between the metal thickness in the composite film (determined from the EDX) to the pure metal peak at the edge of the mask (Profilometry). Similarly, the metal content in the composite can be determined from the ratio

of the thickness of the metal in the composite to composite film thickness.

The content of metal nanoparticles in the composite films, which was specified as a volume filling factor f usually determined from

$$f = \frac{\frac{m}{V} - \rho_p}{\rho_m - \rho_p}, \tag{4.6}$$

where ρ_p is the density of the polymer host, ρ_m is the density of the metal, m is the mass and V is the volume of the composite film. However, the experimental film thickness was too small to determine the concentration of metal in the film by weight measurement and the EDX method is considered to be more accurate.

Similarly, the filling factor and the atomic composition in bimetallic polymer composites can be determined from the EDX and Profilometry. The actual rate of deposition of the constituent metal atoms of the alloy can be found from the peak around the mask as shown in figure 4.4.

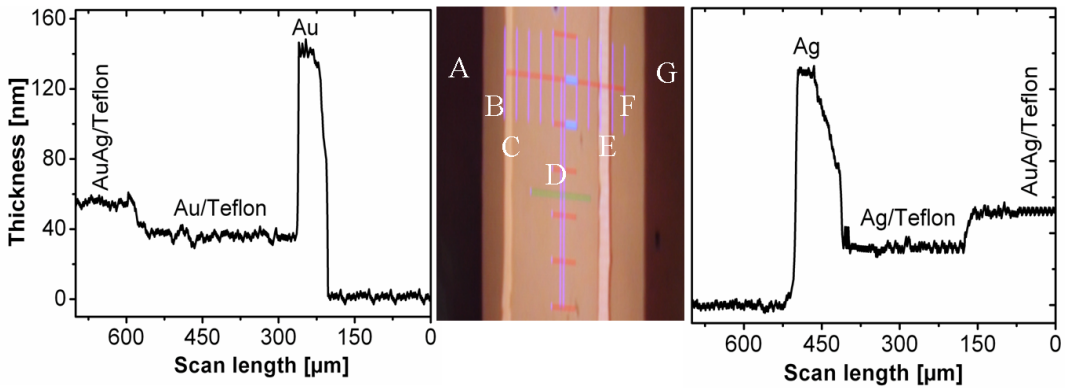

Figure 4.4: *The thickness profile of the nanocomposites around the two edges of the mask. The left side profile shows the thickness of the Au peak (C), the Au/Teflon (B), Ag-Au/Teflon (A), masked area (D), the Ag peak (E), the Ag/Teflon (F), and Ag-Au/Teflon (G). Photo of the deposited film around the mask was shown in the middle of the two side profile.*

4.2.1 Profilometry

Profilometry is a mechanical sensing system which measures roughness by the mechanical moment of a diamond stylus over the sample of interest as indicated in figure 4.4. In profilometry, the sharply pointed stylus has a direct contact to the surface and follows the height variations as the sample is moved. The height variations are converted into electrical signals, producing a profile. The resulting trace represents a cross-sectional view with height vertical resolution. The stylus force typically spans from 0.1 to 50 mg, enabling step heights from 0.5 nm to 800 μm. The radius of the stylus is 12.5 microns, and the horizontal resolution is controlled by the scan speed and scan length. There is a horizontal broadening factor which is a function of the radius of the stylus and of step height. This broadening factor is added to the horizontal dimensions of the steps. Moreover, the technique does not required a special sample preparation and almost any sample that will not be deformed by the stylus can be measured very rapidly.

In these experiments, the steps used for thickness measurement were made by a thin narrow width mask before the film deposition process. Additional scratching of the films after the deposition process was also used as a method of conformation but not as a main method to determine the thickness of the film.

Dektak 8000 profilometer (Veeco) was used for film thickness measurmants and calibration of monitored thickness. The instrument can measure small surface variations in vertical stylus displacement as a function of position. The system provides a maximum of $65,400$ data points per scan for high horizontal resolution and excellent baseline stability for superior measurement repeatability. However, the accuracy of stylus measurements is affected by substrate roughness which gives excessive noise into the measurement and the vibration of the equipment.

4.2.2 Energy Dispersive X-Ray (EDX) Analysis

An Energy Dispersive X-ray Spectrometer (EDX) mounted in a scanning electron microscope (SEM) (Philips X L30) was used to identify and determine the local content of metal in metal-polymer nanocomposite films.

When an electron beam (< 0.01 μm in diameter) strikes the sample and

dwells for a few microseconds interactions occur inside the sample. The interaction between the electron beam and the specimen is the basis of electron microscopy. These fast primary electrons interact in various ways with the surface layer of the specimen as shown in figure 4.5(left). The zone, in which such interactions occurs and in which different signals are produced, is called interaction volume (figure 4.5(right)). The interaction volume depends strongly on the applied acceleration voltage and the atomic number(s) of the element(s) in the specimen. The penetration depth of the electrons increases with increasing the acceleration voltage and decreases with increasing the atomic number. The shape of the interaction volume is dependent up on scattering processes by mean atomic number.

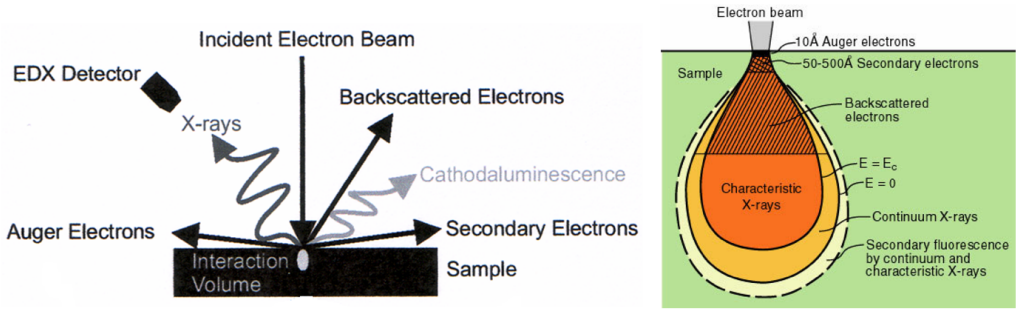

Figure 4.5: *The possible interactions of an incident electron beam and a sample (left), and the interaction volume (right).*

When a lower (usually K-shell) electron was emitted from the atom during the secondary electron process and an inner (lower energy) shell now has a vacancy. Thus, a higher energy electron can drop into the lower energy shell to fill the vacancy. This process leads to emit energy, usually X-rays, to balance the total energy of the atom (see figure 4.6).

The X-ray emission signal can be sorted based on energy in an energy dispersive X-ray detector. The detector used in EDX is the Lithium drifted Silicon detector. This detector is operated at liquid nitrogen temperatures. When an X-ray strikes the detector, it generates a photoelectrons within the body of the Si. As this photoelectrons travels through the Si, it generates electron-hole pairs. The electrons and holes are attracted to opposite ends of the detector with the aid of a

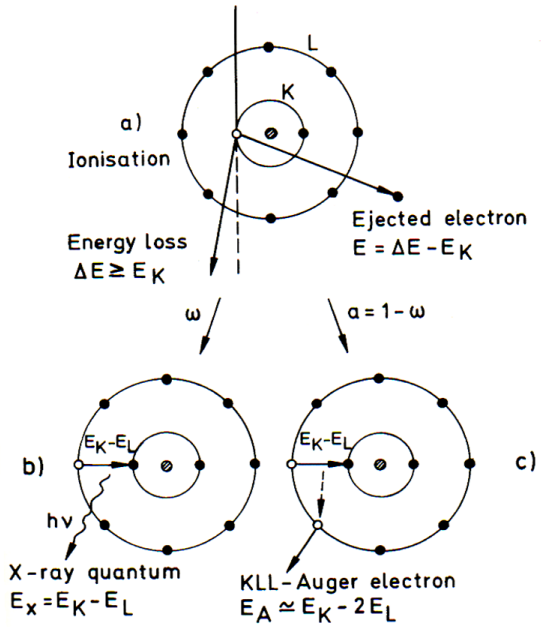

Figure 4.6: *Schematic representation of (a) the ionization process, (b) x-ray emission and (c) Auger-electron emission.*

strong electric field. The size of the current pulse thus generated depends on the number of electron-hole pairs created, which in turn depends on the energy of the incoming X-ray, and the composition of the sample. Thus, an X-ray spectrum can be acquired giving information on the elemental composition of the material under examination. By moving the electron beam across the material an image of each element in the sample can be acquired. These distributions are characteristics of the elements that produced them and the SEM can use those signals to produce elemental images that show the spatial distributions of particular elements in the field of view.

EDX was used for compositional analysis of the nanocomposites. Principally EDX is a microanalytical technique that uses the characteristic spectrum of x-rays emitted by the specimen after excitation by high-energy electrons to obtain information about its elemental composition. Determining the actual composition of the metal clusters in the film requires an analysis of the energies of the X-rays generated when the probe electrons interact with the sample atoms. The

characteristic X-rays have energies that are characteristic of the elements present in the sample. By identifying the emission lines in an acquired spectrum it is possible to determine which elements are present in the particulate sample.

Elemental concentrations of clusters and matrix can be determined from the relative intensity of the peaks in the X-ray spectrum. This is achieved by normalizing the number of X-ray counts in the peaks to a major peak or to the total number of counts after corrections have been made for peak overlap and X-ray background. The quantitative analysis of the film is carried out from the ratio of the characteristic x-ray intensity measured from the specimen to that measured from the standard. The measured intensity ratios between the specimen and the standard are roughly equal to the ratios of the mass or weight fractions of the emitting element,

$$\frac{C_i}{C_s} = \frac{I_i}{I_s} \tag{4.7}$$

where C_i and C_s are the composition in weight(mass) concentration of element i in the unknown and in the standared, respectively. The ratio of the measured unknown to standared intensities, I_i/I_s. However, a significant systematic deviation between the ratio of measured intensities and the ratio of concentrations are known in a homogeneous substances with multielement composition compared to pure element standards due to matrix effects. Using matrix effects, the most common form of the correction equation is

$$\frac{C_i}{C_s} = [ZAF]_i \frac{I_i}{I_s} \tag{4.8}$$

The term ZAF in equation 4.8 refers to the correction due to effect of atomic number (Z), X-ray absorption effect (A) and X-ray fluorescence. Nevertheless, for thin specimens from 30 to 80 nm in thickness a linear dependence of intensity with film thickness was observed which is an indication for the negligible contribution of these factors.

Figure 4.7 shows a typical example of EDX spectra of bimetallic nanocomposites at selected regions of the film around the masked area shown in figure 4.4

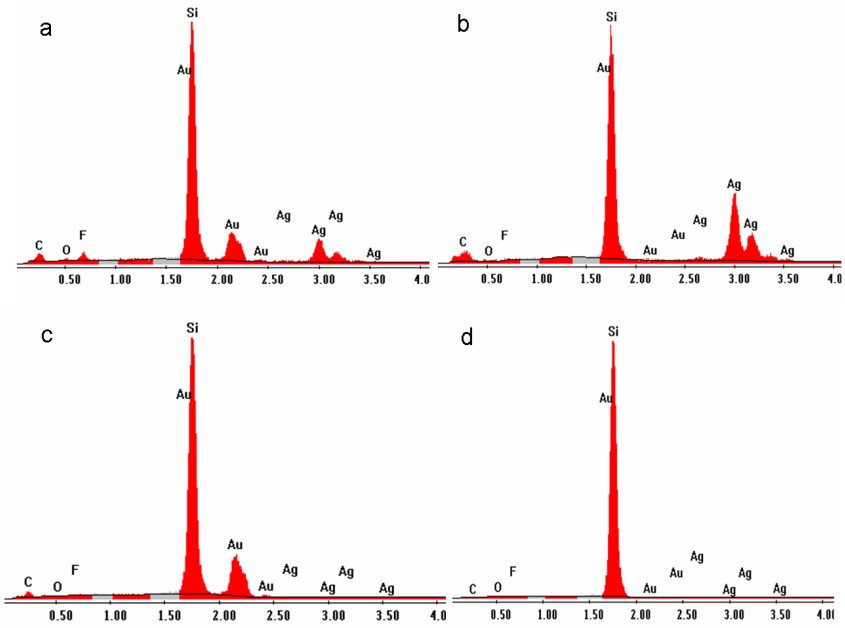

Figure 4.7: *EDX spectra for the regions around the mask (a) bimetallic polymer composites, (b) Ag standard film, (c) Au standard film, and (d) substrate (masked area).*

4.3 Morphology and Structural Characterization

4.3.1 Transmission Electron Microscopy (TEM)

Philips CM30 electron microscope with a maximum acceleration energy of 300 KeV was used to analyze the morphology (shape, size and size distribution of clusters) of the metallic clusters in thin polymer films. TEM offers a high resolution which extends to atomic dimensions and microscopy of thin film specimens.

In transmission electron microscopy (TEM) high energy electrons are used to irradiate thin specimens about 50 nm or less in thickness. The transmitted electrons form an image of the specimen magnified in several steps with the aid of electro-optical lenses and the entire image can be observed directly on a fluorescent screen (see figure 4.8). A detailed description of this technique can be found in [65, 66]

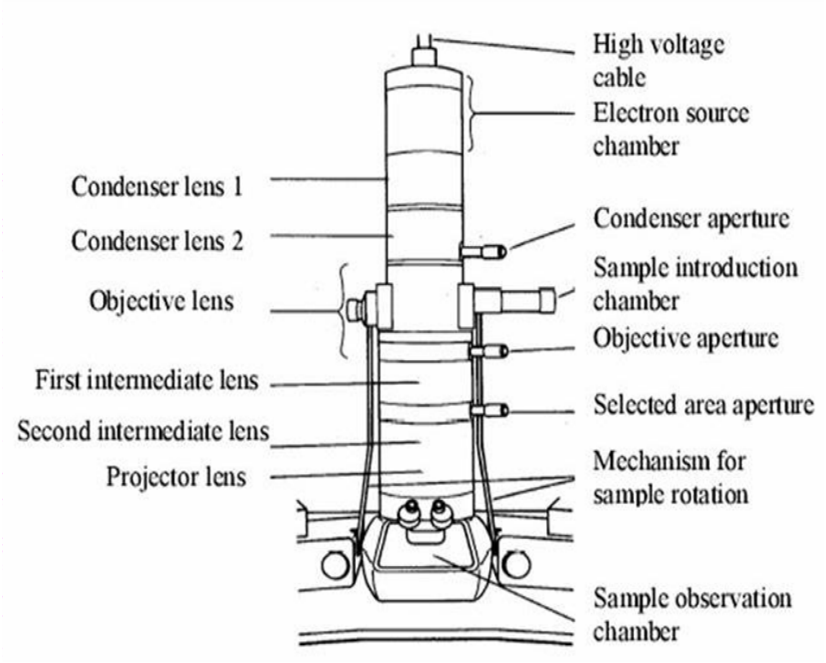

Figure 4.8: *Schematic of the Transmission Electron Microscopy (TEM)*

The electrons emitted from the electron gun are accelerated to an energy of $100-300\,KeV$. The condenser lens then shapes them into an approximately parallel beam which illuminates the specimen uniformly. The objective lens produces a first image, which then is further magnified by intermediate and projector lenses and is finally projected onto the fluorescent screen. The image can be recorded on a plate by exposing the photographic emulsion, or as in our case by CCD camera, which allows further digital picture processing.

There are two very broad modes of TEM operation, namely imaging and analytical (figure 4.9). In the former, structural images ranging from low magnification to atomic resolution are directly revealed, whereas in the later structural information is indirectly revealed through analysis of diffracted beam geometries and energies.

The image contrast is generated by the incident electrons that are elastically scattered (Bright-field) or diffracted (Dark-field) in the specimen by small angles as shown in figure 4.10. In most cases, only electrons penetrating the spec-

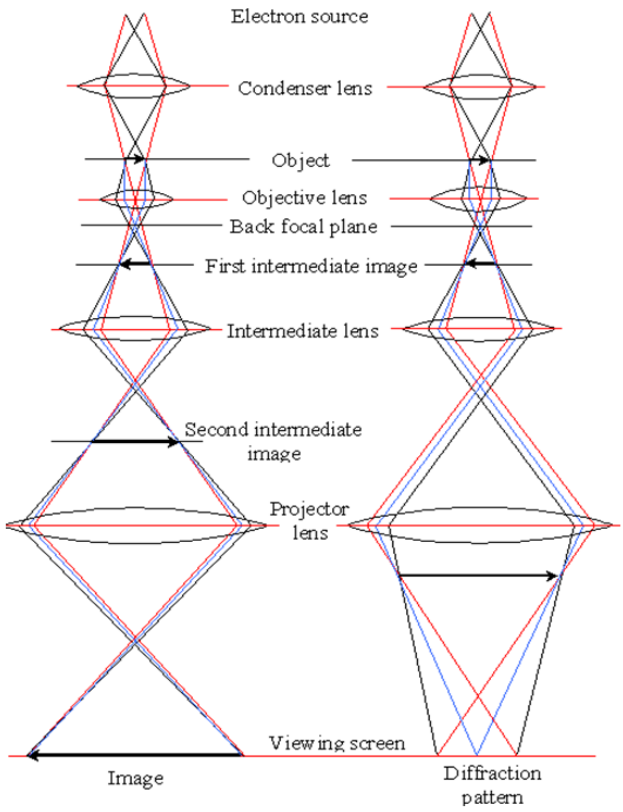

Figure 4.9: *Ray diagram for a TEM in the image mode (left) and selected area diffraction mode (right).*

imen without scattering are used for image formation. The adjustable objective aperture limits the scattering angle of the electrons to the order of 1 *mrad* and allows only the direct beam to pass through. Since the scattered or diffracted electrons are excluded, any changes in the intensity of the transmitted beam due to inhomogeneities in the specimen with respect to density, thickness, and orientation create an image contrast. Bright-field imaging provides a distinct image contrast available when scattered or diffracted beams are excluded by means of an objective lens. The dark-field image is obtained by selection of certain diffracted beams using beam tilting or objective aperture displacement. This is used for imaging specimen regions of specific orientation, structure or composition.

The nanocomposite films were consists of polymers with low atomic weight elements and metallic clusters of high atomic weight elements. As a result metallic

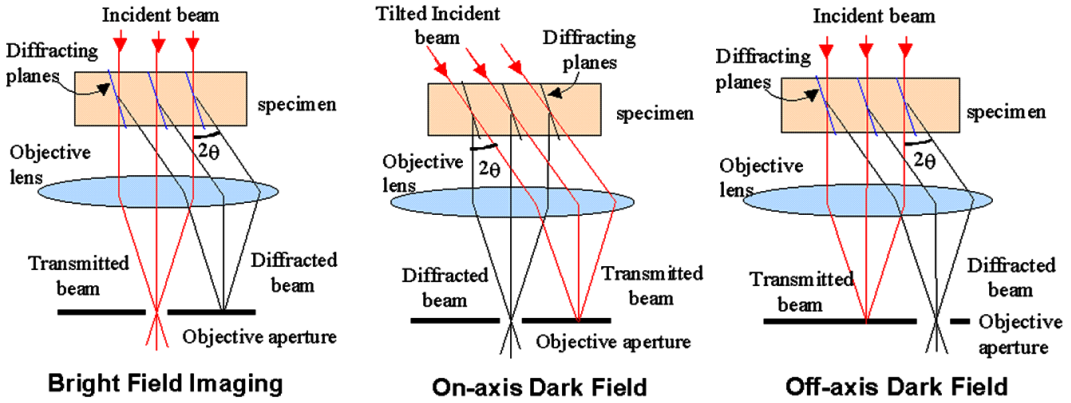

Figure 4.10: *Ray diagram for bright filed imaging and dark field imaging.*

clusters with a higher atomic number exhibited a larger scattering which leads a cluster to appear as dark than the polymer film.

4.4 Optical and Electrical Characterization

4.4.1 UV-Vis Spectroscopy

Ultraviolet and visible (UV-VIS) absorption spectroscopy is the measurement of the attenuation of a beam of light after it passes through a sample or after reflection from a sample surface. Absorption measurements can be at a single wavelength or over an extended spectral range. Ultraviolet and visible light are energetic enough to promote outer electrons to higher energy levels, and UV-VIS spectroscopy is usually applied to molecules or inorganic complexes in solutions or organic matrices.

The UV-VIS spectra have broad features that are of limited use for sample identification but are very useful for quantitative measurements. The concentration of an element in a matrix can be determined by measuring the absorbance at some wavelength and applying the Beer-Lambert Law. Matter can capture electromagnetic radiation and convert the energy of a photon to internal energy. This process is known as absorption. Energy is transferred from the radiation

field to the absorbing species. We describe the energy change of the absorber as a transition or an excitation from a lower energy level to a higher energy level. Since the energy levels of matter are quantized, only light of energy that can cause transitions from one level to another will be absorbed. Indifferent with the IR spectroscopy in which absorption is caused by molecule oscillations, absorption in the UV-Vis spectroscopy is due to electronic transitions.

When an atom or molecule absorbs energy, electrons are promoted from their ground state to an excited state. In a molecule, the atoms can rotate and vibrate with respect to each other. These vibrations and rotations also have discrete energy levels, which can be considered as being packed on top of each electronic level. Absorption spectroscopy is one way to study these energy levels of the atoms, molecules, and solids. An absorption spectrum is the absorption of light as a function of wavelength. The spectrum of an atom or molecule depends on its energy-level structure, making absorption spectra useful for identifying compounds.

Since the UV-VIS range spans the range of human visual acuity of approximately $400 - 750\ nm$, UV-VIS spectroscopy is useful to characterize the absorption, transmission, and reflectivity of a variety of technologically important materials, coatings, thin films and filters. This more qualitative application usually requires recording at least a portion of the UV-VIS spectrum for characterization of the optical or electronic properties of materials.The UV-VIS spectral range is approximately 190 to 900 nm, as defined by the working range of typical commercial UV-VIS spectrophotometers. Nevertheless, a high-end commercial UV-VIS spectrophotometers extend the measurable spectral range into the NIR region as far as 3300 nm.

The light source is usually a deuterium discharge lamp for UV measurements and a tungsten-halogen lamp for visible and NIR measurements. The instruments automatically swap lamps when scanning between the UV and visible regions. The wavelengths of these continuous light sources are typically dispersed by a holographic grating in a single or double monochromator or spectrograph. The spectral bandpass is then determined by the monochromator slit width or by the array-element width in array-detector spectrometers. Spectrometer designs and optical components are optimized to reject stray light, which is one of the

limiting factors in quantitative absorbance measurements. The light beam is redirected automatically to the appropriate detector when scanning between the visible and NIR regions. The diffraction grating and instrument parameters such as slit width can also change.

In this work, UV/Vis/NIR-spectrometer Lambda900 (Perkin Elmer) was used to determine the absorbance, transmittance or reflectance of nanocomposite films prepared on a glass substrate. In this case, the monochromatic light simply passes through the sample, and a single detector measures the final intensity (I). The initial intensity is that which passes through "blank" sample (I_o). In double-beam instruments, the light is split (usually by a chopper or low-height mirror) between the sample and a reference. Two detectors simultaneously measure the two separate intensity values. Detectors are usually just photomultiplier tubes, but other types may also be used.

The light intensities weaken themselves with the passage by a material in accordance with the Bear Lambert law, which can be used to determine the concentration of the absorbant materials.

$$I = I_o e^{-\alpha(\lambda)CL}, \tag{4.9}$$

and The Beer-Lambert equation, $A = \alpha CL$, relates absorbance with the molar absorption coefficient (α), the concentration of the element in the sample (C), and the sample path length (L).

The intensity of the light beam after exiting the sample (I) is measured to determine the absorbance (A) of the sample according to the following relationship:

$$A = log\left(\frac{I}{I_o}\right) \tag{4.10}$$

,
The absorption of the light during the passage through material is not the only cause of the weakness of the light intensity, but also due to dispersion and reflection. Thus, Extinction (Absorption + reflection) is the total light attenuation by a sample. However, the extinction is equivalent with the absorption for nanostructures of size below $15\,nm$, at which the light reflectance is negligible.

4.4.2 Resistance measurment devices

The resistance measurment of the nanocomposite thin films were carried out using a Keithley Picoammeter 6485 as shown in figure 4.11(top). A constant voltage of 0.6 mV was applied across the gold-paladium contact film (about 60 nm) via the nanocomposites as shown in figure 4.11(bottom), and the current through the contacts was measured by the Picoammeter. The sensitivity of the Kiethley 6485 is in the range of 10 PA to 1 mA.

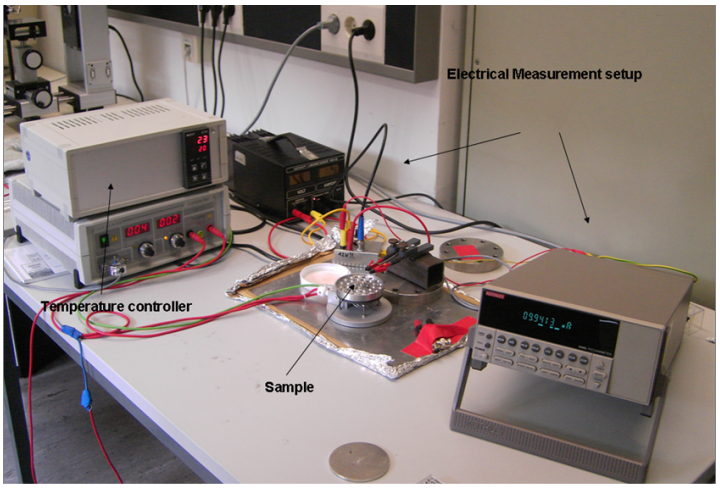

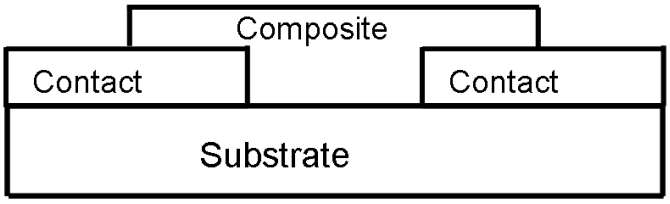

Figure 4.11: *Image of the setup used for recording the current through the composite film (top) and schematic drawing of the film preparation for the resistance measurement (bottom).*

A high voltage would lead to a very high current density and eventually destroy the metal nano-clusters on the device. Thus, a home made voltage controller was used to provide a constant output.

5 Nucleation and Growth of Metal Nanoclusters in Polymers

5.1 Introduction

The synthesis of metallic nanoclusters in a polymer matrix described in this work is based on co-deposition of two extremely dissimilar materials (metals and polymers). Metals are densely packed crystalline solids with high cohesive energy, whereas polymers are made up of large covalently bonded macromolecules held together by very week mostly only van-der-Waals type interactions in an open structure [67]. The cohesive energy of metals is typically two orders of magnitude higher than the cohesive energy of polymers. Moreover, the interaction between moderately reactive metals and polymers is generally much weaker than the strong metal metal binding forces. These distinctions of physical properties lead to a strong aggregation tendency of metal atoms and the formation of nanoclusters. These metallic nanoclusters of low reactivity exhibit no intermixing with the surrounding polymer matrix due to extremely low solubilities in polymers under equilibrium conditions. Thus, a controlled synthesis of nanocomposites require a full understanding of the atomic processes responsible for the nucleation and growth of metallic clusters in polymers. To understand this process an empirical model was developed to describe the nucleation and growth processes. The schematic diagram of processes and characteristic energies in nucleation and growth of metal clusters on polymer surface are shown in figure 5.1(left).

The various competing processes during the nucleation and growth of metal clusters on polymer surfaces are systematically investigated and reported in more detail by Faupel et al [67, 68]. Here in this work the co-deposition process is

described based on the model proposed for a tandem process of metal deposition on a polymer surface. In this case, the nucleation and growth of nanoclusters taking place during the tandem deposition can be considered as process taking place at a particlualr time of deposition and thickness of the film during the film growth.

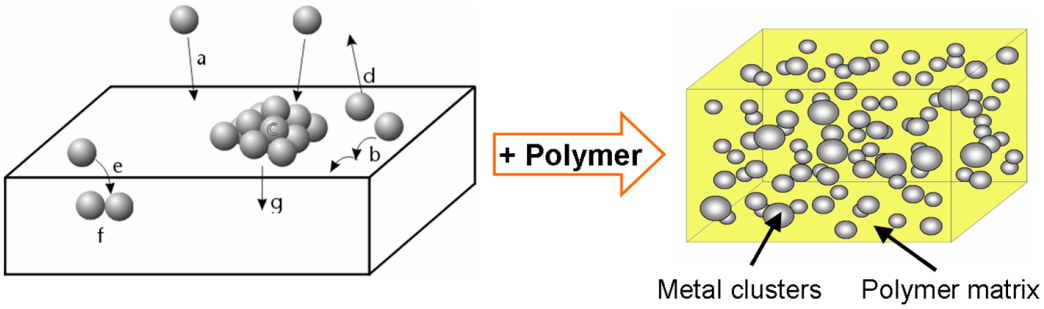

Figure 5.1: *Processes taking place at an instantaneous time of deposition and thickness of nanocomposites during the film growth where isolated metal atoms impinge on the growing polymer surface. The arriving atoms (a) may perform a random walk on the surface (b). In their diffusion path, metal atoms encountering each other may perform aggregates at the surface (c) or reemitted into the vacuum (d). Moreover, metal atoms can be diffuse into the growing polymer film (e) and form aggregates in the polymer film (f). Metal clusters may also be embedded into the polymer (g).*

The energetic vapor metal atom impinge on the simultaneously growing polymer surface with the thermal energy they have gained during evaporation and quickly loose this energy into the surface upon arrival. Hence, these atoms which imping on the polymer surface, did not get reflected directly back into the vacuum, rather they usually remain on the surface and migrate over the surface randomly for a length of time τ_s given by [69, 70]

$$\tau_s = \frac{1}{\nu} exp \frac{E_{des}}{kT}, \tag{5.1}$$

where ν (typically 10^{12} s^{-1}) is an atomic vibration frequency, E_{des} is the energy required to desorb back into vacuum, k is Boltzmanns constant and T the temperature. During its residence time, the metal atom is capable of diffusing a

mean distance χ from the site of incidence given by

$$\chi = \sqrt{2D_s\tau_s}. \tag{5.2}$$

The surface diffusion coefficient D_s is essentially

$$D_s = \frac{1}{2}{a_0}^2 \nu exp\frac{-E_s}{kT} \tag{5.3}$$

and therefore

$$\chi = a_0 exp\frac{E_{des} - E_s}{2kT} \tag{5.4}$$

where a_0 is an atomic dimension and E_s is the activation energy for surface diffusion.

Since typically E_{des} is several times E_s, (χ/a_0) can be large at suitably low temperatures. As a result, during the migration over the surface, the adatoms will encounter other atoms and are captured by a surface site. Depending on the size of the binding energy between these atoms and their areal density, they will form critical clusters, which may then grow to form large and stable clusters of atoms. This binding energy between atoms and the energy of critical clusters are centrally important to the understanding of nucleation and growth processes [71].

There are two extreme cases for metal nucleation on a polymer surface, preferred nucleation and random nucleation [72]. Preferred nucleation and random nucleation refers where nuclei are formed due to metal atoms trapped at preferred sites and by metal atom encounters, respectively. The density of the nuclei depends on these nucleation processes (preferred or random nucleation), the surface diffusion coefficient and the sticking coefficient. Their contribution to metal cluster formation is highly dependent on the experimental parameters, mainly the rate of deposition and the substrate temperature as well as on the particular metal-polymer combination (surface energy) [73]. If metal atoms impinge on metal surfaces their sticking coefficient is generally very close to unity [74]. The sticking coefficient is defined as the ratio of the number of atoms sticking on the surface to the total number of metal atoms arriving at the surface [73]. For metals this is some times more appropriately termed the condensation coefficient C. In order to understand the influence of deposition parameters on

the cluster densities, it is necessary to distinguish between two regimes of metal condensation (incomplete and complete condensation). In complete condensation ($C = 1$) clusters are formed at lower temperatures by random nucleation and it is deposition rate dependent. In contrast, polymers with incomplete condensation $C < 1$ at room temperature show a significant lower and non deposition rate dependent cluster density, indicating preferred nucleation at defect sites.

The probability to find a preferred site is proportional to the mean distance that they diffuse on the surface. If χ is greater than the average distance d between two neighboring sites, its probability to find a preferred site is unity. If not, the probability is assumed to be equal to χ/d. Thus, the condensation coefficient C of metal on polymer surfaces, can be expressed as

$$C = \begin{cases} 1, & \chi \geq d \\ \chi/d, & \chi < d \end{cases} \tag{5.5}$$

The measured condensation coefficient only depends on the number of trapped atoms on the polymer surface. Therefore, the condensation coefficient is closely related to the probability of finding a surface site with sufficient binding energy to remain adsorbed on the surface [75, 76]. This can be a preferred site on the polymer surface or a nucleation site. These preferred sites include impurities, defects, terminal groups or attractive arrangements of the polymer chains, which are related to the surface roughness of the polymer and significantly dependent upon the temperature. When an atom arrives at the surface, its probability to find a trapping site is related to the density of these sites. The larger the number of nucleation sites N, the smaller the average distance between the growing clusters. As a result, the condensation coefficient increases since the condensation probability is controlled by surface diffusion. The condensation coefficient can be expressed as

$$C \propto {N_c}^{1/2} exp \frac{E_{des} - E_s}{kT}, \tag{5.6}$$

where N_c is the number density of the growing clusters.

The physical and chemical properties of such composite films are usually dependent on the film microstructure. To obtain a composite film with the desired properties, it is necessary to manipulate the microstructure of the film, i.e film

thickness, size and concentration of the dispersed metal particles and the spatial distribution of the particles in the composite film. These parameters depend on the condensation coefficient of metal atoms, and itself depend on the rate of deposition, metal-polymer combination and the metal nucleation. Moreover, one must suppress the formation of any undesirable clusters of inhomogeneous sizes. Therefore, knowledge of the nucleation and growth processes of metal atoms in polymers will be mandatory prior to their use in functional applications.

5.2 Results and Discussion

5.2.1 Growth of monometallic nanoclusters in polymers

In this section, several examples of metal-polymer combinations are considered in order to demonstrate the possible controlled synthesis of metallic clusters in a polymer matrix: Au/Teflon, Au/PAMS, Ag/Teflon, Ag/Nylon, and Ag/PMMA. To prevent the formation of metallic layers at the early stages of the film growth; the substrates are coated by thin polymer films prior to the co-deposition.

In simultaneous deposition, the nucleation and growth of metallic clusters in polymers are strongly depend up on the rate of deposition of both constituents: metal and polymer. Therefore, the ratio between the rate of deposition of metal and polymer is a very important parameter to describe the film growth. Figure 5.2 shows the volume fraction of Au and Ag nanoparticles versus the ratio of deposition rates for different polymers. As a result, the metal filling factor depends on the condensation coefficient of metal atoms on a given polymer surface as well as on the metal-polymer deposition rate ratio.

Practically, it was observed that the filling factor of metal in the polymer matrix increases linearly with the increase in the ratio r of the deposition rates of metal (R_m) to polymer (R_p). The slope of the plots is proportional to the value of the condensation coefficient of metal atoms on the given polymer hosts. Early in the deposition process and at low rate of deposition the cluster density increases rapidly due to the formation of new nuclei. Later and at a high rate of deposition the formation of new nuclei becomes negligible and the growth of already existing clusters dominates. Therefore, the condensation coefficient of

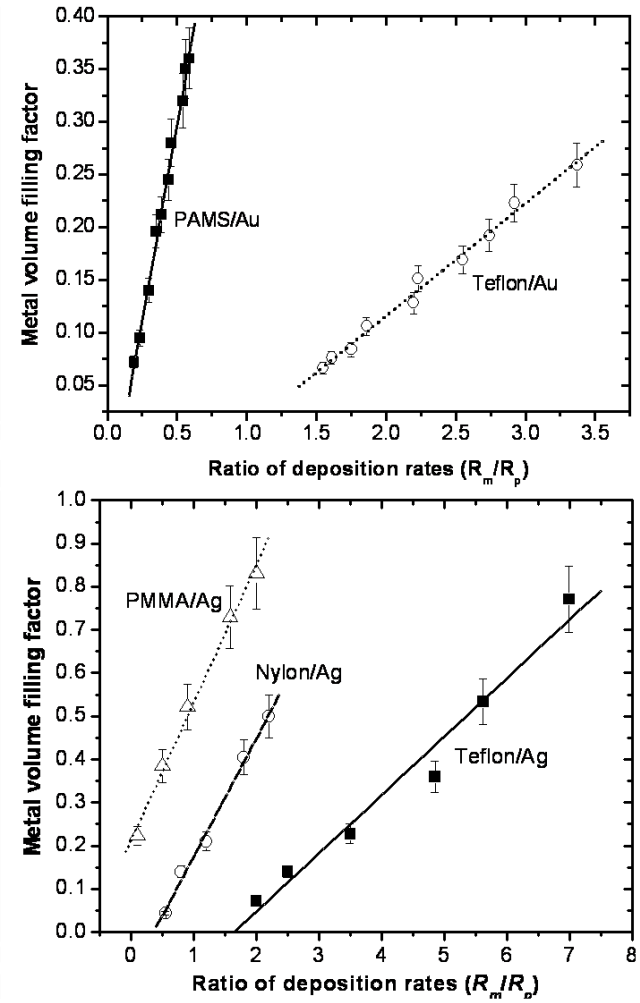

Figure 5.2: *Metal volume filling factor versus ratio of deposition rates of Au to Teflon and PAMS (top); and Metal volume filling factor versus ratio of deposition rates of Ag to Teflon, Nylon and PMMA (bottom).*

metal atoms increases with an increase in the rate of deposition. At higher metal coverages, metal atoms increasingly impinge on metal clusters and finally the condensation coefficient approaches unity.

On the other hand, an extremely large difference in the condensation coefficient of metal atoms in various polymers were observed. For instance, the condensation coefficient of Au atoms in PAMS is about 0.3 at low $r < 0.25$ and

increases rapidly to unity at $r \sim 1.5$. Whereas the condensation coefficient of Au atoms in Teflon is extremely low (smaller than 0.03) even at $r \sim 1.5$ and increases slowly up to 0.1 at a high metal-polymer deposition ratio of $r = 3.5$. Similarly, large differences in the Ag filling factors in PMMA, Nylon, and Teflon are indicated for the similar metal-polymer ratio, which is an indication for differences of the condensation coefficient of Ag atoms in these polymers. The difference in the condensation coefficients of metal atoms in polymers follows the trend of the surface energies of the polymers. Teflon has a surface energy of only $15.7\,mJm^{-2}$ and PMMA has $41\,mJm^{-2}$. A low surface energy impedes macroscopic wetting of the surface, it does not appear unreasonable that a low surface energy also impedes atomic condensation. Therefore, The large difference in the condensation coefficient may be due to the differences in the chemical interaction, i.e a favorable interaction of the metals with PAMS and PMMA with aromatic and carbonyl groups, respectively, and an unfavorable one with the fluoro groups of Teflon. Therefore, the favorable interaction with the polymer functional groups dominates the condensation of the metals on the polymers and the introduction of fluorine is not detrimental to the condensation behavior of the metals [62].

The TEM images of nanocomposites at various polymer matrices and metal volume concentration are shown in figures 5.3 to 5.7. Noble metals deposited at room temperature into polymers show Volmer-Weber type of growth. i.e., they do not wet the polymer surface around but form three-dimensional spherical clusters. The density and size of these clusters depend on the deposition parameters as well as the metal-polymer combination. In the case of random nucleation the variation of the deposition rate of the metal shows significant effects on the density and size of the clusters. A high deposition rate leads to a high stationary concentration of metal atoms diffusing on the surface of growing polymer surfaces in such a way that the probability for the formation of critical clusters increases. Consequently, the cluster density increases with an increase in the rate of deposition and reaches a maximum during the nucleation period. Later, the density of the clusters drop as a result of cluster coalescence which results an increase in the size of the clusters continuously with an increase in the rate of deposition. Similarly, the average distance between the clusters (interparticle distance) depends strongly on the cluster density. With increasing the density of the clusters, the interparticle distance becomes smaller.

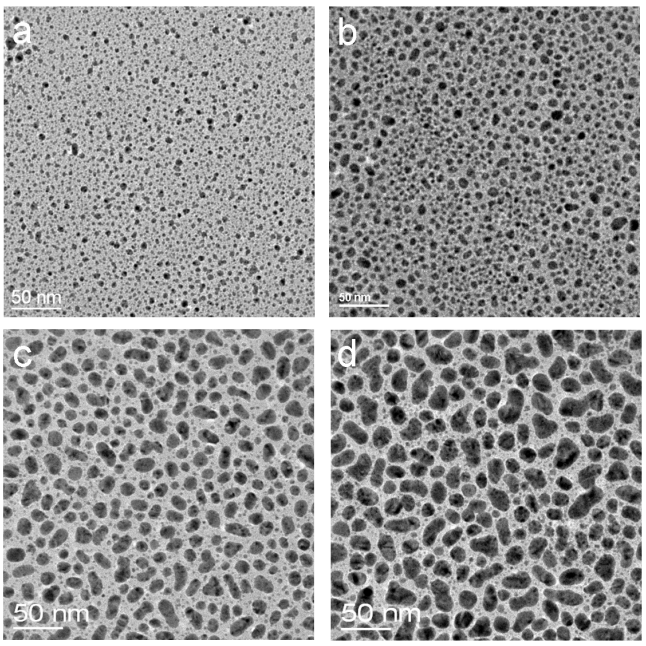

Figure 5.3: *TEM micrograph of Au/Teflon nanocomposites at various metal filling factors. (a) 0.08, (b) 0.16, (c) 0.25, and (d) 0.35.*

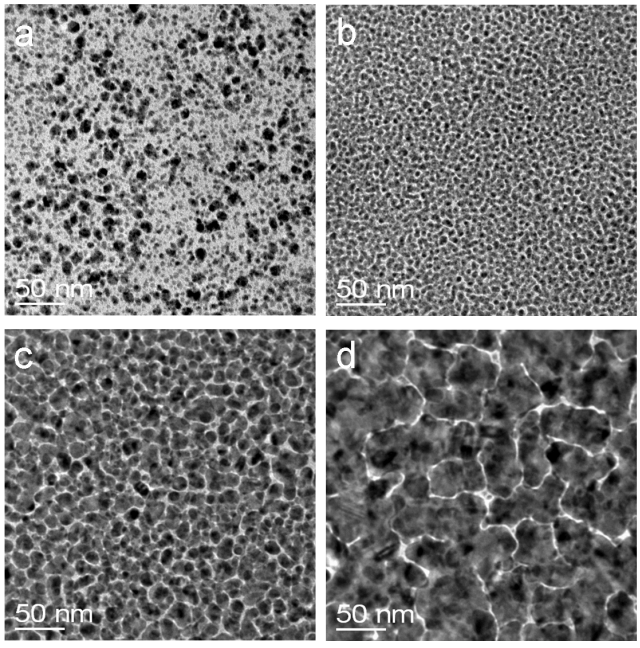

Figure 5.4: *TEM micrograph of Au/PAMS at various metal filling factors. (a) 0.05, (b) 0.12, (c) 0.21, and (d) 0.38.*

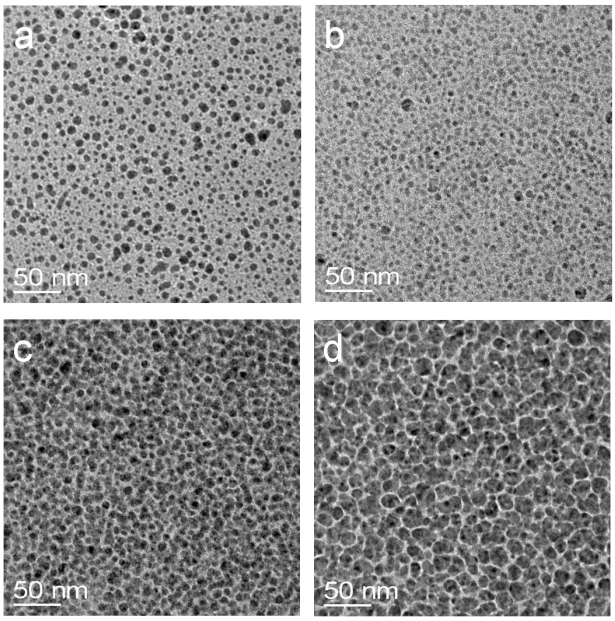

Figure 5.5: *TEM micrograph of Ag/Teflon at various metal filling factors. (a) 0.072, (b) 0.14, (c) 0.21, and (d) 0.36.*

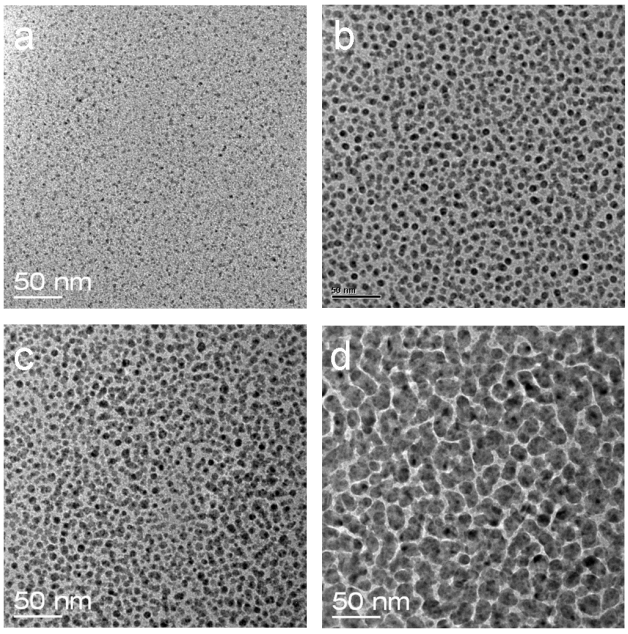

Figure 5.6: *TEM micrograph of Ag/Nylon at various metal filling factor. (a) 0.044, (b) 0.14, (c) 0.21, and (d) 0.405.*

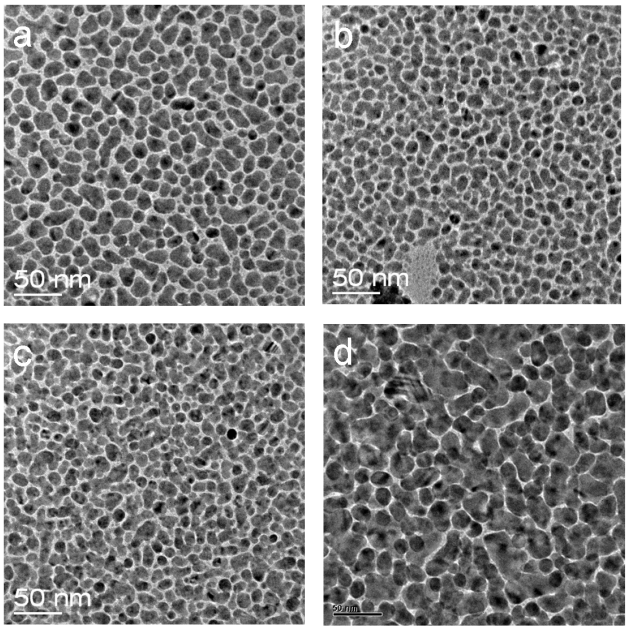

Figure 5.7: *TEM micrograph of Ag-PMMA at various metal filling factors. (a) 0.17, (b) 0.22, (c) 0.30, and (d) 0.38.*

5.2.2 Effect of temperature on the nucleation and growth of metal nanoclusters

To address the nucleation and growth of metal-polymer nanocomposite films completely, two key experiments, namely the influence of the substrate temperature during deposition and the effect of subsequent annealing were carried out. Teflon nanocomposites containing Au and Ag were considered to study the effect of temperature on the microstructure of the nanocomposites.

The condensation coefficients of Au and Ag in Teflon at room temperature are very small as reported in section 5.2.1. Furthermore, the condensation coefficient of these metals decrease to extremely smaller value due to an increase in the substrate temperature during deposition. As shown in figure 5.8, while the substrate temperature increases to the glass transition temperature of Teflon film ($140\,^{\circ}C$), the re-emission of adatoms due to thermally activated desorption increases due to the competition between thermal desorption and diffusion controlled nucleation. As a result, the cluster density decreases upon an increase

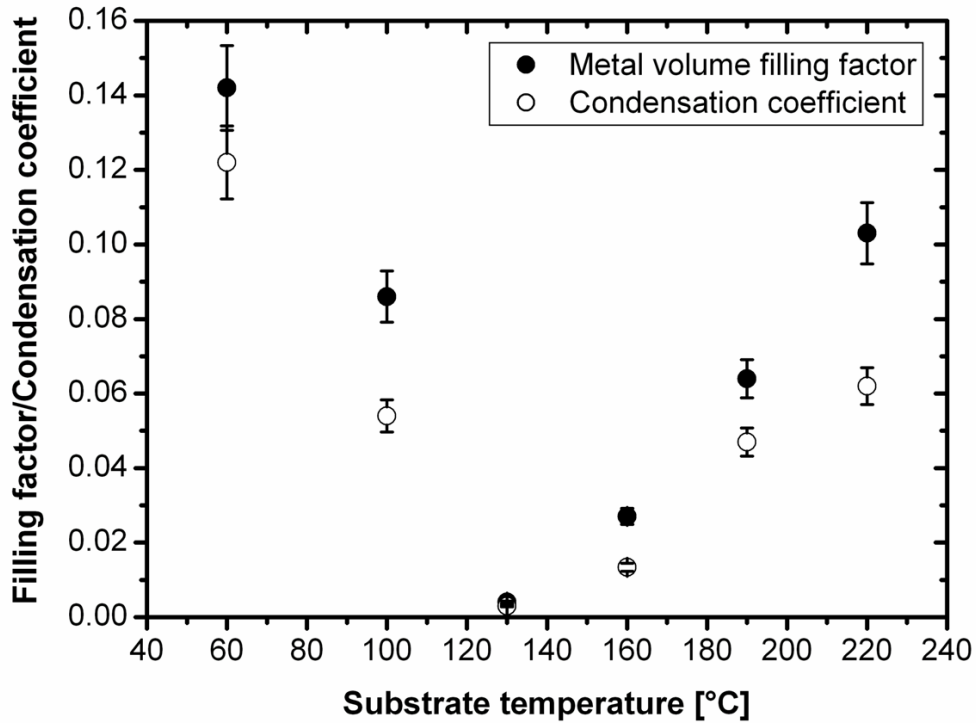

Figure 5.8: *Metal volume filling factor (•) and condensation coefficient (○) of Au/Teflon nanocomposites versus substrate temperature for a metal/polymer deposition ratio of 2.6.*

of the substrate temperature. In other words, the condensation of metal atoms drops since the probability for the adatoms to reach the clusters before they desorb becomes smaller as the distance between the clusters increases. The reduction in the glass transition temperature of polymer films as compared to the bulk material is reported before [77, 78]. This is because of the change in the polymer structure upon evaporation such as a reduction in molecular weight and a difference in m to n ratio of the self stabilized monomers (where m is tetrafluoroethylene(TFE) and n is perfluoro(2,2-dimethyl-1,3-dioxole)(PDD)). Moreover, the surface effect in thin films is known to reduce in the glass transition temperature of the polymer.

At a temperature above the glass transition temperature, micro-Brownian motion of the Teflon moleculer segments is released and the growing polymer film behaves like viscous fluid [79–81]. This leads to enhance the mobility of metal atoms on the growing polymer surface before desorption. On the other hand,

embedding of metal atoms into the growing polymer matrix and/or embedding of clusters formed at the surface can be the cause for the coalescence and growth of clusters inside the polymer matrix at high temperatures [82, 83]. It is known that, metal clusters which are formed on the surface were found to be embedded into the polymer upon heating above T_g, where the polymer chains attain long-range mobility [68, 84, 85]. The driving force for this process is the lowering of the high surface energy of the metal clusters. The high cohesive energy of metals gives rise to a correspondingly high surface Gibbs free energy of metal particles. The Gibbs free energy of a metal particle inside the polymer is lower than that of the particle at the surface, and it can be reduced by embedding into the polymer matrix. Following the embedding process, metal atoms coalesce together due to a preferred metal-metal interaction than metal-polymer molecules. As a result, a difference in the microstructure of Teflon composites prepared at various substrate temperatures below and above T_g were demonstrated as shown in figure 5.9 and figure 5.10 for Au/Teflon and Ag/Teflon nanocomposites, respectively.

Moreover, the very pronounced differences between metals and polymers are reflected in a post deposition heat induced change of microstructure in a metal polymer nanocomposite. The size and shape of nanoclusters in a polymer matrix which are prepared at room temperature can be changed by heat treatment at elevated temperatures [86]. This is due to metal diffusion in the polymer matrix that contrasts distinctly with interdiffusion between two materials that are more alike and exhibit appreciable mutual solubility. In addition, the availability of extremely large free volume, which exceeds ten percent in typical amorphous polymers plays an important role in the diffusion of the clusters [87, 88].

Figure 5.11 shows the TEM images of Ag nanoclusters in Teflon heat treated at various temperatures in air atmosphere. Upon annealing the cluster size increases and the cluster density decreases. Since the composite films are heat treated far below the metal boiling point, the cluster growth does not appear to occur by ordinary Ostwald ripening [89]. However, a temperature induced mobility of smaller clusters and cluster coalescence is the cause for the growth phenomena. Simply on the basis of size effects, smaller particles are known to have larger chemical potentials than those of larger particles, and thus the thermodynamic stability favors the formation of larger particles [90, 91].

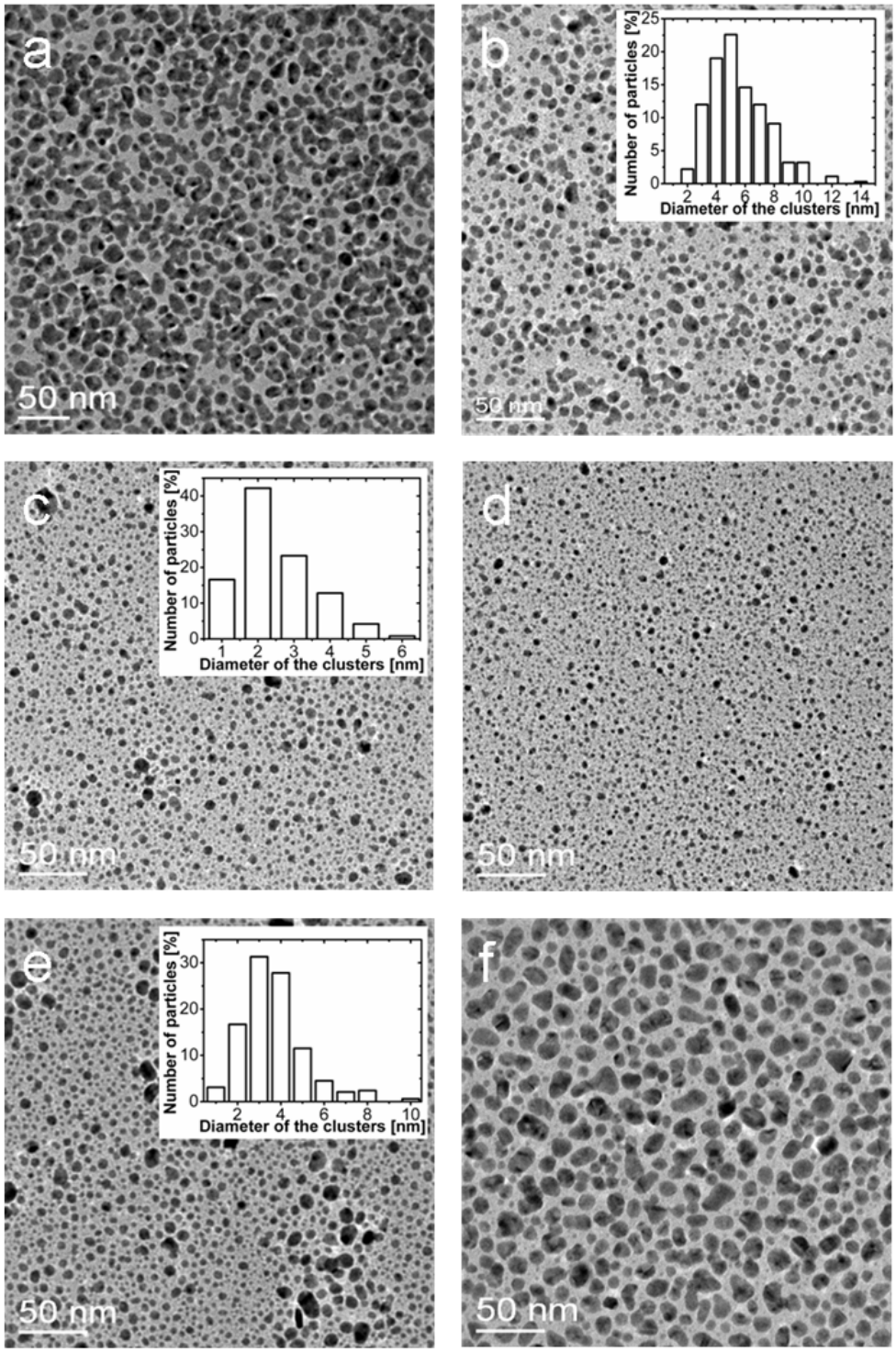

Figure 5.9: *TEM images of Au-Teflon nanocomposites co-deposited at different substrate temperatures (a) room, (b)* $100\,°C$*, (c)* $130\,°C$*, (d)* $190\,°C$*, (e)* $220\,°C$ *and (f)* $250\,°C$*. The mean diameter of the cluster size for* $100\,°C$*,* $130\,°C$ *and* $220\,°C$ *are 5.56 nm, 2.48 nm and 3.67 nm, respectively.*

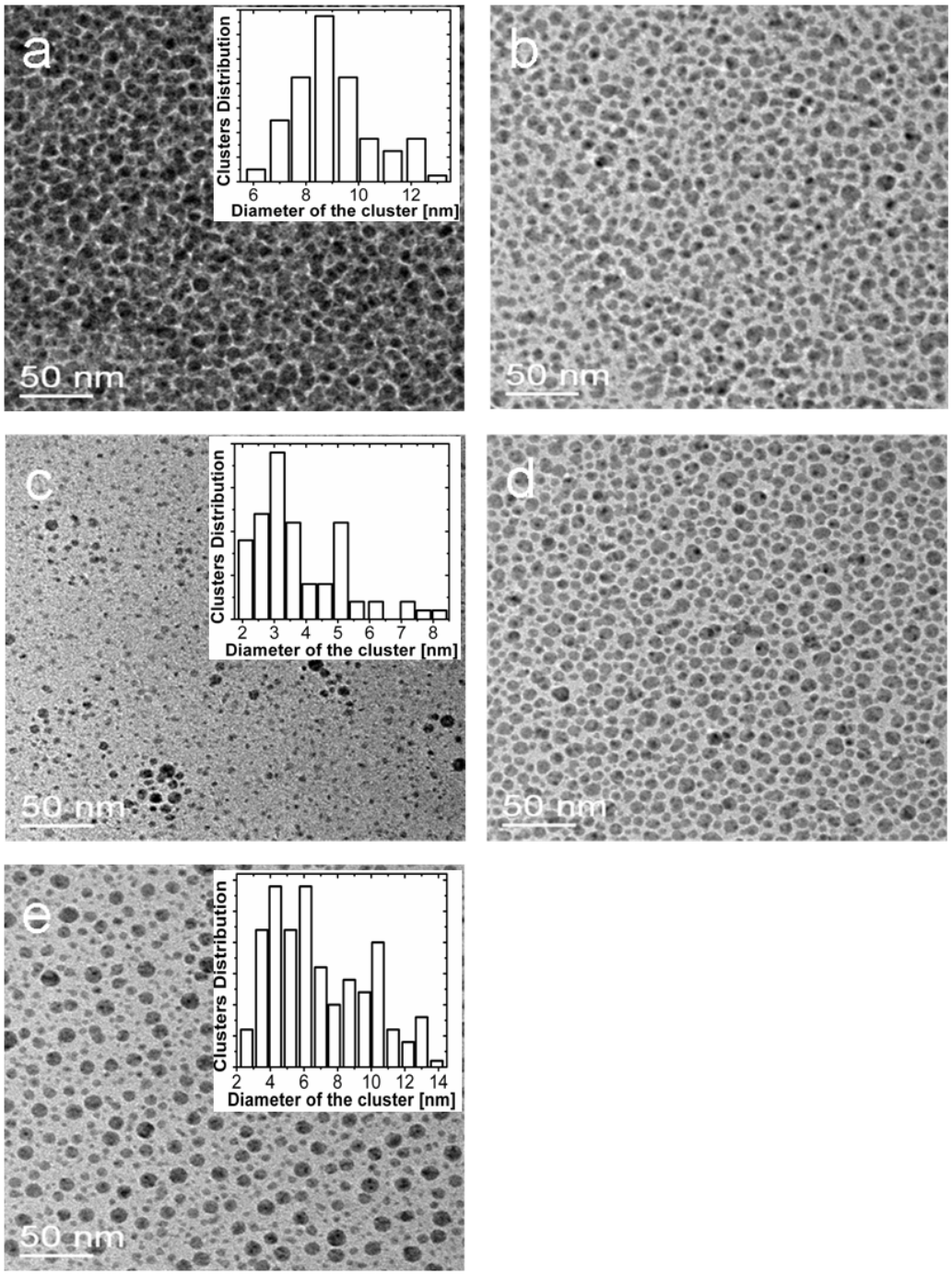

Figure 5.10: *TEM images of Ag-Teflon nanocomposites co-deposited at different substrate temperatures (a) room, (b)* $90\,^{\circ}C$*, (c)* $140\,^{\circ}C$*, (d)* $190\,^{\circ}C$ *and (e)* $240\,^{\circ}C$*. The mean diameter of the clusters for samples prepared at room,* $140\,^{\circ}C$ *and* $240\,^{\circ}C$ *are 9.0 nm, 3.76 nm and 6.9 nm, respectively.*

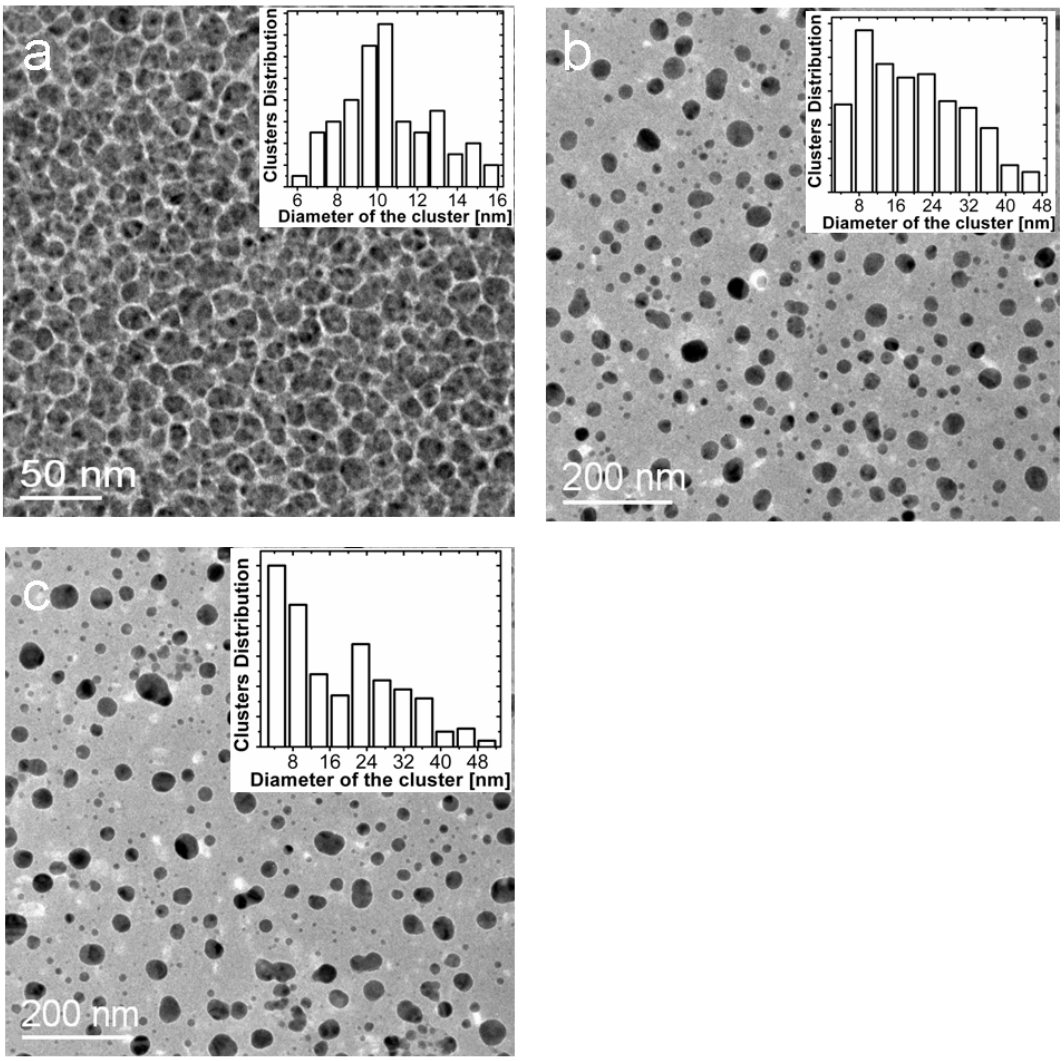

Figure 5.11: *TEM micrograph of Ag/Teflon nanocomposites ($f = 0.36$) as deposited (a), heat treated at $200\,°C$ for 2 min (b) and 64 min (c).*

In addition, a comparison between (b) and (c) of figure 5.11 shows the variation of the microstructure of Ag-Teflon nanocomposites which were annealed at $200\,°C$ in air atmosphere for different time interval. The results of the TEM analysis indicates that the average cluster size increases with annealing time. A strong reduction of the cluster density is also observed in the first stage of the annealing process, which is due to the thermal instability of clusters of smaller

size [92]. For systems containing both large and smaller particles, the difference in the chemical potential causes diffusional material redistribution from smaller to larger particles. Particle growth is therefore governed by the diffusion coefficient of metal clusters which is related with the average size.

5.2.3 Growth of bimetallic nanoclusters in polymers

In the case of co-deposition of two different types of metal atoms along with the polymer, the condensation coefficient of one type of metal atom is not depend only on the ratio of the metal to polymer deposition rate as in case of monometallic clusters [93, 94]. In addition one have to consider the ratio between the deposition rate of the constituent metal atoms. Therefore, the synthesis of bimetallic nanoclusters in a polymer with a specific alloy composition and filling factor needs to consider various parameters.

Figure 5.12(top) show the Au composition in bimetallic Ag-Au increases linearly with an increase in the ratio of the deposition rate of the metals (Au/Ag) at approximately $0.1\,nm/min$ rate of deposition of Teflon. One must consider that the condensation of metals can be varying from 0.05 to unity with an increase in the rate of deposition relative to the rate of deposition of the polymer. Moreover, the condensation coefficients of one of the constituent metals are also depend on the rate of deposition of the other constituent metal. As shown in figure 5.12(bottom), an increase in the composition of Au in the alloy lead to enhancement of the condensation of Ag. This is likely due to the strong interaction of two metal atoms. Hereafter the alloy composition (x) refers to the atomic percentage of Au and Cu in the Ag-Au and Ag-Cu bimetallic nanoclusters, respectively. The alloy filling factor (f) is also referred to the amount of bimetallic Ag-Au or Ag-Cu nanoclusters in the composite films, essentially the volume fraction.

The morphology of bimetallic composites are related with the composition and the alloy filling factor as shown in figure 5.13 and 5.14 for Ag-Au/Teflon and Ag-Cu/Teflon, respectively.

In both types of composites at low Au or Cu alloy composition the mean diameter of the bimetallic nanoparticles did not exhibit a large difference with a variation in composition. However, a much higher size difference and alloy filling

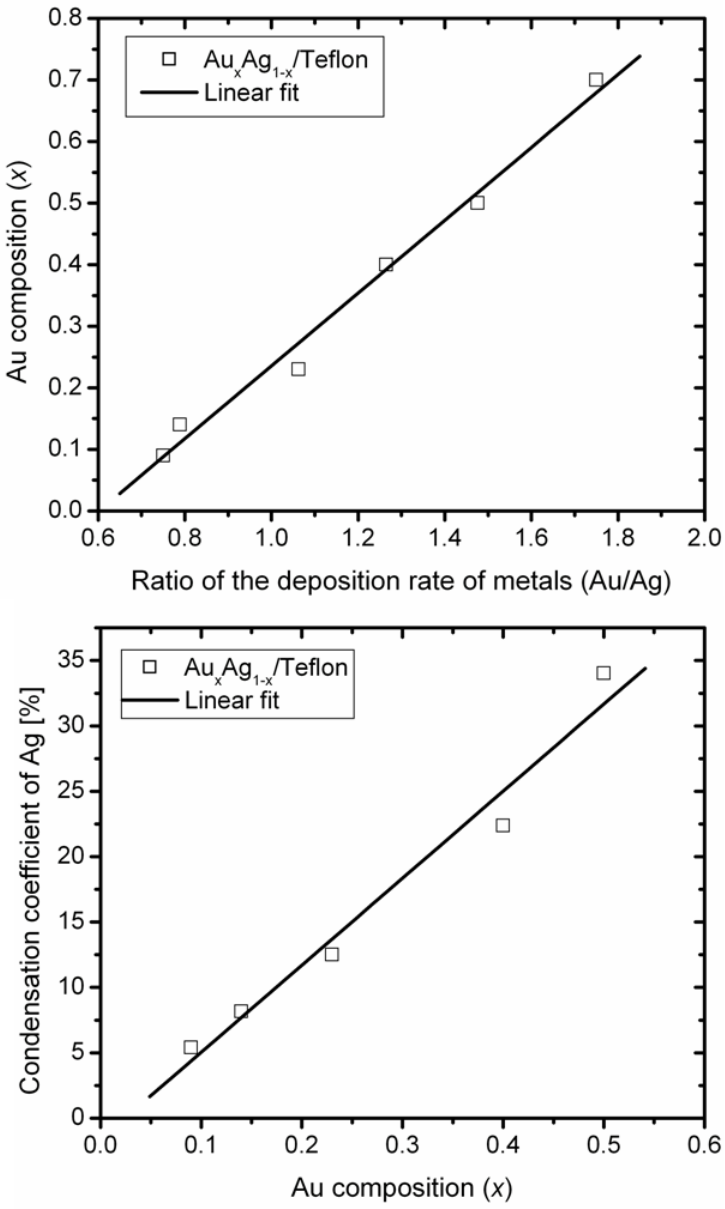

Figure 5.12: *The Au composition versus the ratio of the deposition rate of metals (top) and Ag condensation coefficient versus the Au composition (bottom).*

factor were observed with increase in the alloy composition for $x > 0.4$ in case of Ag-Au/Teflon. For $x > 0.4$, the filling factor increases in the range from 13 to 40 % with an increase in the Au content. In co-evaporation processes, an increase

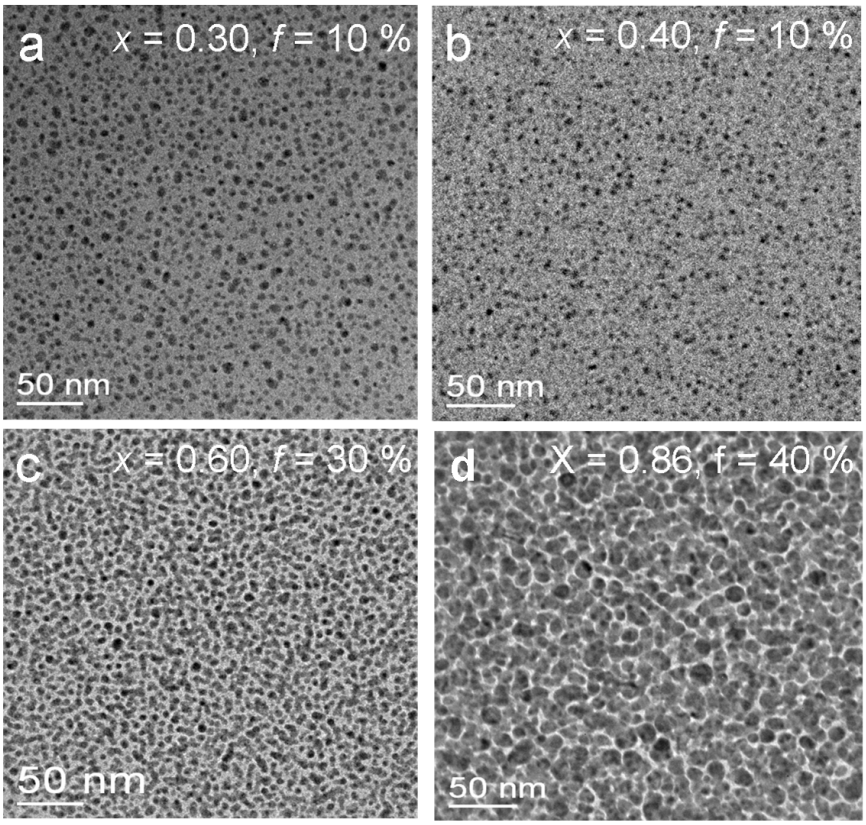

Figure 5.13: *TEM micrograph of $Ag_{1-x}Au_x$ nanoclusters in Teflon at various alloy composition and filling factor.*

of the metal content in the polymer matrix leads to an increase in the size of the clusters as well. Thus, the possibility to control and vary the filling factor and size of the clusters independently is difficult in such a system.

Now, however, it is not clear, whether such co-deposition of two metals lead to the formation of alloy nanoclusters or not. But, both Ag (4.09 Å) and Au (4.08 Å) have nearly the same lattice parameters as compared to Cu (3.61 Å) so that alloy formation can be more favorable for Ag-Au than Ag-Cu. Therefore, there is a definite possibility for the synthesis of bimetallic alloyed Ag-Au nanostructures and it is very probable for a segregated nanostructures from immiscible elements(see figure 5.15) such as Ag and Cu in the nanoscale [95]. Moreover, the large difference in the condensation coefficient of Cu than Ag on Teflon surface might lead to the formation of core-shell nanostructures especially at high rate of

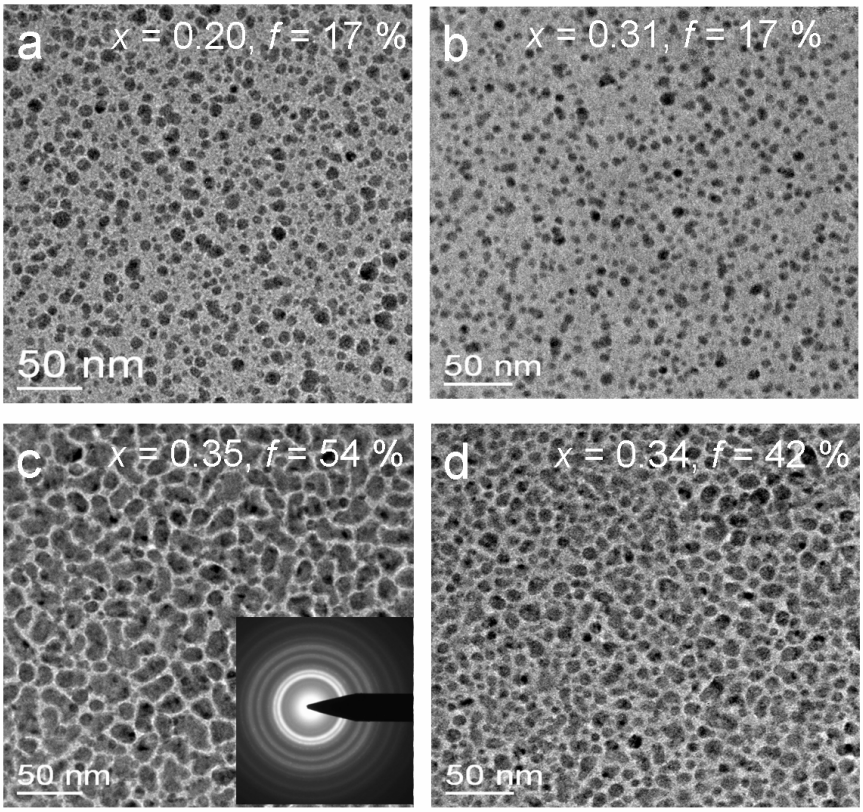

Figure 5.14: *TEM micrograph of $Ag_{1-x}Cu_x$ nanoclusters in Teflon at various alloy composition and filling factor. The corresponding diffraction rings for sample (c) shown in the inset.*

deposition. Therefore, the Cu with higher condensation coefficient as compared to the Ag would have a great probability to act as nuclei for the growth of the core-shell structure. Ag atoms with a higher diffusion mobility than Cu can be attached to the surface of Cu clusters as a shell. In fact, both the formation of alloy and core-shell nanostructures did not investigated in other means except optical analysis described in the next chapter.

The effect of post deposition heat treatment of Ag-Au/Teflon nanocomposites on the change in their microstructure was also studied in the same fashion as Ag-Teflon and Au-Teflon composites. Likewise, the size of the bimetallic nanoclusters increase as shown in figure 5.16. The mechanism of cluster coalescence and the change in the microstructure of the composites are described previously

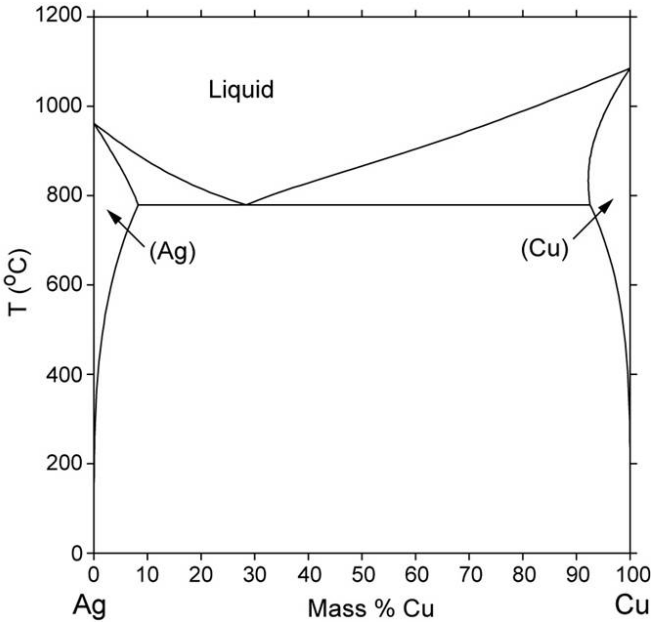

Figure 5.15: *Calculated phase diagram of Ag-Cu system*

in section 5.2.2.

5.3 Conclusion

The growth of metallic nanoclusters in polymers is taking place between materials which have strongly contrasting properties. This leads to the aggregation of the high cohesive metals and formation of spherical nanoclusters in the polymer matrices. The cluster density, size and shape of the clusters are strongly dependent on the condensation coefficient of metals on polymers. During the co-evaporation process, the condensation coefficient depends on the ratio of the deposition rate between metal and polymer, the type of metal-polymer combination, substrate temperature and the nucleation density. It is investigated that the condensation coefficient increases with an increase in the ratio of deposition rate of metal to polymer regardless of their metal-polymer combination. Increasing the substrate temperature during the deposition leads to a decrease in the condensation coefficient up to the glass transition temperature of the polymer and increases beyond this temperature.

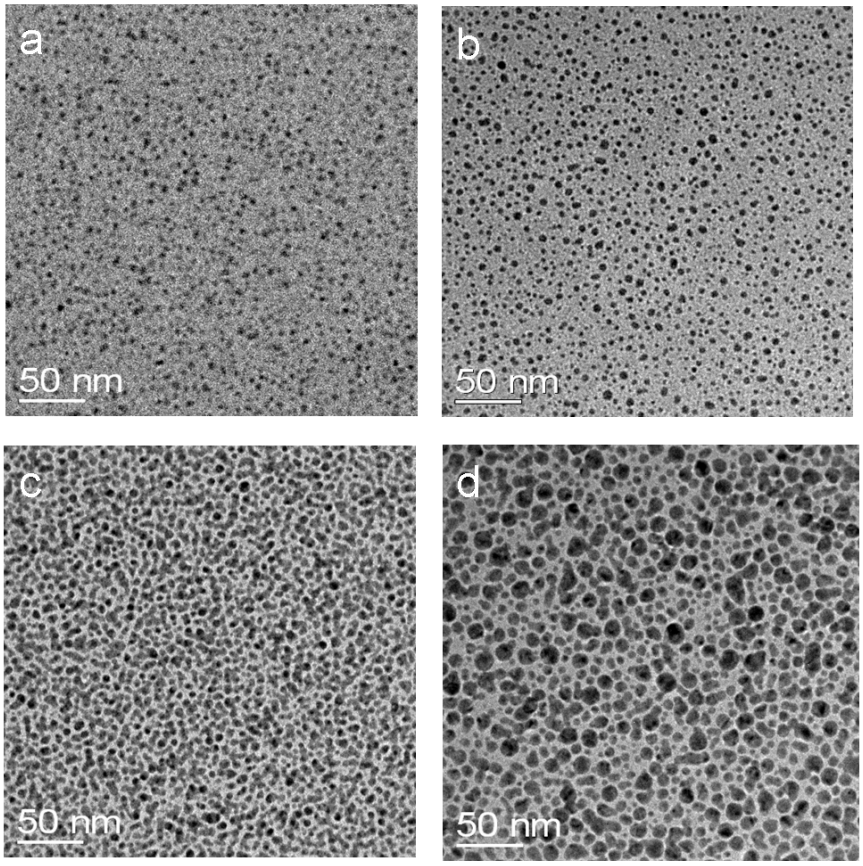

Figure 5.16: *TEM micrographs of a Ag-Au/Teflon nanocomposites. The alloy composition, filling factor, and temperature respectively are (a) 0.40, 10 %, as deposited; (b) 0.40, 10 %, at* $200\,^{\circ}C$*; (c) 0.55, 16 %, as deposited; (d) 0.55, 16 %, at* $200\,^{\circ}C$*.*

The effect of metal diffusion in the polymer due to heat treatment after deposition leads to a change in the microstructure of the nanocomposites. Post deposition annealing of the nanoclusters results in larger cluster sizes with a more spheroidal shape. Moreover, the cluster density, size and shape is dependent on the annealing temperature and time.

Bimetallic nanostructures in polymers synthesized by using co-evaporation from three distinct sources show homogeneously distributed clusters in polymers. The morphology, chemical composition and filling factor of the bimetallic clusters were controlled by the experimental parameters such as the ratio of the deposition rate of metal A to metal B, and metals to polymers.

6 Optical Properties

6.1 Optical Properties of Monometallic Composites

In this section, the optical properties of various polymer composites (Teflon, PAMS, Nylon, and PMMA) containing monometallic clusters of Au or Ag will be discussed. The optical properties of polymers will be explained in relation to the types of metal-polymer combination, filling factor, size of the nanoparticles and interparticle distance.

6.1.1 Results and Discussion

6.1.1.1 Au nanoparticles in various polymer matrices

Figure 6.1(A) and 6.1(B) show the extinction spectra of PAMS and Teflon composites containing Au clusters, respectively. The extinction peaks observed in the spectra are due to the presence of Au nanoparticles in the films. In both polymer composites, the position of the extinction peak wavelength shifted continuously toward longer wavelength with increase of the Au volume fraction. Figure 6.2 shows linear dependence between the peak position and the filling factor. In co-evaporation, the metal volume fraction is strongly related with nanoparticle size and interparticle distance as described in section 5.2.1. The size and size-distribution, interparticle distance and shape of the embedded particles can be varied during film deposition and mainly depend on the amount of the evaporated metal. The role of these factors on the plasmon band width, position, and intensity varies in different ranges of metal filling factor in the dielectric matrix. For very small particles ($< 6\,nm$), a broadening of the absorption peak with decreasing particle size is usually observed but there is no clear explanation for the

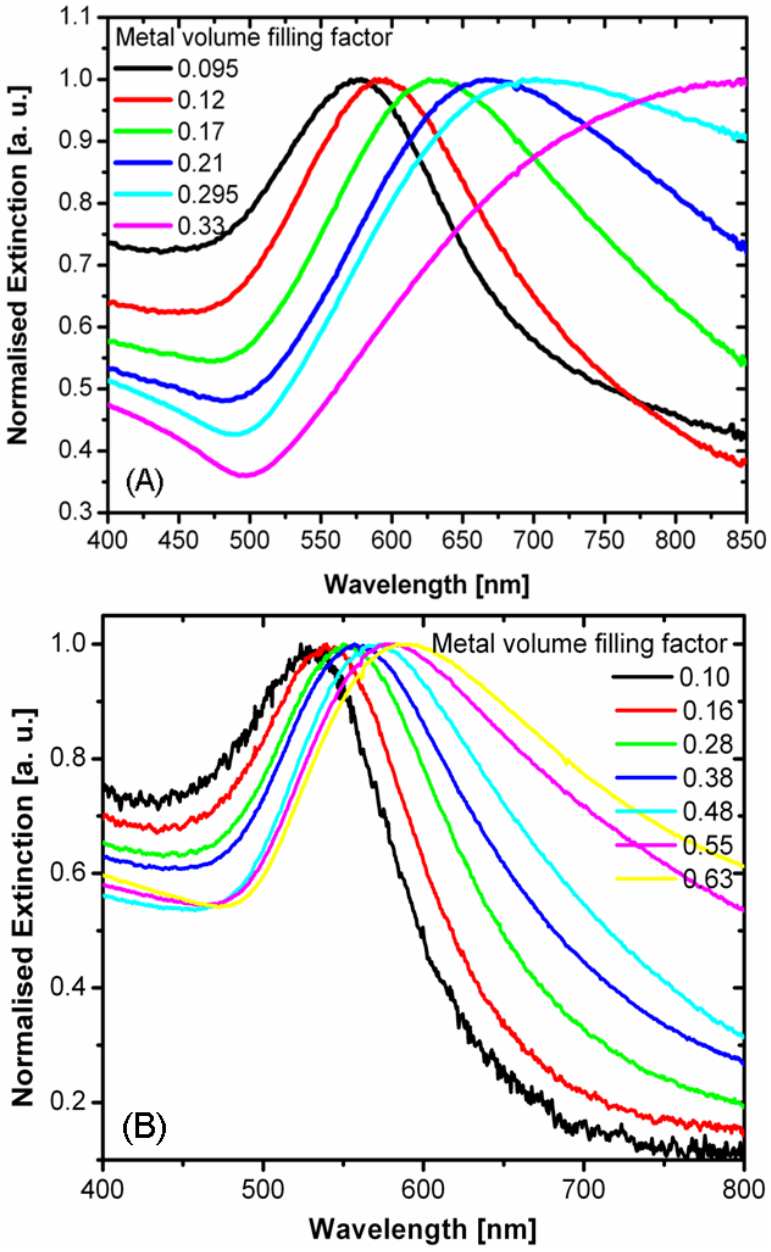

Figure 6.1: *Normalised extinction UV-Vis Spectra of Au-PAMS (A), and Au-TAF (B) at different Au volume fractions.*

peak shift with particle size, especially for small metal particles. On the other hand, a decrease in the interparticle distance lead to increase the particle-particle interaction, which in turn can decrease the effective plasma frequency. There-

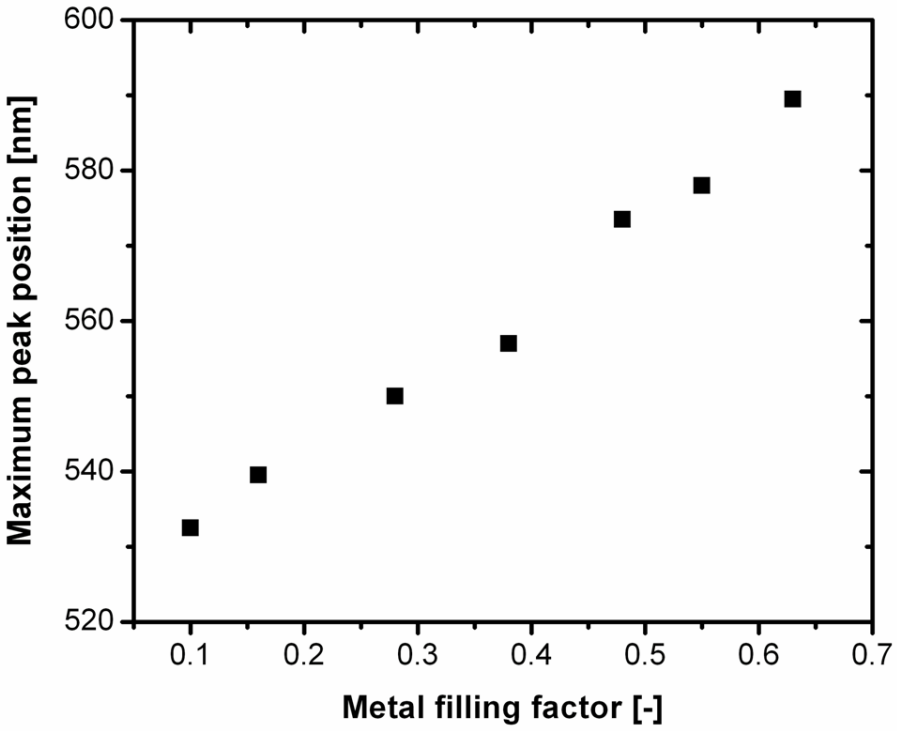

Figure 6.2: *The maximum peak position versus filling factor in Au-TAF nanocomposites*

fore, it is certain that, the shift of the plasmon band maximum toward longer wavelengths in Au-PAMS and Au-Teflon nanocomposites is mainly due to the Au filling factor.

To explain the shift of the plasmon band, either the change in the Drude plasma frequency of the metal particles or the change in the value of the dielectric constant of the matrix has to be considered. The latter can be explained by replacing the matrix with an effective medium where the dielectric constant is expected to increase with the increase of Au concentration. When the metal particles are much smaller than the wavelength of light, the effective relative permittivity ϵ_{eff} of such a composite system can be reduced from equation 2.43 approximately as:

$$\epsilon_{eff} = \epsilon_h \frac{\epsilon_m (1 + 2f) + 2\epsilon_h (1 - f)}{\epsilon_m (1 - f) + \epsilon_h (2 + f)} \tag{6.1}$$

where f is the volume fraction occupied by the metal particles [96–98]. This

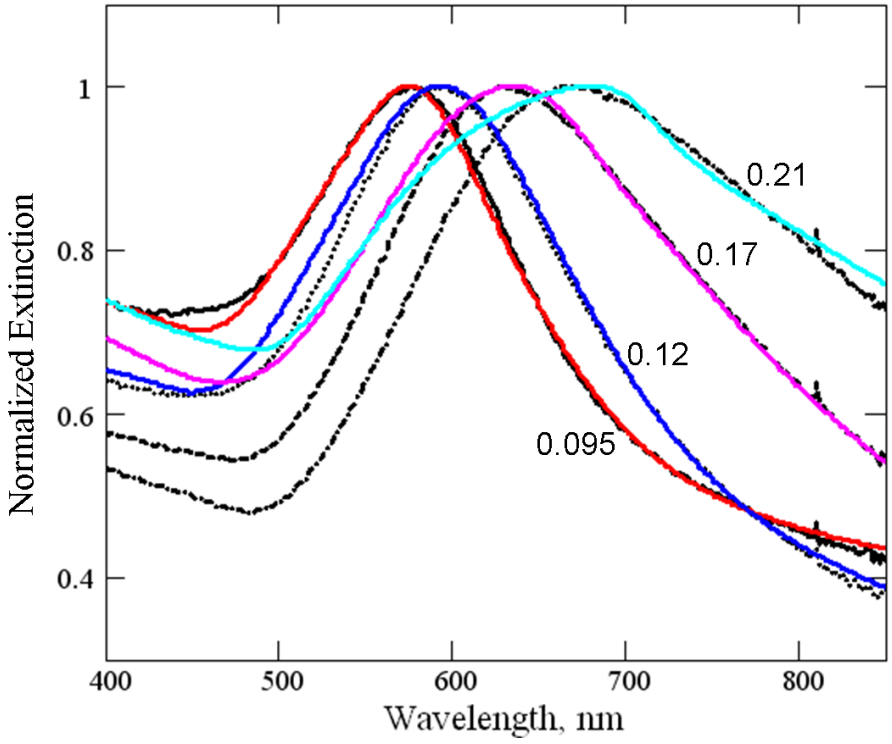

Figure 6.3: *Black curves: Experimental extinction spectra of Au-PAMS nanocomposite films at different metal fillings; Colored curves: numerically calculated extinction spectra by modified effective medium theory*

equation predicts that the band maximum shifts to longer wavelengths with an increase of the metal volume fraction and with the relative permitivity of the surrounding medium [99, 100].

Figure 6.3 shows the comparison between the experimental results in figure 6.1(A) and numerically calculated extinction spectra based on the modified effective medium theory. As mentioned before in section 2.2, the modified EMA fits well with the experimental results up to a metal filling factor below the percolation region. In the range of metal filling factor from 5 to 15 %, the EMA are no longer applicable due to non-negligible contributions of the multipole polarizability and scaling theories are also not yet applicable since the deviation from the percolation conditions is too large. The modified EMA takes a number of assumptions in relation to the metal-polymer nanocomposite material in order to

make the computations simple. For instance,

- the polymer material has an isotropic dielectric permittivity which is independent on the metal filling fraction,
- the dielectric permittivity of metal nanoparticles is isotropic and the dependence of it on nanoparticle size cannot be neglected,
- polymer composites contain randomly distributed metal nanoparticles over some volume but not fractal-like metal structures are formed at least up to a close vicinity of the percolation threshold,
- the shape of the nanoparticles are assumed as spherical in shape at least till close to percolation threshold conditions,
- it is further assumed that all the nanoparticles have the same size, and the interparticle separation distance obeys a Gaussian distribution law,
- most importantly the main assumption in the Bruggeman method (the total polarization of all inclusions embedded in a medium with the effective dielectric constant should vanish) is modified. In the modified EMA, randomly distributed metal particle dimers are also considered in addition to the metal and dielectric inclusions.

The comparison between the experimental and calculated extinction spectra shows a very close fit curve from roughly $500\,nm$ to about $725\,nm$. But a deviation is observed at wavelengths shorter than $500\,nm$.

6.1.1.2 Ag nanoparticles in various polymer matrices

The excitation of surface plasmons of Ag nanoparticles embedded in a Nylon matrix is found to be a transmission minimum or extinction maximum as shown in figure 6.4. At a relatively low metal filling factor $< 20\,\%$, Nylon composites containing Ag nanoparticles show a very small shift of the transmission minima to longer wavelengths. In this region the size of the clusters are very small and

the interaction of nanoparticles is negligible due to the large separation between them. However, further increment in the filling factor leads to an increase of the cluster size beyond $10\,nm$. At the same time, the interparticle distance decreases and becomes comparable with the cluster size. As a result, a large red shift of the plasmon resonance is exhibited due to electrodynamic interactions between the particles at a low particle separation [6, 34, 100]. This phenomenon is more pronounced and shows a large broadening of the plasmon band over a wide range of wavelengths for f above $40\,\%$ because of particle coalescence and the formation of a network structure. For instance, a transmission minimum was observed at $725\,nm$ near the infrared region at $f = 50\,\%$. In this range, the observed optical properties are due to the combined effect of metal filling factor, size, and interparticle separation. As the Ag concentration increases from 4 to $50\,\%$ in the composite films of thickness $60\,nm$, the average size of Ag nanoclusters in the composite also increases from 2 to $20\,nm$.

In order to explain the size dependent plasmonic properties of Ag nanoclusters, one has to consider the different range of metal filling factor at which the size of the clusters vary in the range of $2R < 20\,nm$ or $2R > 20\,nm$. For nanoparticles smaller as or compared to the wavelength of the light the Mie theory reduces to the relation given in equation 2.35. In this relation, the bandwidth and peak height are roughly determined by $\epsilon_2(\omega)$. However, within the dipole approximation there is no size dependence except for varying intensity due to the fact that the volume V depends on the particle radius R. Experimentally, a strong size and size distribution dependence of the plasmon bandwidth and position were exhibited where the dielectric function of the metal nanoparticles itself is assumed to be size dependent $\epsilon = \epsilon(\omega, R)$ [29, 101–105].

In general, the size and size distribution of the clusters are related to the decay processes as indicated in equation 2.40. These decay mechanisms of the coherent motion of the free electrons include both the energy and momentum (dephasing of the collective electron motion) dissipation and are directly related to the width of the plasmon resonance. For a bulk metal with infinite boundaries the damping constant Γ is determined by electron-electron, electron-phonon, and electron-defect scattering processes (grain boundaries, impurities, and dislocations). In this case, the electron-phonon scattering dominates and Γ should be constant. However, for small particles this is assumed not to be valid. The sur-

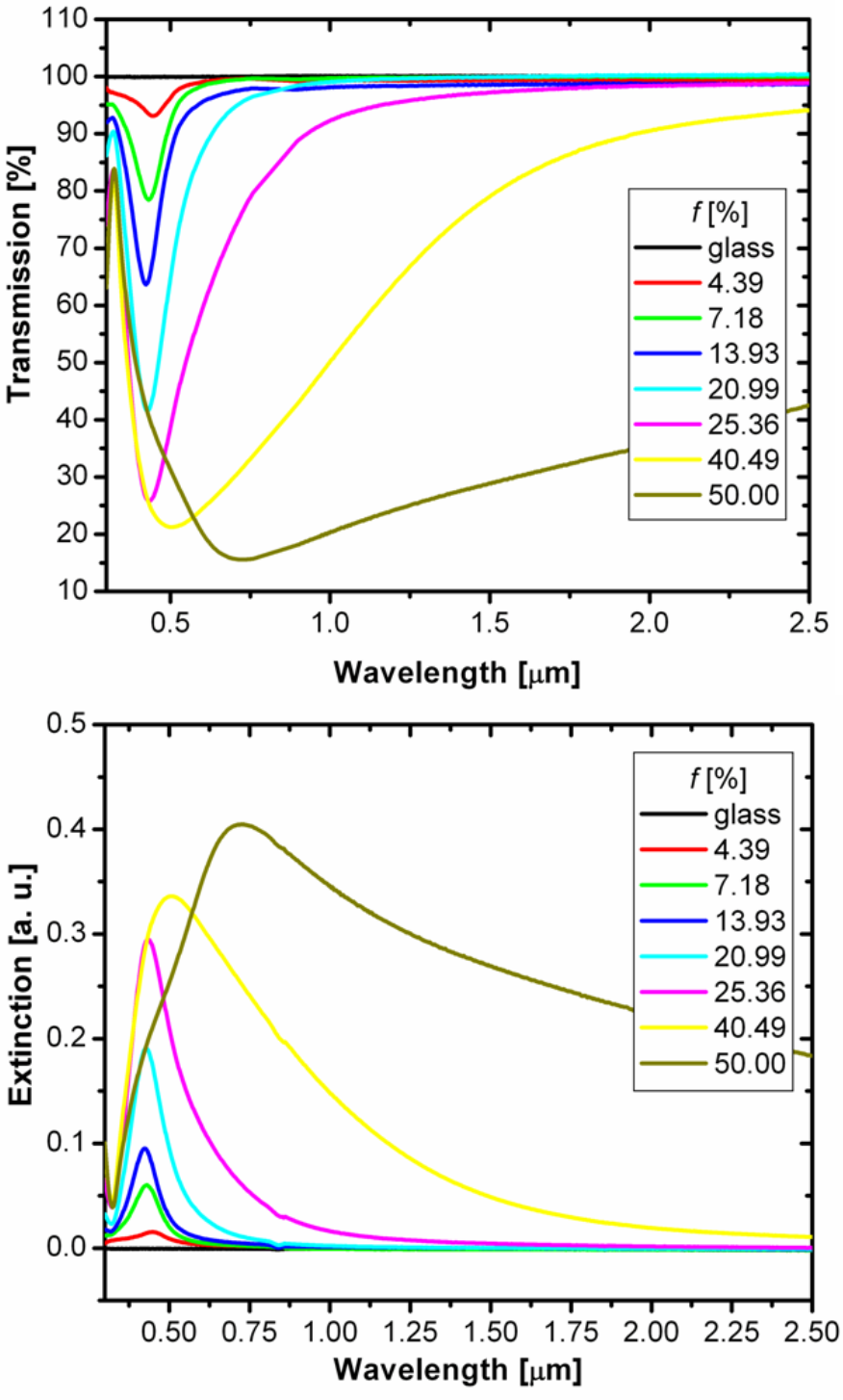

Figure 6.4: *The UV-Vis Spectra of Ag-Nylon nanocomposites at various Ag volume filling factor: Transmission spectra (top), and Extinction spectra (bottom).*

face acts as an additional scatterer because the mean free path of the electrons becomes comparable to the size of the particles.

For $f < 20\,\%$, the size of the clusters is smaller than $10\,nm$, the physical phenomena associate with radiation effects, like scattering and radiation damping, are negligible, such that $\sigma_{ext} = \sigma_{abs}$. Nevertheless, we have to consider that the conduction electrons suffer an additional damping effect due to surface dispersion or finite size. The damping constant is directly related with the mean free path of the conduction electrons. This surface dispersion occurs when the mean free path of the free electrons is comparable or larger than the dimension of the particle, as a result, the electrons are scattered by the surface. As the cluster gets smaller, the surface dispersion effects are more dominant. The surface dispersion does not change the wavelength of the proper modes but it only affects its intensity as shown in figure 6.4.

For $f > 20\,\%$ and if the size of the clusters are large enough, the radiation effect becomes significant. Therefore, the displacment of the electronic cloud is no longer homogenous even for spherical particles, and once more, high multipolar charge distributions are induced. As a result, the depolarization field shifts the position of the plasmon to longer wavelengths and the radiation damping reduces the intensity. In this region, both the absorption and scattering contribute to the extinction spectrum. Figure 6.5 shows the percentage of energy absorbed for Nylon/Ag nanocomposites at various filling factors. The absorbance was calculated by using $T(\lambda) + R(\lambda) + A(\lambda) + S(\lambda) = 1$, where T, R, A and S are transmission, reflection, absorption and scattering, respectively. The large red-shift and broadening of the single plasmon band of isolated clusters can also be due to strong dipole-dipole interactions. When concentrated systems are considered, the nanoparticles become closer to each other, and interactions between neighboring particles can arise, so that the models for isolated particles do not hold any more. If two nanoparticles are in close proximity, the conduction electron oscillation of each nanoparticle is affected by the coupling parter, causing the localized surface plasmon resonance λ_{max} to shift.

In addition, the transmission spectra of Ag nanoclusters dispersed in Teflon and PMMA matrices are presented in figure 6.6 for different metal filling factors. It is known that the optical constants of the particles and the surrounding medium

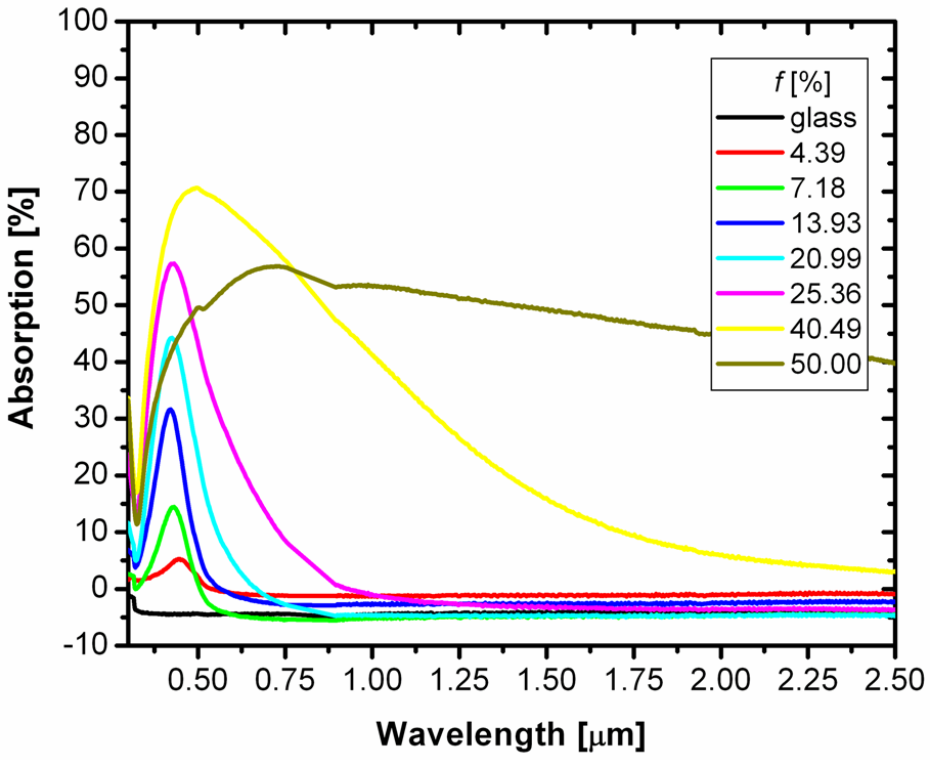

Figure 6.5: *Absorption Spectra of Ag-Nylon nanocomposites at various Ag volume filling factor.*

play a significant role in the peak positions of the transmission minima [106, 107]. Ag particles are also known to show the most pronounced effect due to the size of the particles and the optical constants of the surrounding medium [108]. In this work a comparison among Teflon/Ag, PMMA/Ag, and Nylon/Ag are used to show this phenomenon. Here, the comparison is limited to lower filling factors below 10 %, at which the Ag cluster size and the distance between the clusters are significantly below 8 nm and above 20 nm, respectively. The change in the particle size and separation distance within this range have no significant effect in the redshift of the plasmon resonance for the constant metal concentration in the composites [32]. Thus, the redshift of the transmission minimum from 426 nm (Teflon/Ag) to 432 nm (Nylon/Ag) at the same Ag concentration of 7.18 % is due to an increase of the dielectric constant of the surrounding medium. The average dielectric constants of Teflon AF, PMMA, and Nylon are 1.7, 2.7, and 4.0, respectively [109].

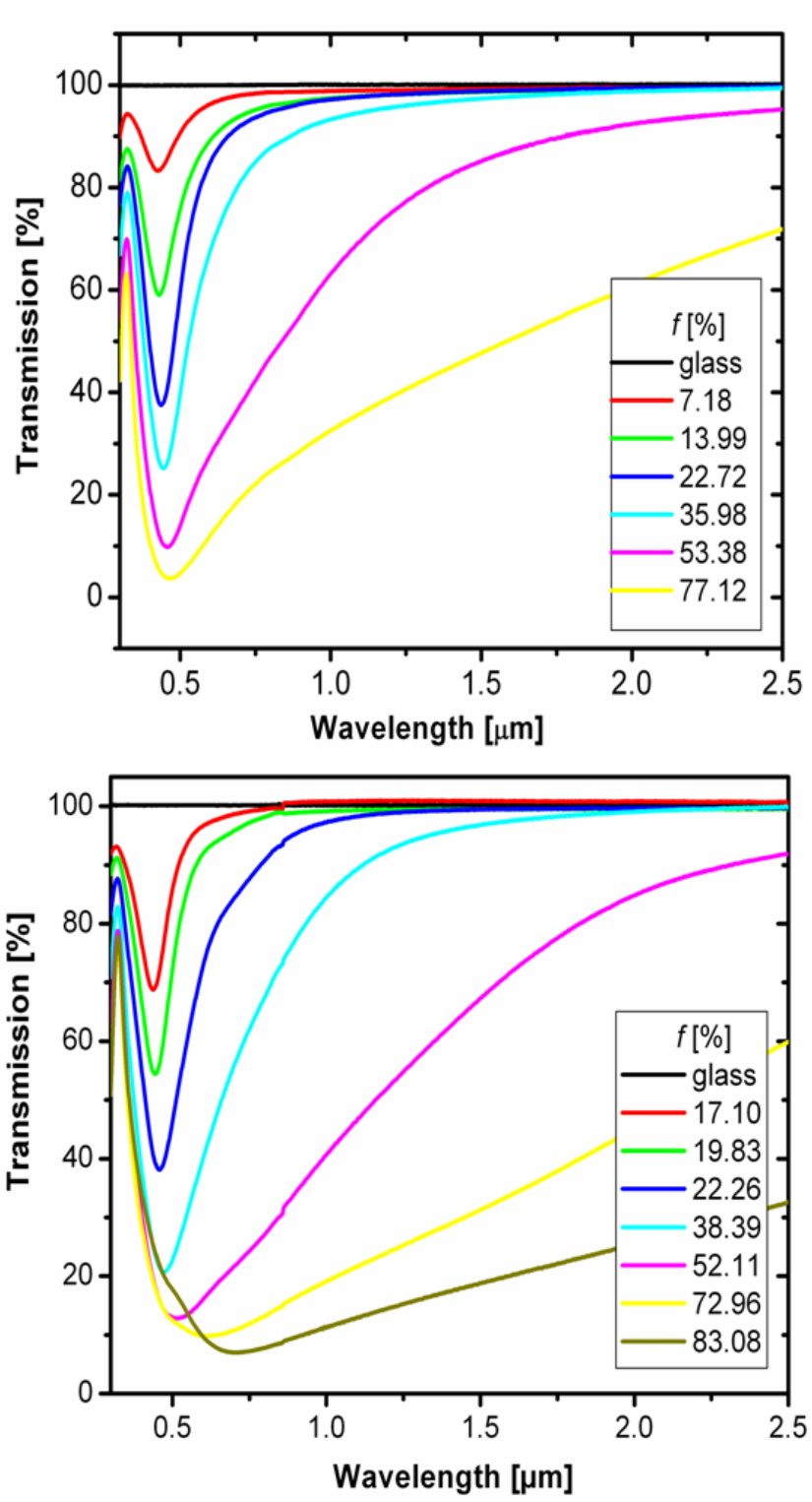

Figure 6.6: *Transmission spectra of Ag nanoparticles dispersed in a matrix of Teflon AF (top) and PMMA (bottom).*

The effect of the surrounding media on the plasmon resonance wavelength of spherical nanoparticles can be easily understood using the Mie theory from equation 2.37. The dielectric constant of the medium surrounding the metallic nanosphere (ϵ_h) is assumed to be a positive, wavelength independent and real number. It is evident that there is a roughly linear relationship between the local index and the plasmon resonance peak of each particle [9, 106, 110–112]. The external nanoparticle environment can be the substrate on which the nanoparticle were fabricated and the surrounding polymer matrix. For instance, nanoparticles can be fabricated on the substrate by metal evaporation where air is the surrounding environment. Changing the substrate may obtain some tunability in the SPR. However, one can tune the SPR significantly by introducing another medium in many ways: (a) overcoating the nanoclusters by tandem evaporation of a dielectric medium such as a polymer, (b) sandwiching the nanoparticles by coating the substrate before metal deposition and then overcoating the clusters, and (c) simultaneous deposition of metal and the dielectric medium. These changes of the surrounding environment induces a change in the average dielectric constant of the medium (ϵ_{eff}) [113, 114].

6.1.2 Conclusion

The simultaneous vapor phase codeposition of Au and Ag with various polymers (TAF, PAMS, Nylon, and PMMA) was successfully used to produce polymer/metal nanocomposites with a wide range of metal volume filling factors. The nanostructure of such nanocomposites is determined by the size, shape, and cluster distribution of the metal nanoparticles. The relationship between nanostructure and optical properties of nanocomposite films is the key to understand how these properties can be controlled by the ratio of metal/polymer rate of deposition. The position, intensity, and broadening of the particle plasmon resonance were determined as function of the metal volume filling factor. At small values of f the spherical metal nanoclusters, which grows in the polymer host during deposition, are uniformly distributed in the polymer and exhibit a strong transmission minimum or absorption maximum in the visible part of the optical spectrum. The position of this metal particle resonance shows a large red shift with increasing f which is accompanied by increasing particle size. These fac-

tors are interdependent for composites produced by vapor phase co-deposition. The present critical comparison between microstructure and the optical behavior elucidates the role of each factor in the observed physical phenomena.

The changes of the optical properties of the nanocomposite films due to a difference in the surrounding dielectric media were reported as well. Shifts of the SP to a longer wavelength region were observed with increasing the dielectric constant of the polymer matrix. These shifts are most clearly exhibited at low metal filling factors where size effects are more quenched.

6.2 Temperature Dependant Optical Properties of Nanocomposites

The plasmon absorption characteristics of the composite films are known to be sensitive to the microstructure of the film , e.g., particle size, shape, particle to particle distance and three-dimensional distribution of the particles in the film. As a result, the tunable SPR wavelength in the visible and near infrared regions has been achieved by changing these parameters of the metallic nanoparticles. In this section, the change in the plasmon absorption as a result of temperature induced changes in the microstructure will be presented extensively.

6.2.1 Results and Discussion

The UV-vis spectroscopy results (Figure 6.7) show the extinction spectra of Au/Teflon(top) and Ag/Teflon(bottom) deposited at various substrate temperatures. The SPR maxima decrease in intensity and shift to a lower wavelength as the substrate temperature increases up to $140\,^{\circ}C$. In contrast, for a temperature above $140\,^{\circ}C$, the peak intensity increases with a red shift of the SPR position. These shift of the extinction spectra of the films are related with the change in microstructure of the nanocomposites obtained as a result of the substrate temperature during deposition. The transition temperature at which the blue shift of the SPR changes to the red shift is similar for both Au and Ag clusters. This indicates that the change is related to the physical properties of the polymer matrix that can alter the condition for the cluster growth. As described in section

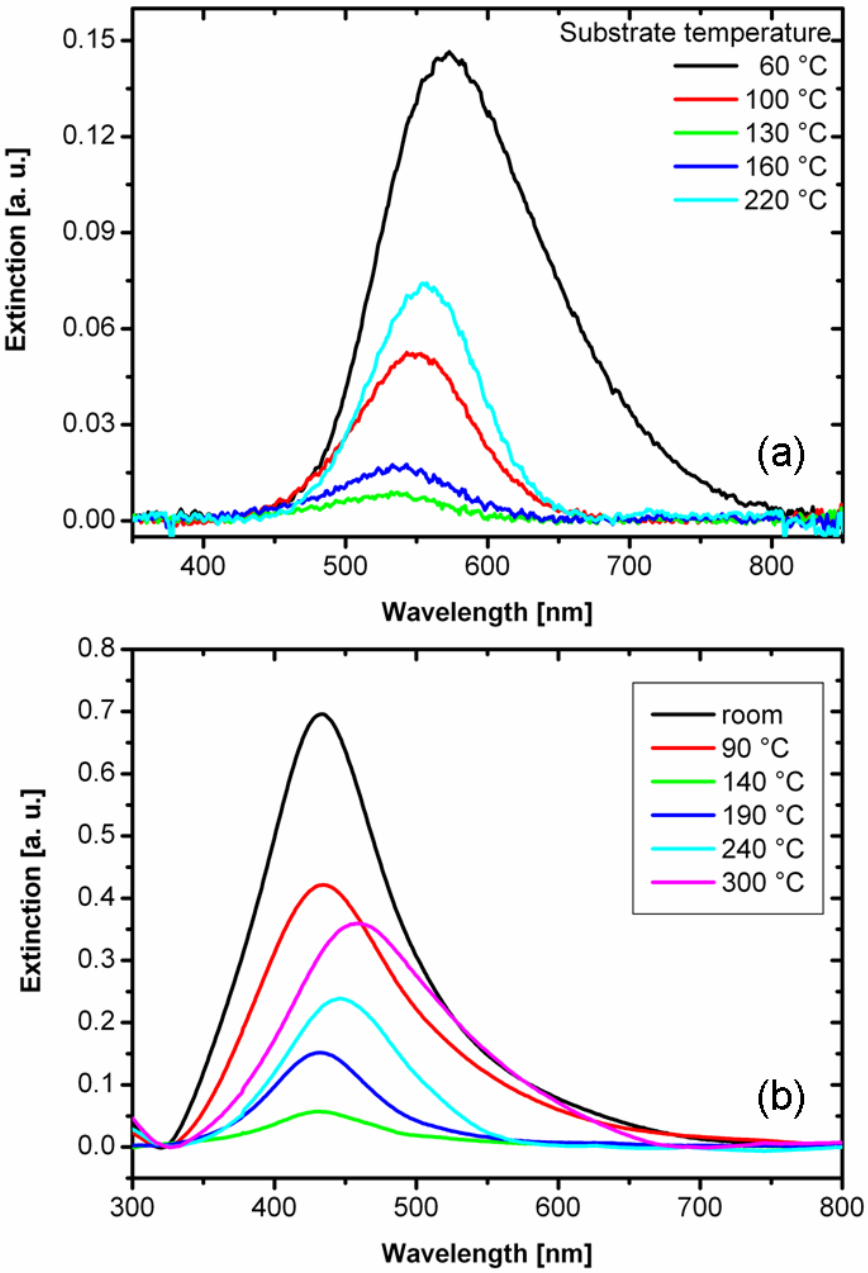

Figure 6.7: *The extinction spectra of Au-Teflon (a), and Ag-Teflon (b) nanocomposites deposited at various substrate temperatures.*

5.2.2, microstrucures with smaller cluster size were obtained with an increase in substrate temperature during deposition up to the glass transition temperature of the polymer. Above T_g, the microstructure of the composites shows larger

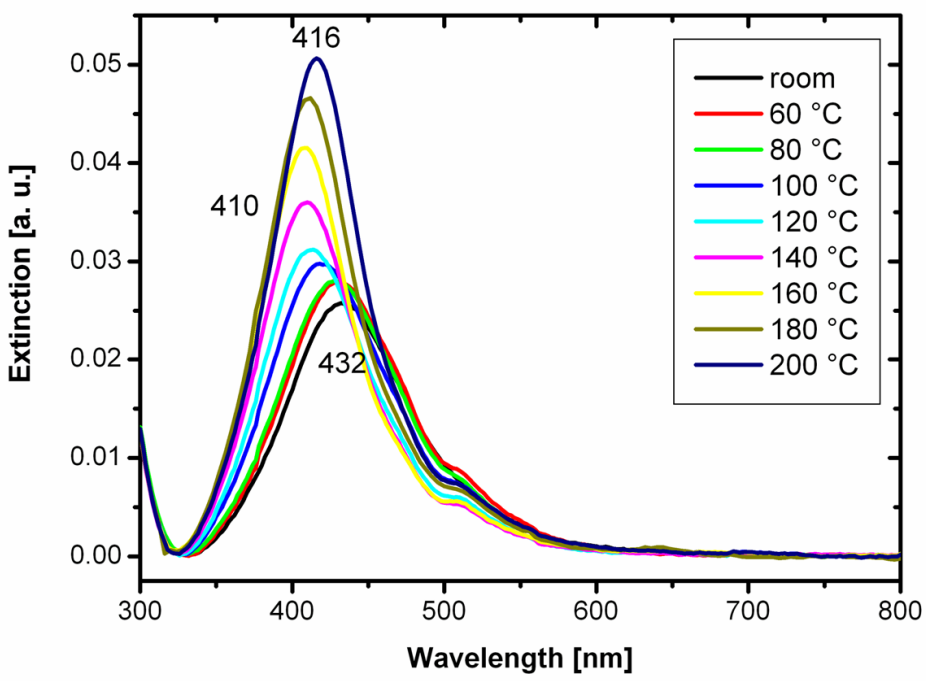

Figure 6.8: *Optical extinction spectra of Ag-Teflon nanocomposites heat-treated at various temperatures for* 10 *min.*

cluster size and a decrease in number density of the clusters.

In addition, we report on the change in the optical absorption caused by postdeposition thermal annealing in air for simultaneously deposited metal-polymer nanocomposites: Ag-Teflon and Au-Teflon. As mentioned before, annealing of such composite thin films result in a heat-induced size evolution of small metallic nanoparticles in the film and/or relaxation of the supporting matrix. This affects the cluster size, interparticle separtation, and spatial distribution, i.e., annealing produces a microstructure with larger cluster size, higher particle-to-particle distance, and lower number density of nanoparticles [115, 116].

The plasmonic properties of polymer nanocomposites consisting of three-dimensionally distributed Ag nanoclusters are strongly dependent on the post-deposition heat treatment as shown in figure 6.8. The heat treatment causes a shift of the plasmon peak to shorter wavelengths, an increase in absorbance, and makes the peak narrow. This result is in good agreement with the change in microstructure, the blue shift of the peak is related to an increase in particle-to-

particle distance as a result of an increase in size of the clusters and a decrease in the number density of the clusters [112, 117–120]. The blue shift in lower content of Ag indicates that the growth of clusters, which is supposed to bring a red shift of the SPR is small enough to dominate the effect of particle distance. However, it leads to a narrow band width with an increase in intensity. It is known that the averaged radius of silver clusters can be related with the extinction spectra using the expression $R = \nu_F/\Delta w$, where ν_F is the Fermi velocity for bulk Ag and Δw is the width in frequency at half maximum of the resonance peak [116].

This phenomenon is completely different from the embedding process observed in metal clusters formed on polymer surfaces during heat treatment [79–81, 121]. In this case, the mean size of the Ag particles is mostly unchanged upon heat treatment and the blue shift of the plasmon peak is considered to be mainly due to the changes in the distribution of the Ag particles in the film. The penetration of the Ag particles with constant particle number leads to a relative decrease of particle concentration per unit volume, since interparticle distance increases as the Ag particles disperse into the matrix. As a result, the local volume fraction of the Ag clusters in the films decreases gradually as the particle disperse into the polymer matrix. This change in the volume fraction of Ag clusters results in the change in the effective dielectric constant of the composite film because the interaction of dipoles induced in the particles by external electromagnetic field of incident light depends on the distance between neighboring particles. This effect can be responsible for the decrease of the plasmon band intensity and width during heat treatment.

A set of samples with lower Ag filling factor far from percolation (a) and near the percolation (b) were heat treated at a temperature of $80\,^{\circ}C$ (figure 6.9), $140\,^{\circ}C$ (figure 6.10), and $200\,^{\circ}C$ (figure 6.11) at various duration of time. In this case, the thermal treatments are commonly used to favor the growth of particles through diffusion. Thus, the growth of particles can be varied by temperature and time of the annealing as well as the the type of microstructure before treatment [122–124]. The comparison among these figures expresses that, the lower filling factor samples exhibited a larger shift towards the shorter wavelength because of the size dependent diffusivity of the Ag clusters. As a result, the particle-to-particle separation can be larger for composites with lower metal content. On the other hand, an increase in the cluster size during the treatment has a less or

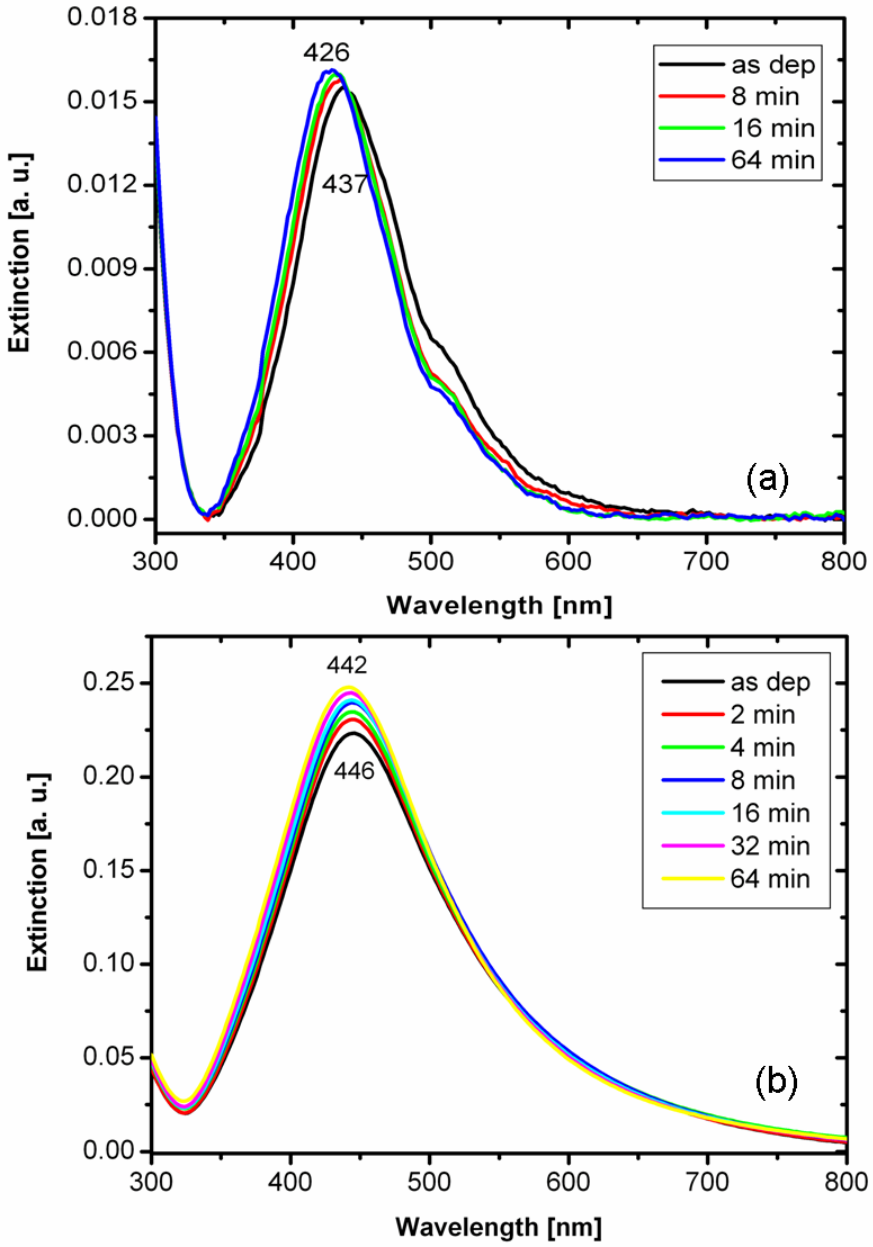

Figure 6.9: *Extinction spectra of Ag-Teflon nanocomposites with various duration of heat treatment at* $80\,°C$*: (a) far from percolation, (b) near the percolation.*

no significant role on the optical properties of the composites. In addition, the time needed to observe size dependent plasmonic properties (red shift) decreases with an increase in the annealing temperature, i.e., $64\,min$, $16\,min$, and $2\,min$ for

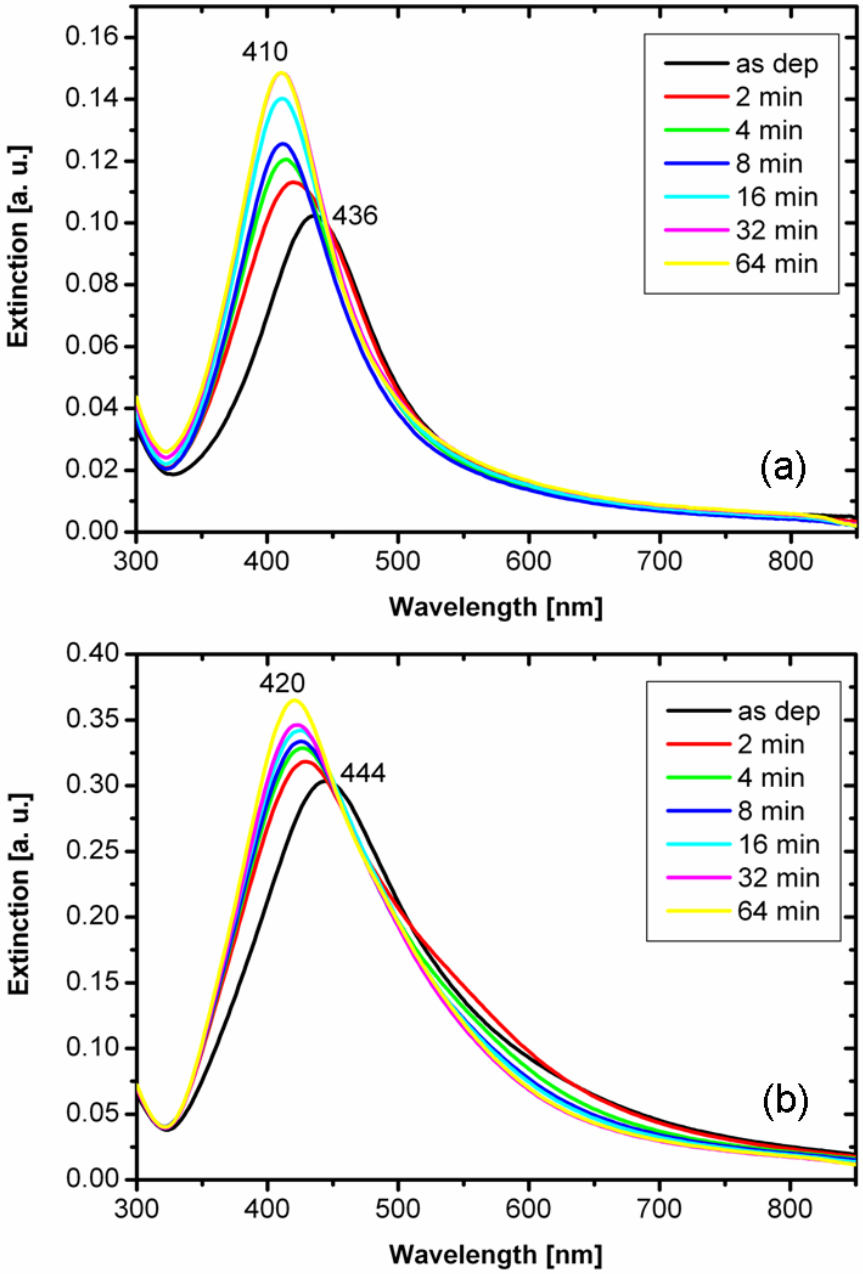

Figure 6.10: *Extinction spectra of Ag-Teflon nanocomposites with various duration of heat treatment at 140 °C: (a) far from percolation, (b) near the percolation.*

80 °C, 140 °C, and 200 °C, respectively. Therefore, the Ag clusters show higher diffusivity at higher temperatures which lead to strong size dependent plasmonic

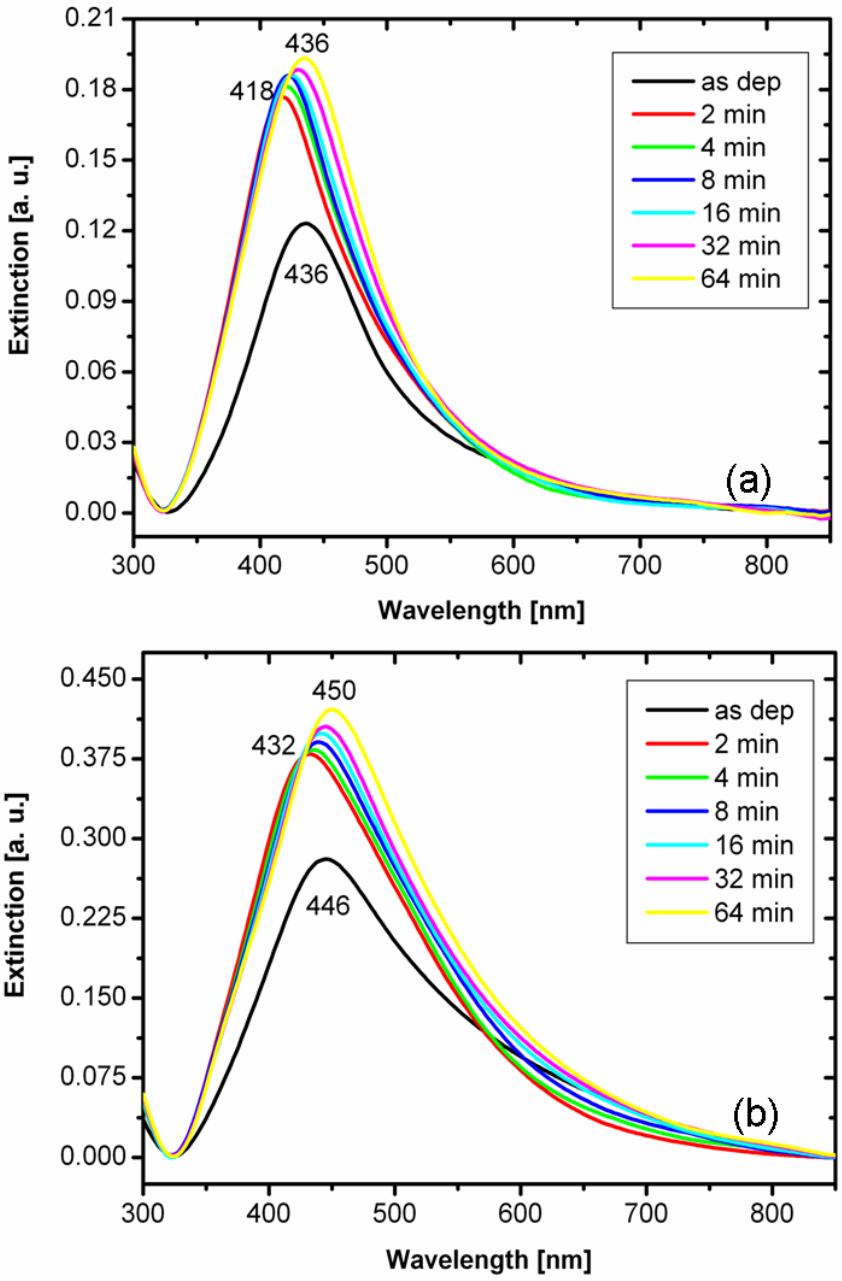

Figure 6.11: *Extinction spectra of Ag-Teflon nanocomposites with various duration of heat treatment at 200 °C: (a) far from percolation, (b) near the percolation.*

properties for higher temperature ranges due to evolution of larger cluster sizes.

Figure 6.12 shows UV-Vis spectra of Au-Teflon composites heat treated at

various temperatures(a) and for different times of treatment(b). As observed in

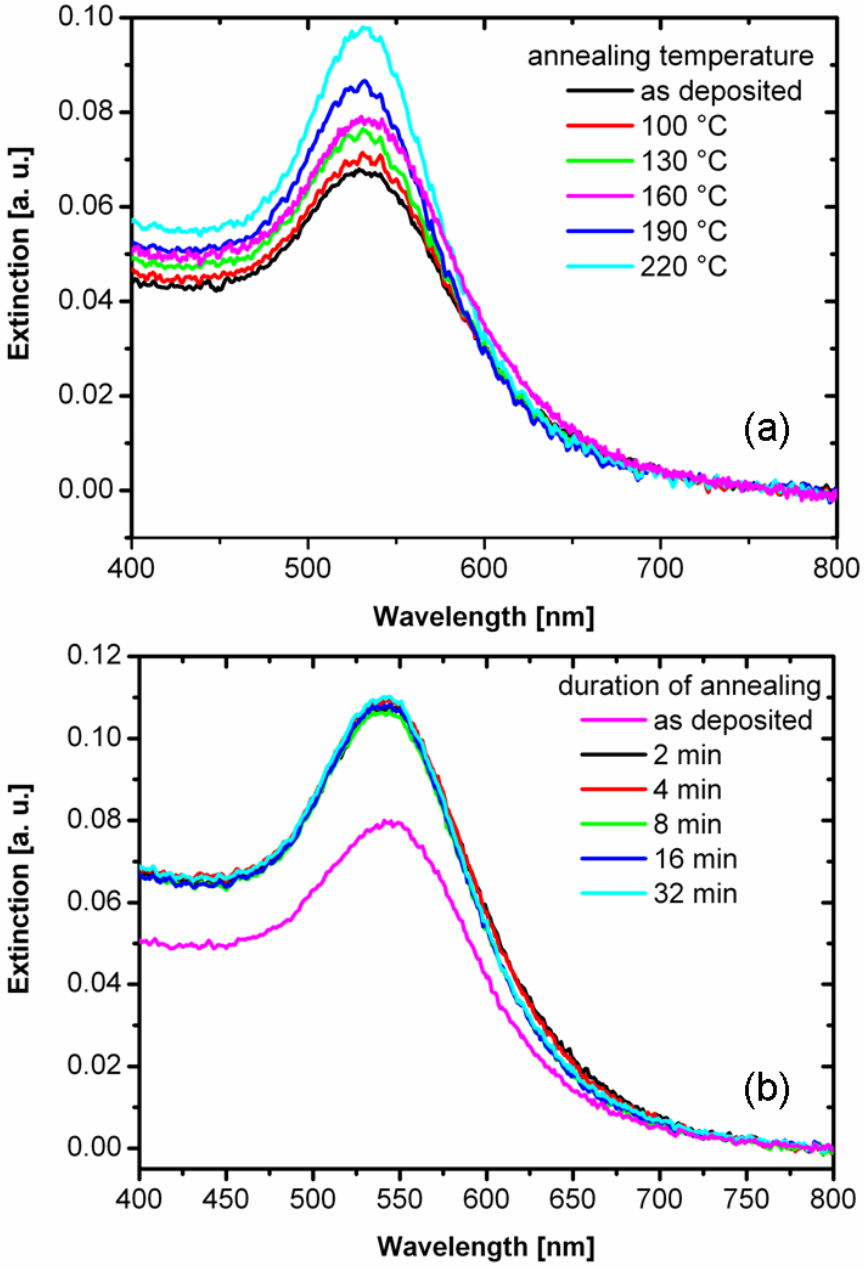

Figure 6.12: *Optical extinction spectra of Au-Teflon nanocomposites heat-treated at various temperatures for 10 min (a), and heat treated for various duration of annealing at* 150 °C *(b).*

case of Ag, the plasmon band intensity increases with an increase in annealing

temperature but with smaller shift in position of the plasmon band maximum to wards lower wavelengths. Whether cluster size is involved or not in these phenomena is very relevant to nanoscale material science. For this study Ag nanoclusters in Teflon are considered as the best candidate since the Ag nanoclusters are known to exhibit relatively strong plasmon absorption in the visible region as compared with Au nanoparticles. Note that, the interband transition of Ag is in the near-ultraviolet region while that of Au is superpositioned at the plasmon frequency of Au particles. Moreover, the larger shift of the plasmon band might be due to the higher mobility of Ag clusters in the polymers as compared to Au clusters. Therefore, the plasmon peak position, intensity and width for Ag nanoparticles can be determined more precisely than the Au nanoparticles. The absence of any change in the intensity of the SPR wavelength of Au/Teflon for heat treatment longer than $2\,min$ implies that the clusters are immobile once they attain the lower surface energy to be in equilibrium state as also observed in [123].

6.2.2 Conclusion

A shift of the plasmon band, originating from the Ag and Au nanoclusters in the Teflon AF matrix, to shorter wavelength was observed with an increase in the substrate temperature up to the T_g of the polymer host. Co-deposition at higher temperature ($T > T_g$) leads to a shift of the plasmon absorption band to longer wavelength. This is due to changes in the number density of the clusters, metal filling factor, intercluster separation and size of the clusters as a result of hot landing of metal atoms and polymer molecules during co-deposition.

It was found that the peak wavelength of the plasmon band shifted towards shorter wavelength with an increase in temperature. This shift of the absorption maximum is caused mainly by an increase in the distance between the clusters due to the decrease in the number density of the clusters during the heat treatment. Changes in the microstructure of the composites as a result of heat treatment take place mainly due to the temperature dependent diffusion of metal clusters in the polymer matrix. These processes are also time dependent. Thus, a plasmon band shift to shorterwavelengthwas observed with longer duration of annealing. But the direction and degree of the shift depends on the original microstructure and

the annealing temperature. A microstructure with a larger cluster size exhibits a smaller blue shift as compared with a microstructure with smaller cluster sizes. Moreover, a high annealing temperature above T_g leads to a red shift of the plasmon peak maximum in contrast to annealing below T_g. Thus, the shifts of the plasmon peak maximum and intensity are controlled by the competition between an increase in cluster to cluster separation and in the size of the clusters.

6.3 Optical Properties of Bimetallic Composites

Bimetallic nanoclusters have been receiving a great research interest because of their properties that are very different from the clusters of their constituents. What makes them very attractive, either as an alloy or core-shell structure, is that their catalytic, electronic, and optical properties can vary dramatically not only due to size effects as pure nanoclusters but also as a result of the combination of different metals [125].

As discussed in previous sections, it is possible to tune the optical properties of metallic clusters by varying the size, metal concentration and the refractive index of the surrounding host. However, these parameters could not be able to induce a large shift of the plasmon band with a minimum broadening of the peak. For pure Au clusters, the surface plasmon band gets broadened and red shifted as the cluster size gets bigger and Ag nanoclusters exhibit much less shift in the position of plasmon band with the change in the size of the clusters.

The motivation to prepare bimetallic clusters consisting of Ag and Au or Ag and Cu rose due to the ability to tune the plasmon resonance for a large range of wavelength within the two boundaries of the constituents as a result of the change in their composition. A linear proportionality between the composition of the alloy and the plasmon peak position in bimetallic clusters was reported before; and the dielectric properties of the bimetallic clusters are assumed to be the composition-weighted average of the dielectric functions characterizing the pure materials [31, 126–128], i.e.

$$\epsilon(x,\omega) = x\epsilon^{Au}(\omega) + (1-x)\epsilon^{Ag}(\omega), \tag{6.2}$$

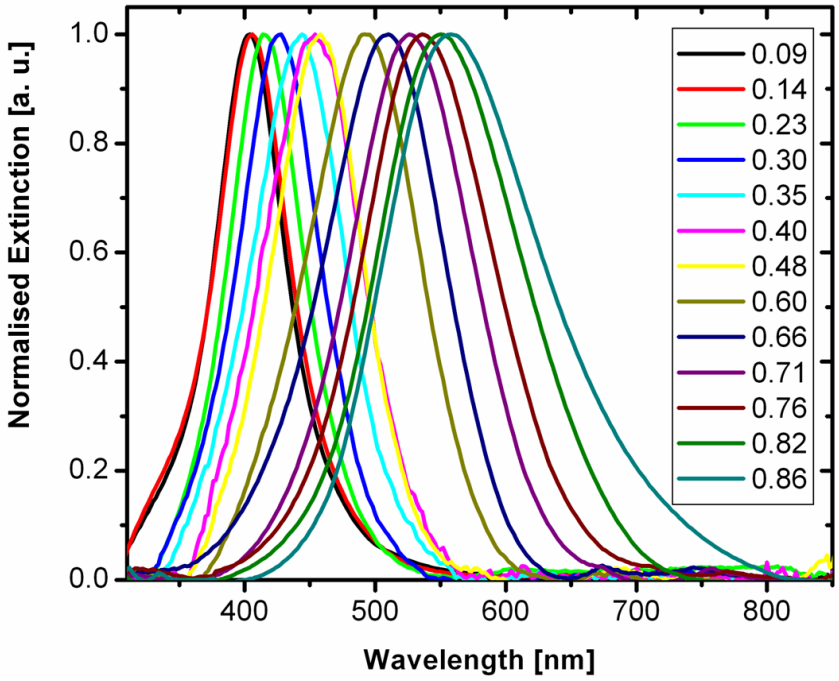

Figure 6.13: *Normalized extinction spectra of Au_xAg_{1-x}/Teflon nanocomposites*

where x is the Au composition in the alloy.

6.3.1 Results and Discussion

6.3.1.1 Bimetallic Ag-Au nanoclusters in polymers

The normalized UV-Vis extinction spectra for Ag-Au (Figure 6.13) shows a single plasmon band which is tuned over a large wavelength window (nearly for 200 nm) through the modification of the composition.

The plasmon maximum was red-shifted almost linearly with increasing the Au content as shown in figure 6.14. The absorption band shift, in this case, is not related to the intraband transition since the plasma frequency of the alloys are similar to that of the parent metals. Nevertheless, the shift must be ascribed to the gradual change in the d-band structure of the alloy with change in chemical

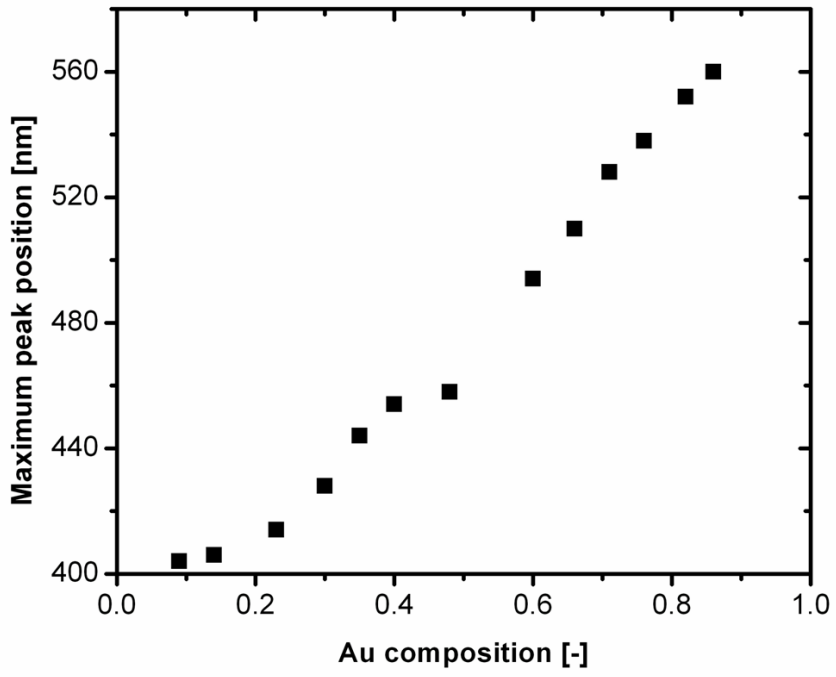

Figure 6.14: *The maximum peak position versus the Au composition in the alloy*

composition, and its effect on that component of the dielectric function.

It is known that Ag and Au have very distinctive and well separated plasmon absorption bands in the visible region which can be easily monitored through UV-visible spectroscopy [129, 130]. When two metals are combined within a single nano sized particle (bimetallic nanoparticles) the optical properties are dictated by a combination of the properties (dielectric function) of both metals. Such a combination strongly depends on the microscopic arrangement of the metals within the particle, i.e. whether an alloy, a perfect core-shell geometry or something between is obtained. For particles composed of Ag and Au the SP extinction spectrum can help in this determination [131]. Combining the resonance condition with the dielectric constant of a free electron gas one finds that the absorption maximum of the plasmon oscillation is roughly given by

$$\omega_{max} = \frac{ne^2}{\epsilon_0 m_{eff}\sqrt{1+\epsilon_m}}. \tag{6.3}$$

The electron density n and effective masses m_{eff} of Ag and Au are, however, very similar. Thus, a surface plasmon absorption at $287\,nm$ and $299\,nm$ is calculated for Ag and Au, respectively, using equation 6.3 [51]. However, the difference in the interband contribution to the plasmon resonance or equivalently the difference in the core polarizability leads to a surface plasmon absorption at $400\,nm$ for Ag and $520\,nm$ for Au nanoparticles. Therefore, the positions of the SP maxima for Ag and Au differ (assuming an equivalent environment) almost entirely because of different contributions of the interband transition to the dielectric functions of the two metals.

In addition to the shift of the plasmon peak position, the damping of the plasmon resonance of Ag-Au alloys with increasing Au content and the damping maximum was observed near $x = 0.4$ (Figure 6.15a). This experimental result is in agreement with calculated spectra of Ag-Au alloy nanoparticles using the full Mie equation [52, 55, 132]. The decrease in the absorbance could be due to the fact that the increased Au content results in the damping of the Ag SP band in this region. As described in section 5.2.3, with an increase in the Au content the mean diameter of bimetallic nanoparticles decreases, which contributes to the damping of the band intensity. On the other hand, the damping can be also the result of more disordered structure that leads to a maximum resistivity where significant scattering of the conduction electrons occur [133, 134]. Therefore, an increase in the intensity of the extinction spectra was observed for $x > 0.4$ in the region where Au is dominant (Figure 6.15b). In this region the shift of the plasmon band towards the higher wavelength is accompanied by an increase in the intensity. This can also caused by an increase in alloy filling factor with composition for $x > 0.5$.

Although the alloy composition is the main focus of this work, the influence of bimetallic alloy filling factor are also investigated.Bimetallic clusters embedded in the polymer matrix show a red shift of the plasmon band maxima with an increase in the alloy filling factor while keeping the alloy composition constant ($x = 0.40$) as shown in figure 6.16.

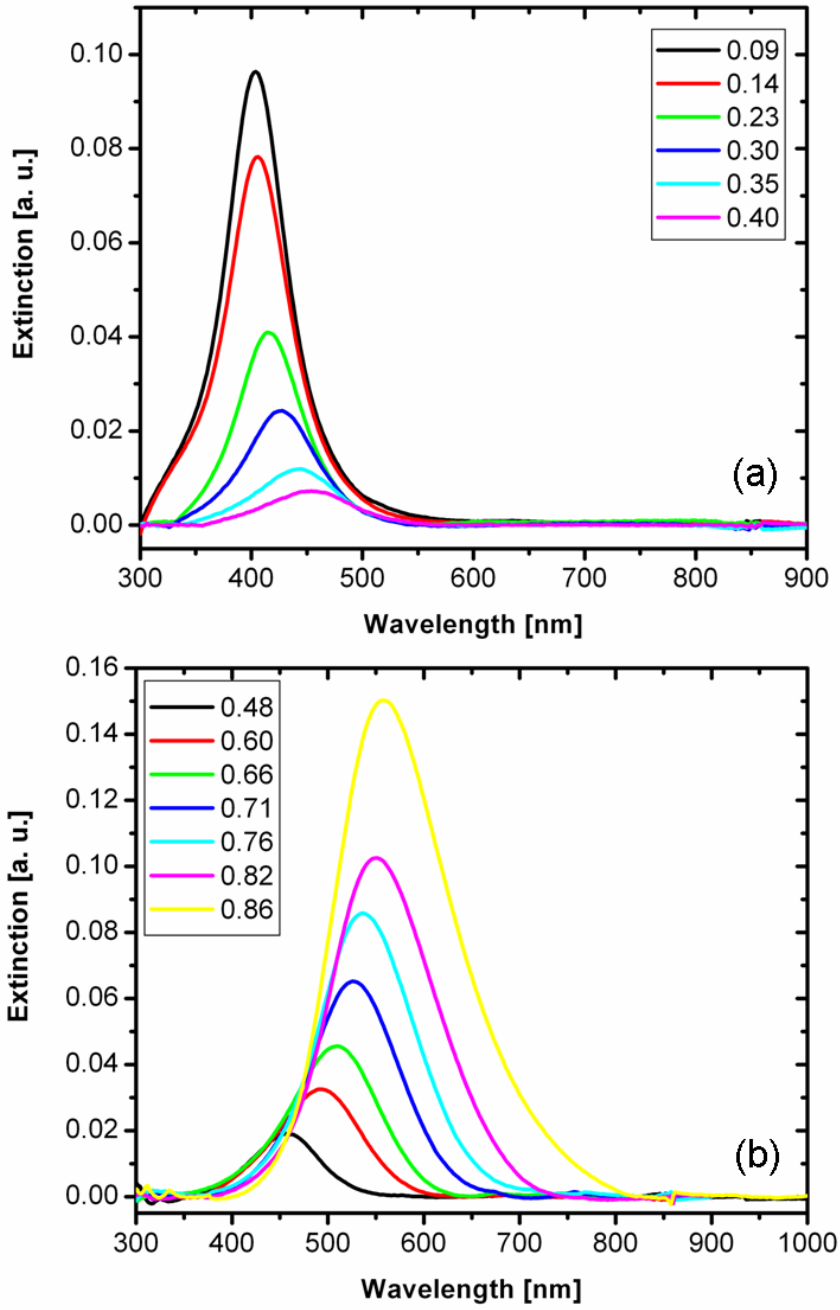

Figure 6.15: *Extinction spectra of Teflon composites containing bimetallic Au_xAg_{1-x} nanoclusters with an increase in Au composition.*

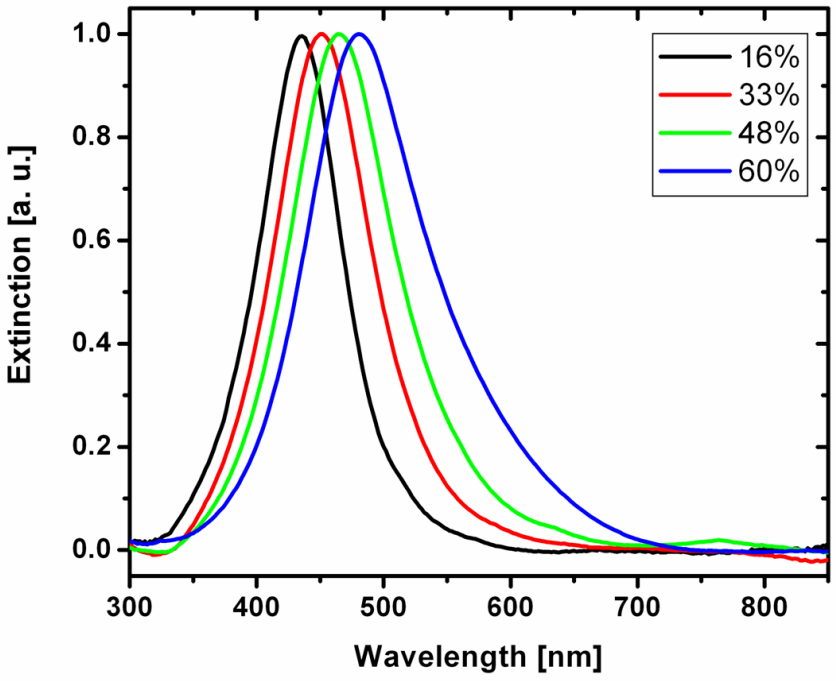

Figure 6.16: *Normalised extinction spectra of Au_xAg_{1-x}/Teflon nanocomposites at various alloy filling factor*

6.3.1.2 Bimetallic Ag-Cu nanoclusters in polymers

The optical spectra of polymer composites containing bimetallic Ag-Cu nanoclusters exhibit a single SPR and the position can be tuned over a wide spectral range as shown in figure 6.17. It is known that the variation in the interband transition among the noble metals results in the plasmon absorption band at about 400 and 580 nm for Ag and Cu, respectively. The original single plasmon peak of Ag-Cu nanoclusters with 0.20 Cu composition and 17 % alloy filling factor shows strong redshift, damping and broadening as the Cu content increases upto 0.4. Further increasing of the Cu content above $x = 0.4$ acompanied with an increase in alloy filling factor up to 50 %. As a result, the plasmon band continues the shift towards the higher wavelength with an increase in their intensity. The wide tuning range in bimetallic Ag-Cu is related to the change in the composition of the bimetallic clusters rather than to the change in their dimensions. Similar nanocomposite films containing either pure Ag or Cu with similar dimensions

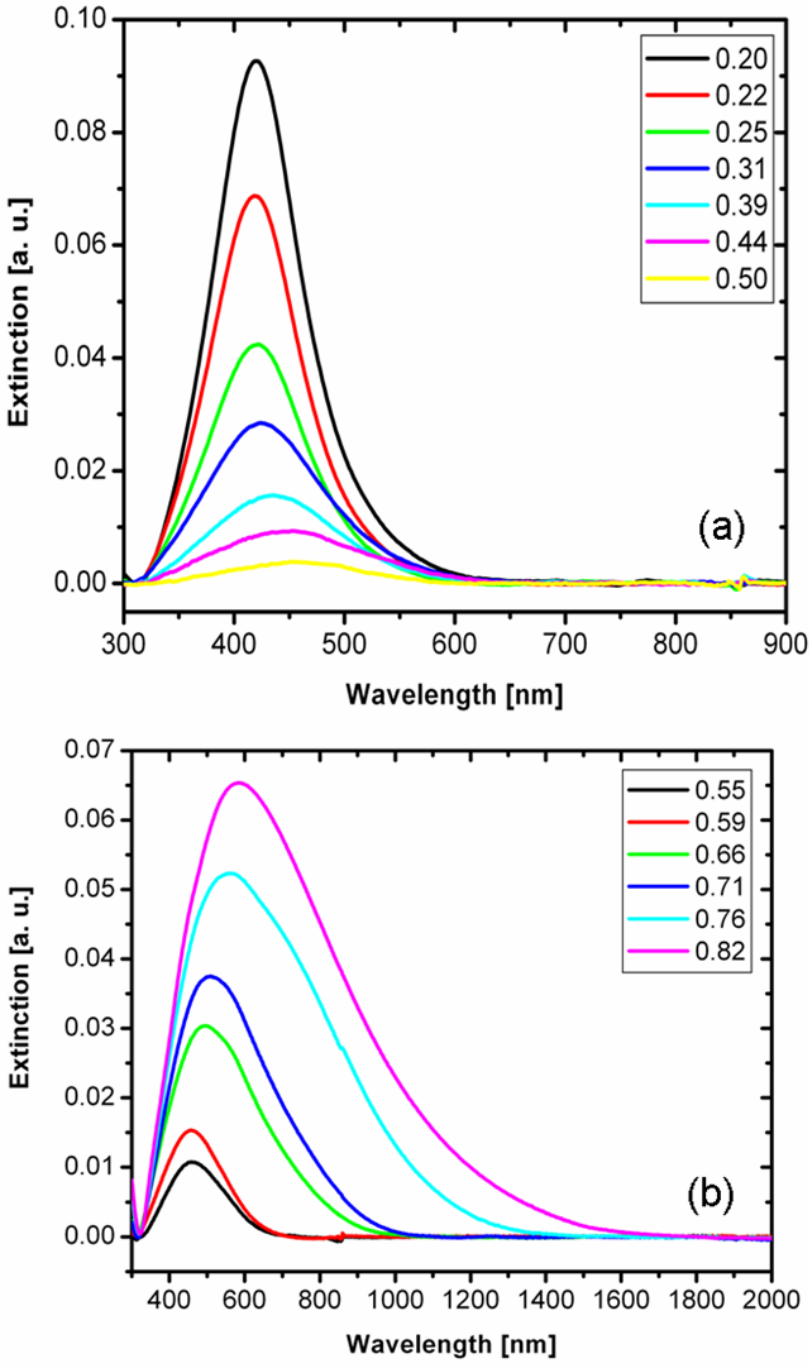

Figure 6.17: *Extinction spectra of Teflon composites containing bimetallic $Ag_{1-x}Cu_x$ nanoclusters with an increase in Cu fraction in the alloy.*

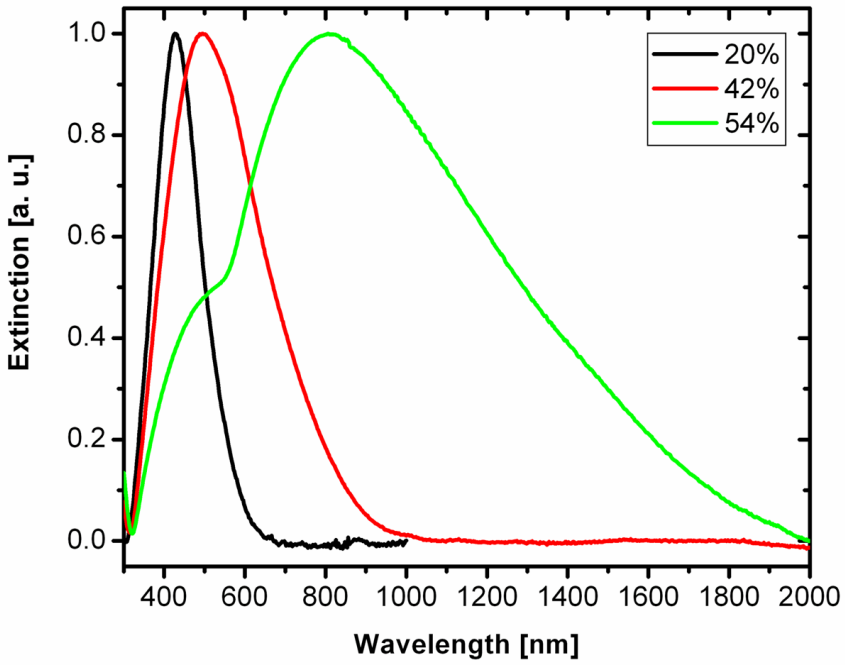

Figure 6.18: *Extinction spectra of $Ag_{1-x}Cu_x$/Teflon composites(x=0.35) as a function of the alloy volume fraction.*

show a spectral tuning range smaller than 50 *nm*.

On the other hand, an increase in the Ag-Cu volume filling factor at a constant Cu composition in a Teflon matrix exhibited the plasmon band to shift to longer wavelengths. However, in contrast with the case of Ag-Au nanoclusters an emerging of the second peak of the plasmon band was observed for $f = 54\,\%$ (see figure 6.18). Earlier reports on the phase separated Ag-Cu and Ag-Au core-shell nanoclusters exhibited two plasmon band peaks [53, 54, 58, 131]. In the case of Ag-Au, the two SPR peaks usually converge into a single one peak when the core-shell structures are converted into alloys by heat treatment.

A critical investigation of Teflon composites containing bimetallic Ag-Cu nanoclusters with $f = 54\,\%$ shows two distinct peaks in the UV-Vis spectra (Figure 6.19). Although the TEM image (figure 5.14C) is not clear to show the core and the shell structure in a definite margin, the optical results reveals the structure. As mentioned before, in the generated core shell structure from simultanious evaporation, the Cu and Ag are expected to be the core and the shell

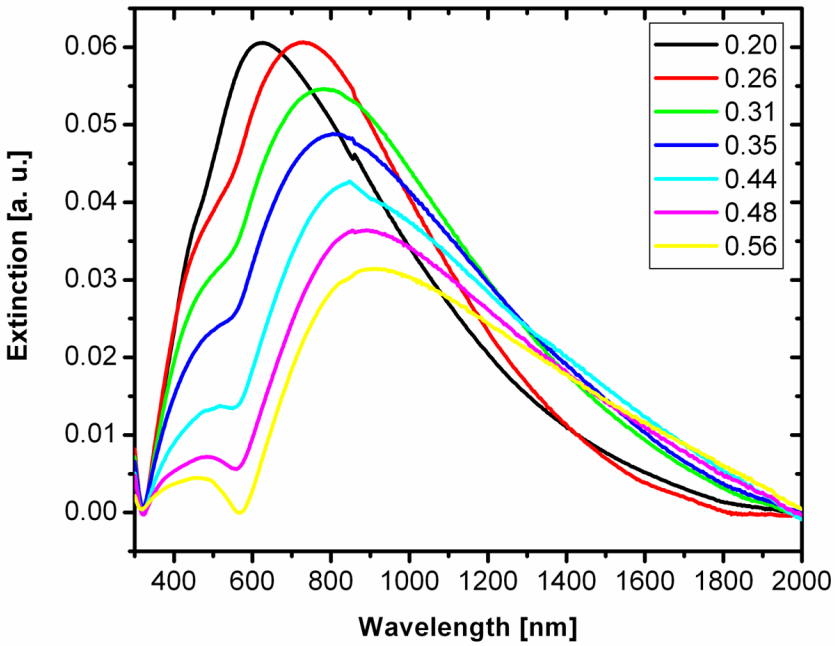

Figure 6.19: *The extinction spectra of $Ag_{1-x}Cu_x$ bimetallic core-shell structure in Teflon matrix with f=54 % alloy volume fraction at various Cu fraction in the alloy*

of the clusters, respectively. Therefore, as the Cu composition x increases the core size increases and the shell thickness decreases. The broadening of the plasmon band extinction spectra and the appearance of the second peak are likely due to the increase in interparticle interactions introduced by the core-shell system. The largest cores (Cu) coated with the thinnest shells (Ag) (for large x) showed the largest frequency shifts of resonance into the near infrared region. According to the Mie theory and experimental results obtained, the extinction spectrum is very sensitive to the thickness and size of the nanoshells [135–139]. Thus, the plasmon band shifts to longer wavelength with an increase in size of the core shell structure and a decrease in the thickness of the shell. Moreover, by increasing the ratio of the core size with respect to the overall diameter of the core shell, the plasmon frequencies can be shifted to the near-infrared region of the optical spectrum. This is as a result of interparticle interactions. On the other way, the blue shift is responsible for the progressive covering of the Cu core particles by Ag shell layers. Due to Ag covering Cu, the plasmon band was Ag dominated.

When the core size is sufficiently large, scattering becomes significant, resulting in the damping of the absorption. This effect promotes a weakening in the apparent intensity of the plasmon band. Note that Cu plasmon band damps out more strongly than Ag. Nevertheless, the absence of the double peak for the smaller cluster size (at lower alloy filling factor) can be due to the size dependent diffusion of the shell element into the core and the formation of bimetallic alloy clusters. The dependence of the diffusion of the clusters on size, in general, [140] and the size dependent diffusion of the shell material into the core, in particular, was reported before [141].

One can assume that the presence of two peaks in Ag-Cu nanoclusters at higher filling factor is due to the change in the shape of the clusters. Both the experimental and theoretical calculations give a single plasmon resonance for spherical particles; and, a deviation from this shape results in two or more SPR which depend on the shape of the clusters (cylinderical-two peaks, cubic-more than three) [142, 143]. If the dimension of the nanoclusters in the transverse axis differs from longitudenal axis (such as prolate, road, oblate in shape), the plasmon resonance splits into two modes: one longitudinal mode along the long axis and a transverse mode perpendicular to the first [144, 145]. The position and intensity of the transverse plasmon band at lower wavelength and the longitudinal plasmon band at longer wavelength depend on the aspect ratio [146–148]. Where the aspect ratio is defined as the ratio of the longer axis to shorter axis diameter of the NCS (aspect ratio=1 for spherical clusters). As the aspect ratio increases, the transverse plasmon band blue shifts and damps in intensity. Whereas, the longitudinal plasmon band exhibits redshift with an increase in intensity [149, 150]. These phenomena are completly opposite to the experimental results obtained for bimetallic Ag-Cu nanoclusters, which reveals the coreshell characteristic.

The temperature dependent plasmonic properties of the composite materials behave differently for the case of AgAu/Teflon and AgCu/Teflon as shown in figure 6.20. The optical characterization reconfirms the difference in the microstructure of these composites. The single plasmonic peak behavior of AgAu/Teflon remains unchanged with a shift in position after subsequent heat treatment at 200 $^{\circ}C$ which indicates the complete miscibility of Ag and Au. The direction and degree of the shift in the SPR depends on the change in interparticle distance

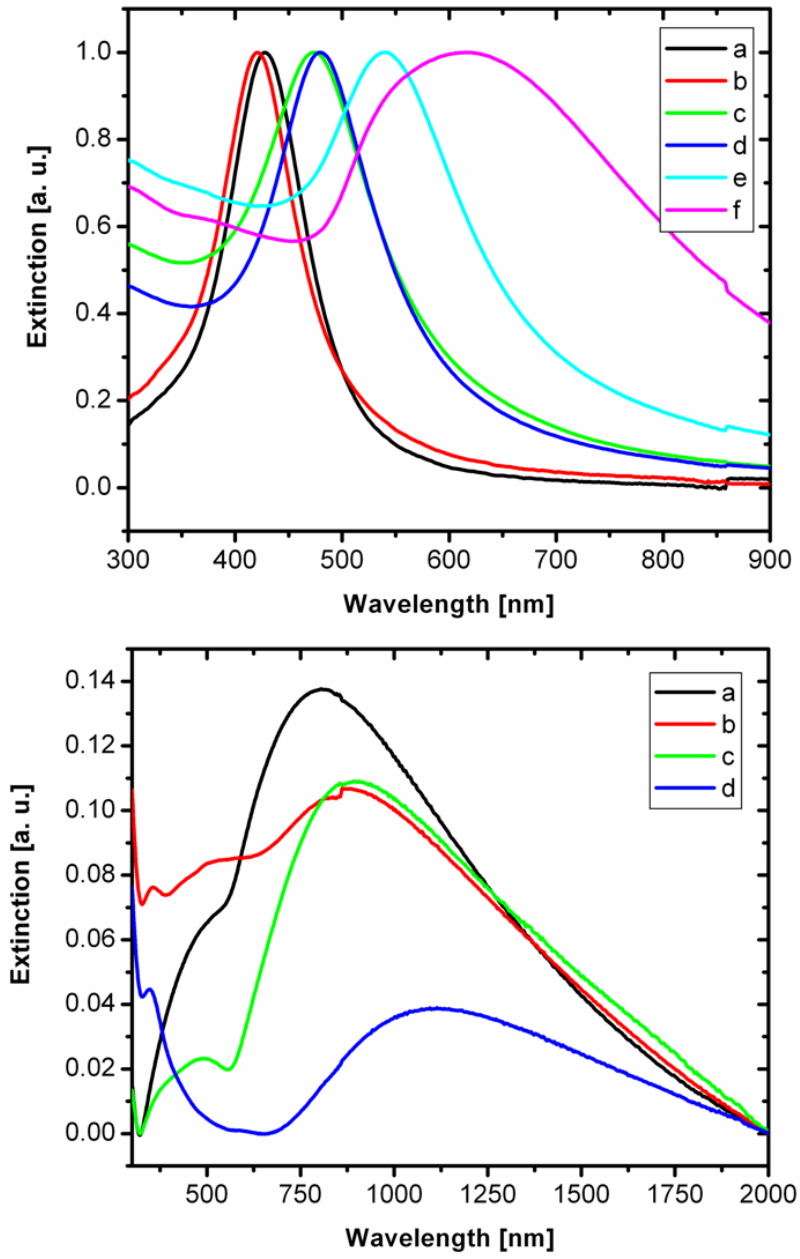

Figure 6.20: *(A) UV-Visible spectra of $Ag_{1-x}Au_x$ alloy nanocomposites. The alloy composition, filling factor, and temperature respectively are (a) 0.16, 10 %, as deposited; (b) 0.16, 10 %, at 200 °C; (c) 0.16, 48 %, as deposited; (d) 0.16, 48 %, at 200 °C; (e) 0.82, 48.5 %, as deposited; (f) 0.82, 48.5 %, at 200 °C. (B) UV-Visible spectra of $Ag_{1-x}Cu_x$ alloy nanocomposites. The alloy composition, filling factor, and temperature respectively are (a) 0.35, 54 %, as deposited; (b) 0.35, 54 %, at 250 °C; (c) 0.48, 54 %, as deposited; (d) 0.48, 54 %, at 250 °C.*

and size as a result of heat treatment. On the other hand, the double peak behavior for AgCu/Teflon remains unchanged and in some cases the generation of a third middle peak is observed. Generally, heating of these composites lead to an increase in the intensity of the Ag peak and a decrease in the Cu peak intensity along with a blue shift and a red shift for Ag and Cu, respectively. The diffusion of Ag into the shell and a consequent better coverage of the core material leads to an increase of the Ag peak intensity and a damping of the influence of the Cu core.

6.3.2 Conclusion

This work reports the synthesis of bimetallic nanoparticles dispersed in a polymer matrix via a co-evaporation approach. In comparison with other techniques this allows to produce high filling bimetallic clusters and free choice of alloy composition. The Ag-Au nanoclusters in a polymer matrix exhibited a single plasmon band for all alloy compositions and filling factors, which is an indication for the formation of a bimetallic alloy NCs. The position of the SP band shifted to red linearly with an increase in the composition. In contrast, the Ag-Cu nanoclusters in a polymer matrix show a single and double plasmon band for $f < 40\,\%$ and $f > 40\,\%$, respectively. Hence, the optical properties of bimetallic Ag-Cu nanoclusters depend strongly on the alloy composition and alloy filling factor. The presence of a double peak at higher filling factor reveals the formation of segregated structure and the immisibility of Ag and Cu in the nanoscale.

Heat treatment of bimetallic clusters (Ag-Au and Ag-Cu) in a Teflon matrix confirmed our earlier assumption of core-shell formation and immiscibility of Ag and Cu in this range. The heat treatment leads to further separation of the two plasmon peaks in Ag-Cu. Whereas, the plasmon peak in Ag-Au alloy nanoparticles remain as single peak during the heat treatment.

7 Electrical Properties

7.1 Introduction

Here, we focus on the electrical properties of nanocomposite films with embedded Ag and Au nanoparticles in different polymer matrices (Nylon 6, and Teflon AF 1600) which are prepared by co-evaporation of metal and polymer under high vacuum. Nanocomposites are formed in between two gold palladium alloy electrodes prepared by sputter deposition on a kapton foil. The gap between the gold palladium electrodes (4.75 $mm \times 3.0\ mm$) is 0.5 mm wide.

7.2 Results and Discussion

7.2.1 Electrical resistivity versus filling factor

Nanocomposites consisting of metallic nanoparticles dispersed in a polymer matrix have electrical conductivity which varies between the conductivity of the insulator material and the bulk metal. The electrical properties of such composite systems depend on both the metal filling factor and the matrix structure [151]. Depending on the film composition, three different conduction regimes are distinguished, namely: the dielectric regime, the transition regime and the metallic regime [152]. In the dielectric regime the small, isolated metal particles are dispersed in a dielectric continuum. However, the metallic regime refers to a structure of granular metal particles that touch and form a metallic continuum with dielectric inclusions. The transition regime is the regime at which the structural inversion between the metallic and the dielectric regime takes place.

Figure 7.1 shows the electrical properties of thin nanocomposite films (70 –

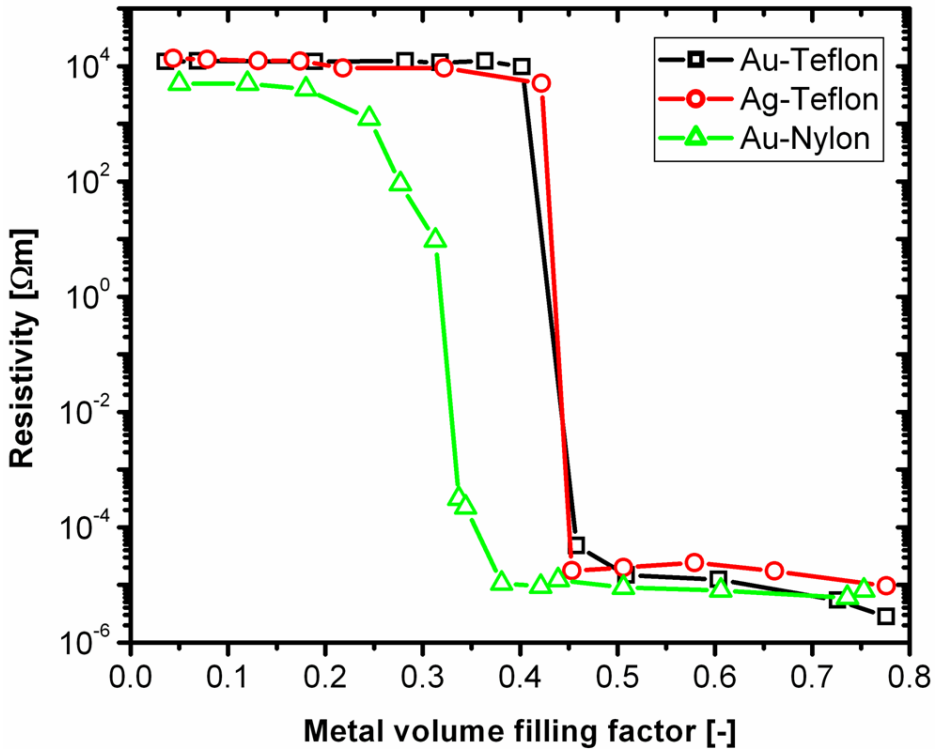

Figure 7.1: *Electrical resistance of Au-Teflon, Ag-Teflon and Au-Nylon nanocomposites with increasing metal filling factor.*

80 nm thick) consisting of Au and Ag nanoparticles in a matrix of Teflon and Nylon as a function of metal filling factor. As expected, the resistivity of the composite materials depend on the metal filling factor (f) and are characterized by a threshold region with a critical value of f, reported as percolation threshold f_c [153–157]. At this metal concentration, the composite undergoes an insulator to metal transition, where the value of electrical resistivity changes by several orders of magnitude from 10^5 Ωm below f_c to below 10^{-5} Ωm beyond f_c. This dramatic change in resistivity of the composites at the percolation threshold is related to the fractal geometry of the infinite metal nanoparticle in the polymer matrix [158, 159]. The lower resistivity value is then caused by the presence of a larger number of metal particles in very close proximity but mediated by thin barriers of dielectric material. As a result, the percolation is not uniquely related to a given chemical composition of the composite material, but it depends mainly on the microstructure of the aggregate and on the ratio between the conductivities

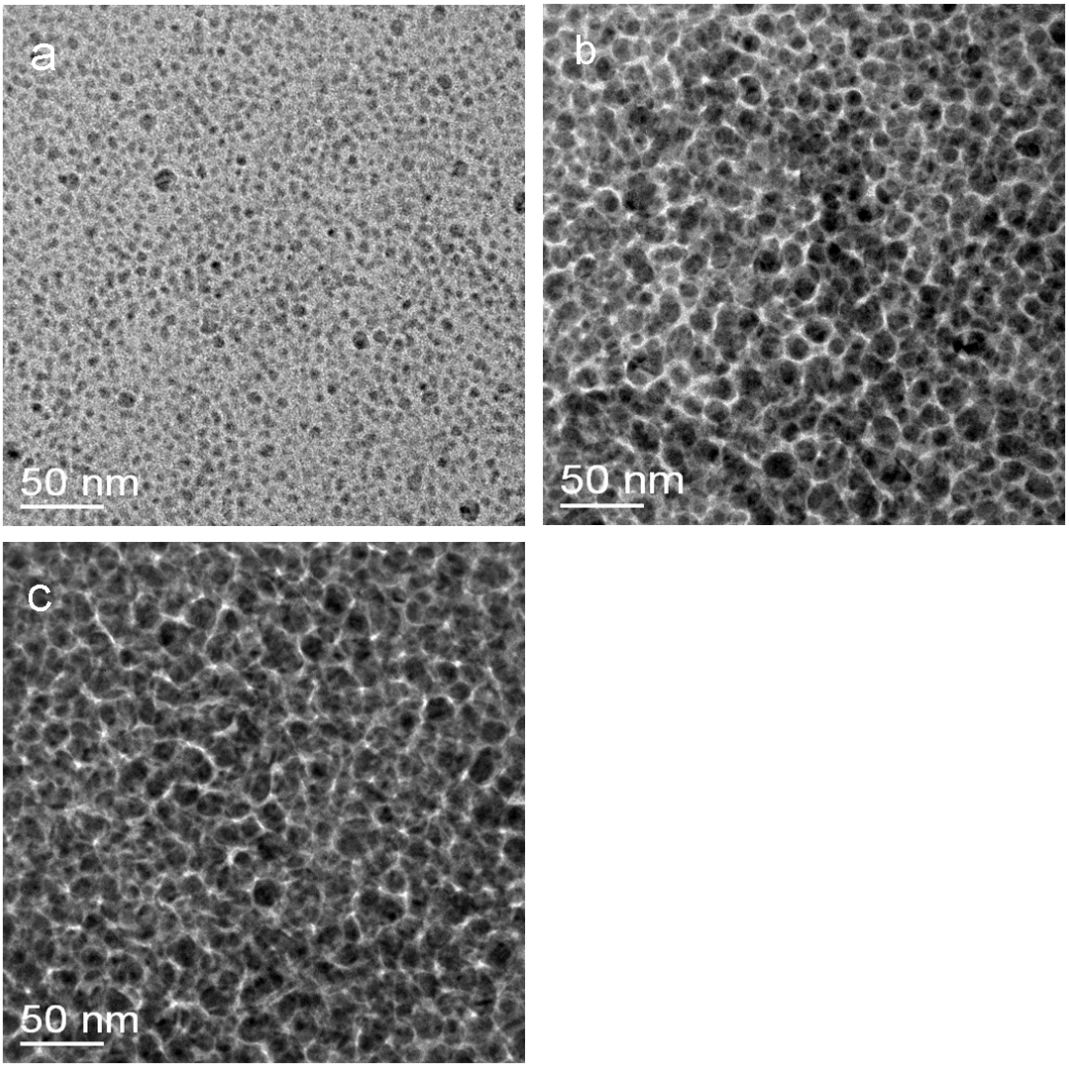

Figure 7.2: *TEM micrograph of Ag-Teflon nanocomposites at the three different regions (a) below percolation $f = 14$ %,(b) at the percolation $f = 42$ %, and (c) above percolation $f = 77$ %.*

of the metallic and insulator phases. For instance, the microstructure of Ag-Teflon nanocomposites at the three different regions are given in figure 7.2.

The comparison between the measured electrical resistivity of Ag-Teflon, Au-Teflon and Au-Nylon reveals the influence of the microstructure on the percolation threshold. It is known that the nucleation and growth of Ag and Au nanoclusters on the Teflon surface are very similar due to similarity in the con-

densation coefficient, which results in nearly similar microstructure. But the Au condensation on two different polymers is quite different. As a result, the region at which the most pronounces resistivity change is centered at about $f \sim 0.42$ for Ag- and Au-Teflon nanocomposites and $f \sim 0.32$ for Au-Nylon nanocomposites. The difference between Teflon and Nylon composites can be related to a difference in size distribution of the nanoparticles.

Assuming a random resistance network model all current has to flow through a single particle at $f = f_c$ by definition, which provides the active connection (backbone) between the electrodes. Thus, an accurate experimental investigation of the d.c. conductivity near the percolation threshold is very difficult due to the significant change in the conductivity of the film with a small change in the nanostructure. It is clear that particle size, shape distribution, and metal particle/insulator interface properties play a significant role close to the percolation threshold. Therefore, the filling factor alone is not sufficient for an adequate characterization of nanocomposites.

7.2.2 Current Voltage Characterization of nanocomposites

Based on their microstructure, the electrical properties of polymer/metal composite films are classified as metallic, dielectric or intermediate. These electrical properties are strongly linked to the particles nanostructure, particularly to the distance between the particles [160]. A variation in size of the nanoparticles $(3 - 15\ nm)$ and inter-particle distance $(2 - 20\,nm)$ can be observed in the dielectric and metallic regime of a nanocomposite with varying metal filling factor. Therefore, when a voltage of $1\,V$ is applied between the electrodes, internal field up to $10^6\,V/cm$ in dielectric regime and $10^7\,V/cm$ in metallic regime can be induced between the metallic particles. Electrical field strengths of such orders of magnitude can provide electrons with sufficiently high energy to escape from the metal by a field emission process.

The electrical transports in nanocomposite films like in granulated metal films involves an activated tunneling between metal particles separated by potential barriers. In this case the activation energy is due to electrostatic image forces, which require the energy δE_F to remove a charge carrier from metallic

particle to a neighboring one [161–163]. It is approximately given by

$$\delta E_F = \left(e^2/\epsilon\epsilon_0\right)\left[(1/r) - (1/s)\right], \tag{7.1}$$

where e is the electronic charge, ϵ and ϵ_0 are the dielectric constants of the matrix and vacuum, r is the particle radius, and s the spacing between the particle centers. However, the conduction can take place via hopping from defect to defect in the insulator as opposed to tunneling directly across the insulating gap between metallic nanoparticles.

Figure 7.3 shows current-voltage plots of Au-Teflon AF nanocomposites with variousAu filling factors. For a composite film with $f = 0.36$, well below the percolation threshold, the metallic particles in the dielectric matrix are separated by a certain distance from each other. As a result, the induced electric field is not sufficient to assist an electron tunneling transport from cluster to cluster, because their distance of separation is too large. Whereas, for composites above the percolation threshold($f > 0.42$), the particles form a metallic continuum with dielectric inclusions. In this case, the interparticle separation is small enough to create a sufficiently high field. Therefore, the field emission is expected to become the dominant mechanism. The conduction by field-induced tunneling thus increases with an increase in the metal filling factor due to a decrease in the separation gap between nanoparticles.

In addition, whether this strong electric field induces a change in the microstructure of the nanocomposites or not requires a special investigation. It would be striking but will be difficult to directly observe the microstructure changes in TEM measurements of samples without and with applied voltages. However, the existence of a breakdown field at a certain applied voltage across the electrodes as shown in figure 7.3 can be taken as evidence for the change in microstructure. We assume that, the strong electric field induces the electron to tunnel from one cluster to another across the polymer matrix and this leads to a higher local current density on increasing the applied voltage. Furthermore, this field might cause the change in the shape of the nanoparticles which leads to further decrease in the gap between them, as illustrated in figure 7.4.

The slight change in the slope of the I-V curve near the breakdown voltage is expected due to the change in the shape of the nanoparticles. of the nanoparticles.

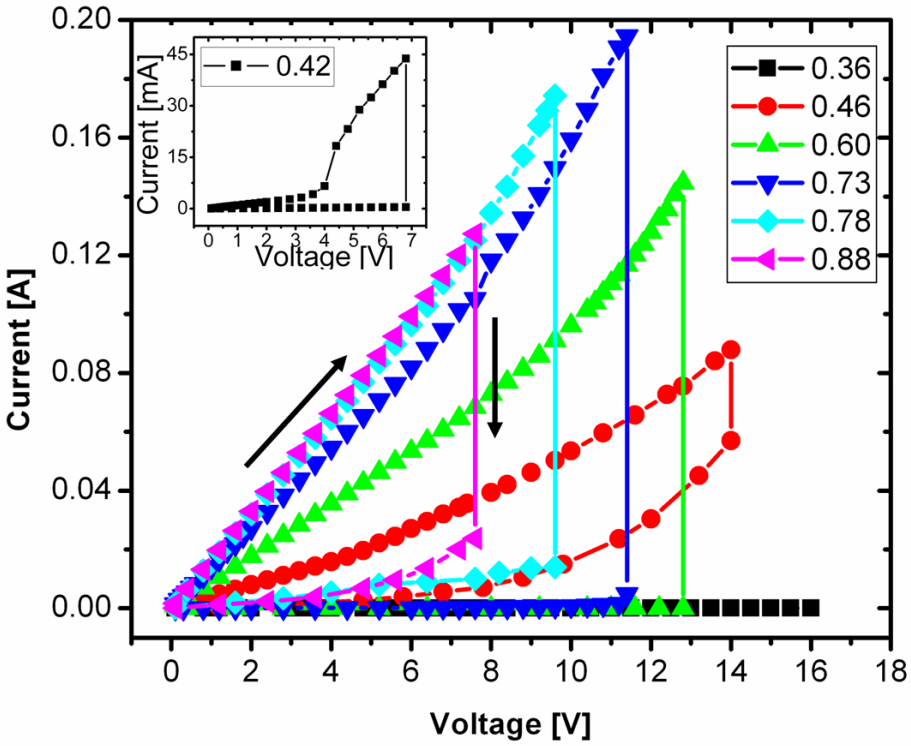

Figure 7.3: *Current-voltage characteristic of TAF composites with embedded Au nanoparticles at various filling factor*

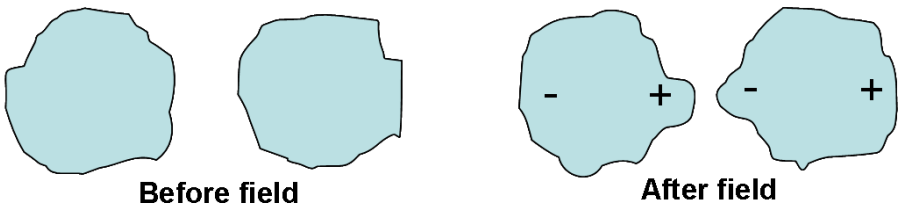

Figure 7.4: *The proposed shape of the clusters before and after the application of voltage across the electrodes*

Later a sudden breakdown of the contacts made by the neighboring nanoparticles is observed probably due to electromigration. The composite film with lower metal filling factor breaks down at higher voltage as shown in the insert of figure 7.5. The first local voltage breakdown event typically happened inside a thin matrix layer separating two nearly touching nanoparticles, where the local electric

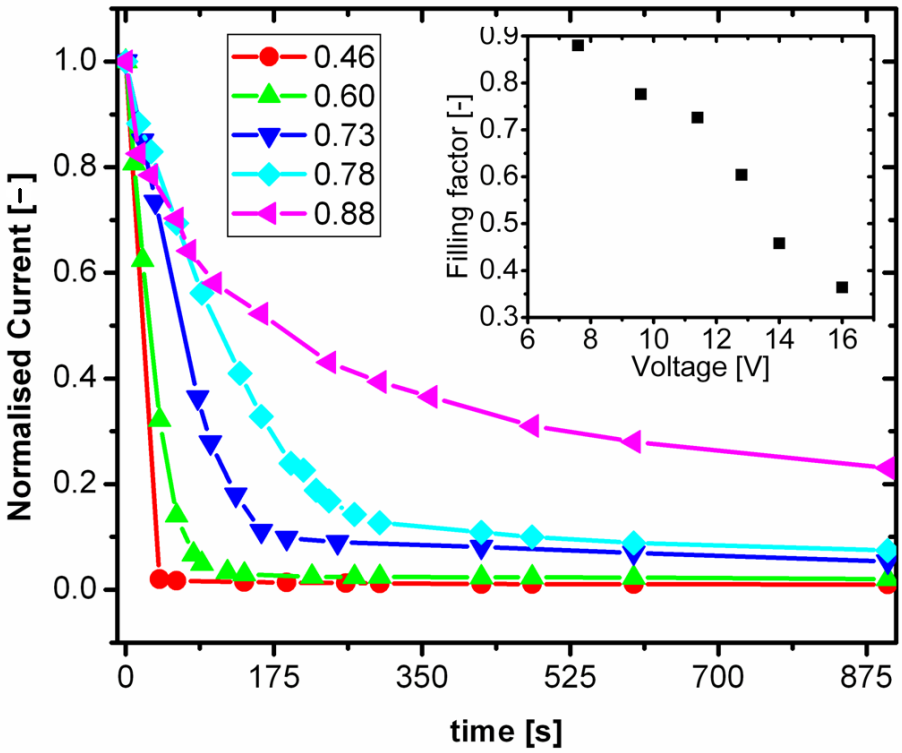

Figure 7.5: *Normalized current versus the switching time at the break down voltage of the corresponding Au filling factor.*

field magnifications were maximal [164]. The sample at the percolation is of special interest (see insert figure 7.3) because of the nonlinear behavior. In this case, the particles from a contact network (or percolation path) which is very sensitive to a variation in the applied dc voltage near $4\,V$ causing a large change in the film conductivity and break down field at lower voltage.

In figure 7.5, the normalized current at the break down voltage is given as a function of time to reach a stable and a low current state. The sample with the lower filling factor reaches the low current state very rapidly ($40\ s$ for $f = 0.36$) as compared to the high filling factor sample ($900\ s$ for $f = 0.88$). This delay time is probably related to the shrinking of the nanoparticle bridges with different size due to high local current density. The bridges at higher f are thicker so that it takes a longer period until break down as a result of the electromigration.

Moreover, it should be asked to what extent the I-V curve retains its shape

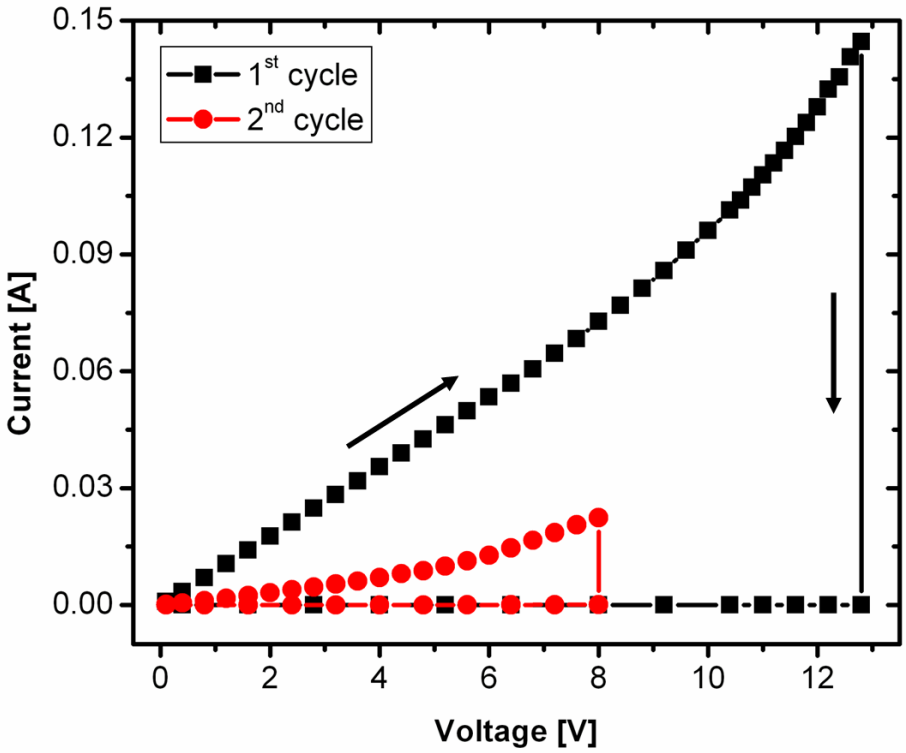

Figure 7.6: *Current-voltage characteristics for two different cycles of Au-TAF nanocomposites with* 0.60 *metal filling factor.*

in different cycles. In principle, nanostructural changes are assumed to be irreversible and cannot explain the reproducibility of switching behavior. Since charge transport takes place through only a smaller number of particles which comprise the backbone, high local current densities are possible. This causes to change the interparticle distance due to local heating and electric field. In figure 7.6, a large variation between the first and second cycle is observed for composites with $f = 0.6$ which reveals the irreversible change in the microstructure. The conductivity of the sample in the second cycle is smaller than the first cycle due to the larger separation gap between the clusters after the first break down. One can also explain these phenomenon in terms of the number of pathways. The number of pathways for electron flow during the first cycle is reduced in number after the break down in the first cycle which causes the second cycle to break down at lower voltage.

7.2.3 Temperature dependence of the electric properties

In this study, the Au-Nylon composites with various Au concentration were heat treated. The annealing temperature was determined by an iron-constantan thermocouple fixed beneath the sample. The electrical currents at the applied voltage of 0.6 V were measured during the increase of the sample temperature and from their derivation the resistances were calculated.

The electrical resistance as a function of annealing temperature is shown in figure 7.7 for samples below and above the percolation threshold. The shape of the curves in both figures is not similar, which refers that their electrical conductivity mechanism in this two different ranges are quite different from one another.

All the samples with metal concentration below the percolation threshold exhibited a similar character: the resistance remains nearly constant or slightly decrease up to about 90 $°C$, then an increase in the resistance was observed upon heating. The maximum peak in the resistance is exhibited at a certain critical temperature between 120 $°C$ and 145 $°C$ which shifts to higher temperature with an increase in the filling factor. After this critical temperature the resistance of the film drops to lower value and shows a minimum resistance at 161 $°C$ independent of the metal filling factor. Further heat treatment up to 185 $°C$ leads again to an increase in the resistance of the sample. Whereas, for samples above the percolation threshold: the resistance is nearly constant up to about 100 $°C$ and drops afterward up on heating. The large drop in the resistance was observed at a temperature between 100 $°C$ and 140 $°C$ which varies according to their metal filling factor. All samples exhibited the same character during the cooling down process, the electrical resistance slightly decreases with the decrease in the temperature.

One possible explanation for the samples below percolation threshold could be the following: in the low-field regime for samples below the percolation threshold, the voltage difference between neighboring metal grains ΔV is much smaller than kT/e. As a metallic pathway does not exist between electric contacts in these samples the charge transport is due to electron hopping between nanoparticles. Therefore, thermal activation tunneling is either almost negligible or compensated by electron phonon scattering in the metal clusters and can be the

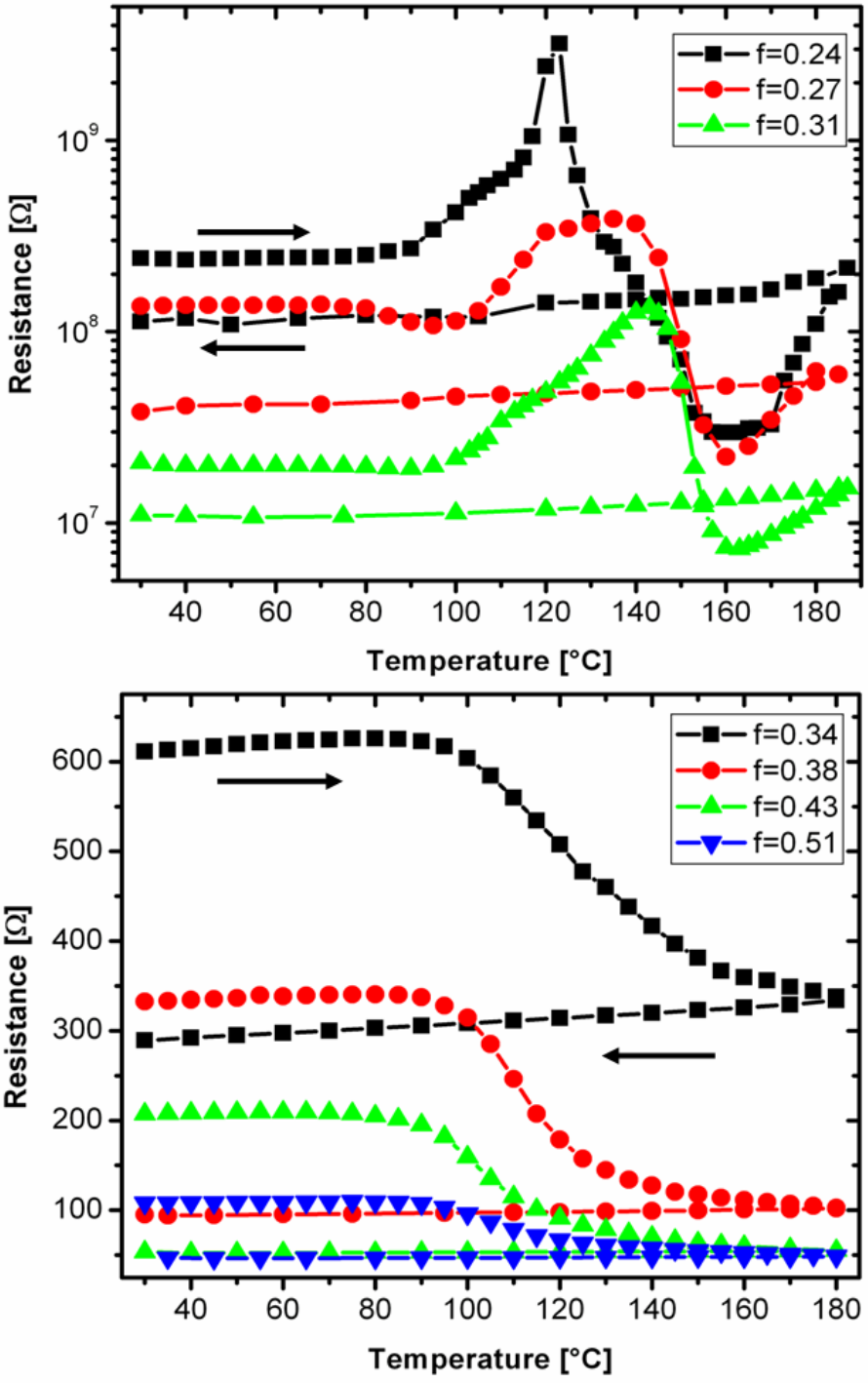

Figure 7.7: *Resistance of Au-Nylon composites as a function of annealing temperature for filling factor below the percolation (top) and above the percolation (bottom).*

cause for the slight decrease up to $90\,°C$. Heating above this temperature, which is near the glass transition temperature of the polymer, allows a metal cluster coarsening. This might happen in the second part of the temperature range up to the critical temperature, and results in a lower number of nanoparticles with a bigger diameter and a larger spatial separation. Since charge transport occurs via tunneling through the barriers, this leads to a significant increase in the resistance as observed. The difference in the critical temperature with the change in metal concentration ($T_m = 123\ °C$ for $f = 0.24$, $T_m = 135\ °C$ for $f = 0.27$, and $T_m = 143\ °C$ for $f = 0.31$) might reveal a competition process between the thermal activation and the change in microstructure which has an opposite effect on the resistance. The higher the metal filling factor, the lower the resistance of the sample, assuming that the sample with the higher filling factor has nanoparticles which are bigger in size and closer to each other. In this range the thermal expansion of the matrix can also contribute to the increase in the resistance but its effect is expected to be much smaller.

In the third part of the curve above T_max, an abrupt drop of the resistance is observed due to nanoparticle arrays rearrangement due to a decrease in polymer viscosity, which is exponentially depend on the temperature. Thus the nanoparticles will be able to arrange themselves easily by the help of an electric field. That means the induced field will be able to drive other nanoparticles into the gap between two neighboring nanoparticles. Hence, the resistance gets lower. However, as a result of this strong electric field the nanoparticles encounter unstable condition which leads to the minimization of energy by the change in shape, which is assisted by the high temperature. Thus the surface mobility favors the shape of the nanoparticles to change from elliptical to spherical [98]. This change of the shape leads to a change in the gap of the nanoparticles that causes an increase in the resistance up to $185\,°C$.

For samples above the percolation in figure 7.7(bottom), the charge transport mechanisms governing the electrical conductivity are completely different from those controlling electrical transport in samples below the percolation threshold. For $T < 90\ °C$ the resistance is practically independent from the temperature, due to the existence of a conductive path network. In contrast with samples at $f < f_c$, the resistance of the samples above the percolation threshold drops at a critical temperature and continues to decrease up to $180\,°C$ up on annealing. For

higher filling factors with larger cluster size, the heating process did not show to a significant change in microstructure due to a limited diffusion of nanoparticles. Nevertheless the slight structural changes begin to be evident and channels with lower resistivity are created so that the resistance decreases in all samples and finally reaches to saturation. Therefore, the relaxation of the polymer matrix is the main parameter to causing the drop in the resistance [38, 39, 165].

During the cooling process, all investigated samples show similar behavior in which the resistance remains constant or slightly decreases with cooling temperature. This suggests that the existence of polymer contraction and reduced phonon scattering on clusters up on a decrease in temperature.

7.3 Conclusion

Nanocomposites of Teflon and Nylon containing three dimensionally distributed Au or Ag nanoclusters were prepared by vapor phase co-deposition. Their electrical conductivity was investigated as a function of metal concentration, and the percolation threshold was found at $f = 0.42$ and $f = 0.32$ for Teflon and Nylon composites, respectively.

The I-V characteristics of Teflon composites with Au nanoclusters exhibited different responses for various Au concentrations. For samples with $f < f_c$, the conductivity caused by the field induced tunneling was found to be very small due to the relatively large gap between the neighboring clusters. Whereas for $f > f_c$ with smaller distance between clusters, the electrical field induced across the electrodes is enough to create the electrons to tunnel from one cluster to the neighboring cluster. Thus, the slope of the I-V curve showed an increase with the metal filling factor. Moreover, the filed induced change of microstructure was evidenced due to the existence of break down voltage and a constant conductivity with a decrease in applied voltage. The break down voltage is inversely proportional to the metal filling factor.

Electrical conductivity measurements in the range $27 - 190\,^{\circ}C$ have been carried out on Nylon composites with various Au concentrations. Similarly, the resistance versus temperature curves was exhibited different trend for those samples with Au concentration below and above the percolation threshold. For sam-

ples with $f < f_c$, the heating process causes coalescence of metal nanoparticles into bigger particles more distant from each other, which leads to a significant increase in the resistance at a certain temperature T_m. For $T > T_m$, the resistance decreases with temperature due to the contraction in the matrix. For samples with $f > f_c$, the heating leads to the formation of a more conductive path between the electrodes and showed a large drop at T_m.

The understanding of the electrical behaviour of the nanocomposites can be used to prepare sensors or other devices with a well defined conductivity. Since the changes induced upon the first heating cycle are irreversible, it can be used to thermally treat a sample up to a certain temperature to induce a desired resistivity. The only caution is that the device must never exceed the maximum temperature used in the first heating cycle during operation.

8 Summary and Outlook

Studies of the plasmonic materials remain a hot, active and expanding field of science and technology. Moreover, manufacturing of novel nanocomposites, micro- and nanodevices with specific features require the development of powerful and flexible techniques to control and optimize their structural and physical properties. In this context, co-deposition of polymer molecules and metal atoms from two independent sources, as presented in this work, provides a simple way to manipulate the shape and distribution of metal clusters. This in turn allows the alternations of the optical and electrical properties. Vapor phase co-deposition of Au and Ag simultaneously with various polymers (Teflon, PAMS, Nylon, and PMMA) was successfully used to produce polymer/metal nanocomposites with a wide range of metal volume filling factor.

The growth of metallic nanoclusters in polymers is controlled by the strongly contrasting properties of the two materials. This leads to aggregation of the high cohesive metal with the formation of spherical nanoclusters in polymer matrix. The cluster distribution in the polymer matrix, and the size and shape of the individual clusters strongly depend on the condensation coefficient of the metal on the polymer surface. The condensation coefficient depends on the ratio of the deposition rates of metal and polymer, the metal-polymer combination, the substrate temperature and the nucleation density. Here, it has been observed that the condensation coefficient increases with an increase in the ratio of deposition rate of metal to polymer regardless of the metal-polymer combination. Moreover, increase of the substrate temperature during deposition leads to a decrease in the condensation coefficient up to the glass transition temperature of the polymer. Beyond the glass transition temperature the condensation coefficient increases again. Heat treatment during or after co-deposition leads to changes in the microstructure of the nanocomposites due to diffusion of metal nanoparticles in

the polymer. Post deposition annealing results in formation of larger and more spheroidal shaped clusters.

The optical properties of the composites are strongly related with the microstructure of the composites. The position, intensity and width of the particle plasmon resonance were determined as a function of the metal volume filling factor, cluster size, shape, distribution, interparticle separation, the type of metal and the surrounding dielectric medium. These factors are interdependent for composites produced by vapor phase co-deposition. The position of the metal particle resonance shows a large red shift with increasing filling factor f which corresponds to an increasing particle size and a decrease in interparticle distance. Changes of the optical properties of the nanocomposite films caused by a change of the surrounding dielectric medium were also observed. Shifts of the plasmon peak position to longer wavelengths were observed with increasing dielectric constants of the polymer matrices. These shifts are most clearly exhibited at low metal filling factors where size effects are less pronounced.

Changes of the microstructure of the composite film upon annealing allowed to demonstrate the effect of interparticle distance and size of the clusters on the plasmonic properties of the composites. As a result it was found that the peak wavelength of the plasmon band shifted towards a shorter wavelength with an increase in the temperature. This shift of the absorption maximum is mainly caused by an increase in the distance between the clusters by agglomeration during the heat treatment, which leads to a decrease in the number density of the clusters. The degree of this shift depends on the original microstructure, annealing temperature, and duration of the annealing.

Bimetallic nanostructures in polymers synthesized by using co-evaporation from three distinct sources show homogeneously distributed clusters in polymers. This work reports for the first time the synthesis of bimetallic nanoparticles dispersed in a polymer matrix via a co-evaporation approach. In comparison with other techniques this allows to produce high filling bimetallic clusters and free choice of alloy composition. Bimetallic nanoclusters in polymers exhibit a plasmon band which is mainly dependent on the alloy composition. For gold/silver bimetallic clusters the single plasmon band position is shifted linearly to longer wavelength with an increase in the gold fraction. In contrast, the Ag-Cu nanoclus-

ters in a polymer matrix show a single and double plasmon band for $f < 40\,\%$ and $f > 40\,\%$, respectively. This is related with the formation of bimetallic alloy or core-shell nanoparticles in polymers.

Also the electrical properties of nanocomposites consisting of three dimensionally distributed Au or Ag nanoclusters in Teflon and Nylon matrices were investigated. The electrical conductivity was investigated as a function of metal filling factor, and the percolation threshold was found at $f = 0.42$ and $f = 0.32$ for Teflon and Nylon composites, respectively. The IV characteristics of Teflon composites containing Au nanoclusters showed different responses for various Au concentrations. For samples with $f < f_c$, the conductivity caused by the field induced tunneling was found to be very small due to the relatively very large gap between the neighboring clusters. Whereas for $f > f_c$ exhibiting a smaller distance between the clusters, the electrical field induced across the electrodes is large enough to allow the electrons to tunnel from one cluster to a neighboring cluster. Nevertheless, electromigration causes a breakdown at a certain voltage which was found to be almost inversely proportional to the metal filling factor. Similarly, the resistance versus temperature curves showed different trend for samples with Au concentrations below and above the percolation threshold, respectively. The changes in the resistance were explained in terms of a change in the microstructure due to rearrangement of the clusters, and polymer contraction above the temperature of the main transition in the polymer.

In conclusion, the physical co-deposition of metal and polymer has been found as a promising technique to produce metal-polymer nanocomposites for various applications. These composites have the potential to be used for technological applications such as tunable color filters, coatings, high density capacitors and so on. In a layer by layer geometry, they can be used as absorbers at multiple and tunable wavelengths and as Bragg reflectors. Moreover, composites with bimetallic structures can be very useful for tuning the optical absorbance over a broad range. Finally, the composites can be used as bifunctional materials, if the constituents of the bimetallic cluster combine different properties such as plasmonic absorption and magnetism.

Bibliography

[1] Biswas, A., Aktas, O. C., Schürmann, U., Saeed, U., Zaporojtchenko, V., Faupel, F. and Strunskus, T., Tunable multiple plasmon resonance wavelengths response from multicomponent polymer-metal nanocomposite systems, *Applied Physics Letters*, 84: p. 2655 (**2004**).

[2] Ouyang, J., Chu, C.-W., Szmanda, C. R., Ma, L. and Yang, Y., Programmable polymer thin film and non-volatile memory device, *Nature Materials*, 3: p. 918 (**2004**).

[3] Greve, H., Pochstein, C., Takele, H., Zaporojtchenko, V., Faupel, F., Gerber, A., Frommberger, M. and Quandt, E., Nanostructured magnetic Fe-Ni-Co/Teflon multilayers for high frequency applications in the gigahertz range, *Applied Physics Letters*, 89: p. 242,501 (**2006**).

[4] Fan, F.-R. F. and Bard, A. J., Chemical, Electrochemical, Gravimetric, and Microscopic Studies on Antimicrobial Silver Films, *Journal of Physical Chemistry*, 106: p. 279 (**2002**).

[5] Hutter, E. and Fendler, J. H., Exploitation of localized surface plasmon resonance, *Advanced Materials*, 16: p. 1685 (**2004**).

[6] Kelly, K. L., Coronado, E., Zhao, L. L. and Schatz, G. C., The optical properties of metal nanoparticles: The influence of size, shape, and dielectric environment, *Journal of Physical Chemistry B*, 107: pp. 668–677 (**2003**).

[7] Beecroft, L. L. and Ober, C. K., Nanocomposite materials for optical applications, *Chemistry of Materials*, 9: pp. 1302–1317 (**1997**).

[8] Kreibig, U. and Vollmer, M., *Optical properties of metal clusters*, Springer Series in Materials Science, Vol. 25, Springer Verlag, Berlin-Heidelberg (**1995**).

[9] Quinten, M., The color of finely dispersed nanoparticles, *Applied Physics B*, 73: pp. 317–326 (**2001**).

[10] Biswas, A., Aktas, O. C., Kanzow, J., Saeed, U., Strunkus, T., Zaporojtchenko, V. and Faupel, F., Polymer-metal optical nanocomposites with tunable particle plasmon resonance prepared by vapor phase codeposition, *Materials Letters*, 58: pp. 1530–1534 (**2004**).

[11] Dirix, Y., Bastiaansen, C., Caseri, W. and Smith, P., Oriented Pearl-Necklace Arrays of Metallic Nanoparticles in Polymers: A New Route Toward Polarization-Dependent Color Filters, *Advanced Materials*, 11: p. 223 (**1999**).

[12] Stegeman, G. I. and Wright, E. M., All-optical waveguide switching, *Optical and Quantum Electronics*, 22: p. 95 (**1990**).

[13] Haes, A. J. and Duyne, R. P. V., A nanoscale optical biosensor: Sensitivity and selectivity of an approach based on the localised surface plasmon resonance spectroscopy of triangular silver nanoparticles, *Journal of American Chemical Society*, 124: p. 10,596 (**2002**).

[14] Haes, A. J., Zou, S., Schatz, G. C. and Duyne, R. P. V., A nanoscale optical biosensor: The long range distance dependence of the localised surface plasmon resonance of noble metal nanoparticles, *Journal of Physical Chemistry B*, 108: p. 109 (**2004**).

[15] Rand, B. P., Peumans, P. and Forrest, S. R., Long-range absorption enhancement in organic tandem thin-film solar cells containing silver nanoclusters, *Journal of Applied Physics*, 96: p. 7519 (**2004**).

[16] Bockstaller, M. R. and Thomas, E. L., Optical properties of polymer-based photonic nanocomposite materials, *Journal of Physical Chemsitry*, 107: p. 10,017 (**2003**).

[17] Convertino, A., Capobianchi, A., Valentini, A. and Cirillo, E. N. M., A New Approach to Organic Solvent Detection: High-Reflectivity Bragg Reflectors Based on a Gold Nanoparticle/Teflon-like Composite Material, *Advanced Materials*, 15: p. 1103 (**2003**).

[18] Schürmann, U., Takele, H., Zaporojtchenko, V. and Faupel, F., Optical and electrical properties of polymer metal nanocomposites prepared by magnetron co-sputtering, *Thin Solid Films*, 515: p. 801 (**2006**).

[19] Nie, S. and Emory, S. R., Probing single molecules and single nanoparticles by surface enhanced raman scattering, *Science*, 275: p. 1102 (**1997**).

[20] Henglein, A., Small-Particle Research: Physicochemical properties of extremely small colloidal metal and semicconductor particles, *Chemical Review*, 89: pp. 1861–1873 (**1989**).

[21] Ershov, B. G. and Henglein, A., Optical spectrum and some chemical properties of colloidal thallium in aqueous solution, *Journal of Physical Chemistry*, 97: pp. 3434–3436 (**1993**).

[22] Raether, H., *Surface Plasmons*, Springer-Verlag Berlin (**1988**).

[23] Barnes, W. L., Dereux, A. and Ebbesen, T. W., Surface plasmon subwavelength optics, *Nature*, 424: p. 824 (**2003**).

[24] Noguez, C., Surface plasmons on metal nanoparticles: The influence of shape and physical environment, *Journal of Physical Chemistry C*, 111: p. 3806 (**2007**).

[25] Ung, T., Liz-Marzan, L. M. and Mulvaney, P., Optical properties of thin films of Au@SiO2 particles, *Journal of Physical Chemistry B*, 105: pp. 3441–3452 (**2001**).

[26] Underwood, S. and Mulvaney, P., Effect of the solution refractive index on the color of gold colloids, *Langmuir*, 10: pp. 3427–3440 (**1994**).

[27] Kreibig, U. and Genzel, L., Optical absorption of small metallic particles, *Surface Science*, 156: pp. 678–700 (**1985**).

[28] Kreibig, U., Electronic properties of small silver particles: the optical constants and their temperature dependence, *Journal of Physics F: Metal Physics*, 4: p. 999 (**1974**).

[29] Link, S. and El-Sayed, M. A., Size and temperature dependence of the plasmon absorption of colloidal gold nanoparticles, *Journal of Physical Chemistry B*, 103: pp. 4212–4217 (**1999**).

[30] Winey, K. I. and Vaia, R. A., Polymer Nanocomposites, *MRS Bulletin*, 32: p. 314 (**2007**).

[31] Link, S. and El-Sayed, M. A., Spectral properties and relaxation dynamics of surface plasmon electronic oscillations in gold and silver nanodots and nanorods, *Journal of Physical Chemistry*, 103: pp. 8410–8426 (**1999**).

[32] Liz-Marzan, L. M., Tailoring surface plasmons through the morphology and assembly of metal nanoparticles, *Langmuir*, 22: pp. 32–41 (**2006**).

[33] Boyd, R. W., Gehr, R. J., Fischer, G. L. and Sipe, J. E., Nonlinear optical properties of nanocomposite materials, *Pure Applied Optics*, 5: pp. 505–512 (**1996**).

[34] Martinu, L., Optical response of composite plasma polymer/metal films in the effective medium approach, *Solar Energy Materials*, 15: pp. 21–35 (**1987**).

[35] Heilmann, A., *Metal-Polymer Nanocomposites*, chapter 6, p. 183200, Wiley Interscience (**2005**).

[36] Kreibig, U., *Handbook of Optical Properties Volume II: Optics of Small Particles, Interfaces, and Surfaces*, chapter 7, pp. 145–190, CRC press (**1996**).

[37] Kelly, K. L., Jensen, T. R., Lazarides, A. A. and Schatz, G. C., *Metal nanoparticles: Synthesis, Characterization and Applications*, chapter 4, pp. 89–118, Marcel Dekker Ltd (**2001**).

[38] Perrin, J., Despax, B. and Kay, E., Optical properties and microstructure of gold-fluorocarbon-polymer composite films, *Physical Review B*, 32: p. 719 (**1985**).

[39] Biederman, H., Martinu, L., Slavinska, D. and Chudacek, I., Plasma deposition and properties of composite metal/polymer and metal/hard carbon films, *Pure and Applied Chemistry*, 60: p. 607 (**1988**).

[40] Cohen, R. W., Cody, G. D., Coutts, M. D. and Abeles, B., Optical properties of granular silver and gold films, *Physical Review B*, 8: p. 3689 (**1973**).

[41] Shalaev, V. M., *Optical Properties of Nanostructured Random Media*, Springer-Verlag, Berlin Heidelberg New York (**2002**).

[42] Starke, T. K. H., Johnston, C., Hill, S., Dobson, P. and Grant, P. S., The effect of inhomogeneities in particle distribution on the dielectric properties of composite films, *Journal of Physics D: Applied Physics*, 39: pp. 1305–1311 (**2006**).

[43] Kochergin, V., Zaporojtchenko, V., Takele, H., Faupel, F. and Föll, H., Improved effective medium approach: Application to metal nanocomposites, *Journal of Applied Physics*, 101: p. 024,302 (**2007**).

[44] Kochergin, V. Y., *Optical Properties of Metamaterials Based on Porous Semiconductors and Nanocomposites-Theoretical Considerations and Experiments*, Ph.D. thesis, Christian-Albrechts University of Kiel (**2006**).

[45] Cusack, N. E., *The Physics of Structurally Disordered Matter: An Introduction*, Adam Hilger, Bristol and Philadelphia (**1987**).

[46] Isichenko, M. B., Percolation, statistical topography, and transport in random media, *Review Modern Physics*, 64: p. 961 (**1992**).

[47] Garboczi, E. J., Snyder, K. A., Douglas, J. F. and Thorpe, M. F., Geometrical percolation threshold of overlapping ellipsoids, *Physical Review E*, 52: p. 819 (**1995**).

[48] Mattox, D., *Handbook of Physical vapour Deposition Processing*, Noyes Publications (**1998**).

[49] Mahan, J. E., *Physical Vapor Deposition of Thin Films*, Wiley-VCH (**January 2000**).

[50] Ohring, M., *Materials Science of Thin Films*, Academic Press, second edition (**2002**).

[51] Link, S., Wang, Z. L. and El-Sayed, M. A., Alloy formation of gold-silver nanoparticles and the dependence of the plasmon absorption, *Journal of Physical Chemistry*, 103: pp. 3529–3533 (**1999**).

[52] Moskovits, M., Srnova-Sloufova, I. and Vlckova, B., Bimetallic Ag-Au nanoparticles: Extracting meaningful optical constants from the surface-plasmon extinction spectrum, *Journal of Chemical Physics*, 116: p. 10,435 (**2002**).

[53] Hodak, J. H., Henglein, A., Giersig, M. and Hartland, G. V., Laser-Induced Inter-Diffusion in AuAg Core-Shell Nanoparticles, *Journal of Physical Chemistry B*, 104: pp. 11,708–11,718 (**2000**).

[54] Schierhorn, M. and Liz-Marzan, L. M., Synthesis of bimetallic colloids with tailored intermetallic separation, *Nano Letters*, 2: pp. 13–16 (**2002**).

[55] Mulvaney, P., Giersig, M. and Henglein, A., Electrochemistry of multilayer colloids: Preparation and absorption spectrum of gold-coated silver particles, *Journal of Physical Chemistry*, 97: p. 7061 (**1993**).

[56] Papavassiliou, G. C., Surface plasmons in small Au-Ag alloy particles, *Journal of Physics F: Metal Physics*, 6: p. L103 (**1976**).

[57] Cottancin, E., Lerme, J., Gaudry, M., M. Pellarin, J.-L. V. and Broyer, M., Size effects in the optical properties of AuAg embedded clusters, *Physical Review B*, 62: p. 5179 (**2000**).

[58] Gonzalo, J., D, B., Afonso, C. N. and Barnes, J. P., Optical response of mixed Ag-Cu nanocrystals produced by pulsed laser deposition, *Journal of Applied Physics*, 96: p. 5163 (**2004**).

[59] Baba, K., Okuno, T. and Miyagi, M., Silver-gold compound metal island films prepared by using a two-step evaporation method, *Applied Physics Letters*, 62: p. 437 (**1993**).

[60] Buttry, D. A. and Ward, M. D., *Chemical Review*, 92: p. 1355 (**1992**).

[61] Sauerbey, G., *Z. Physics*, 155: p. 206 (**1959**).

[62] Thran, A., Kiene, M., Zaporojtchenko, V. and Faupel, F., Condensation Coefficients of Ag on Polymers, *Physical Review Letters*, 82: pp. 1903–1906 (**1999**).

[63] Zaporojtchenko, V., Behnke, K., Strunskus, T. and Faupel, F., Determination of the condensation coefficients of metals on polymer surfaces, *Surface Science*, 454-456: pp. 412–416 (**2000**).

[64] Zaporjtchenko, V., Behnke, K., Strunskus, T. and Faupel, F., Condensation coefficients of noble metals on polymers: a novel method of determination by x-ray photoelectron spectroscopy, *Surface and Interface Analysis*, 30: pp. 439–443 (**2000**).

[65] Fuchs, E., Oppolzer, H. and Rehme, H., *Particle Beam Microanalysis*, VCH, Weinheim (**1990**).

[66] Reimer, H., *Transmission Electron Microscopy*, Springer Verlag, Berlin (**1984**).

[67] Faupel, F., Zaporojtchenko, V., Thran, A., Strunskus, T. and kiene, M., *Metal Diffusion in Polymers and on Polymer Surfaces*, chapter 7, p. 333, William Andrew (**2004**).

[68] Faupel, F., Thran, A., Keine, M., Strunskus, T., Zaporojtchenko, V. and Behnke, K., *Diffusion of Metals in Polymers and During Metal/Polymer Interface Formation*, chapter 8, pp. 221–251, Springer-Verlag Berlin Heidelberg New York (**2003**).

[69] Yang, H. and Flymn, C., Growth of Alkali Halides from Molecular Beams: Global Growth Characteristics, *Physical Review Letter*, 62: p. 2476 (**1989**).

[70] Song, H., Ilegbusi, O. J. and Trakhtenberg, L. I., Modeling vapor deposition of metal/semiconductor-polymer nanocomposite, *Thin Solid Films*, 476: pp. 190–195 (**2005**).

[71] Zaporojtchenko, V., Strunskus, T., Behnke, K., Bechtolsheim, C. V., Kiene, M. and Faupel, F., Metal/Polymer interfaces with designes morphologies, *J. Adhesion Science Technology*, 14: pp. 467–490 (**2000**).

[72] Zaporojtchenko, V., Zekonyte, J., Biswas, A. and Faupel, F., Controlled growth of nano-size metal clusters on polymers by using VPD method, *Surface Science*, 532-535: pp. 300–305 (**2003**).

[73] Zaporojtchenko, V., Strunskus, T., Behnke, K. and Faupel, F., Controlled Nucleation and Growth of Noble Metals on Polymers, *Proc. EuroMat*, 9 (**1999**).

[74] Faupel, F., Thran, A., Zaporojtchenko, V., Kiene, M., T.Strunskus and Behnke, K., Nucleation, Growth, Interdiffusion, and Adhesion of Metal Films on Polymers, in *Stress-Induced Phenomena in Metallization* (**1999**).

[75] Zaporojtchenko, V., Erichsen, J., Zekonyte, J., Thran, A., Strunskus, T. and Faupel, F., *Metallization of Polymers 2*, chapter Adsorption of Noble Metal Atoms on Polymers, pp. 107–116, Kluwer Academic/Plenum Publishers (**2002**).

[76] Zaporojtchenko, V., Strunskus, T., Behenke, K., v. Bechtolsheim, C., Thran, A. and Faupel, F., Formation of metal-polymer interfaces by metal evaporation: influence of deposition parameters and defects, *Microelectronic Engineering*, 50: pp. 465–471 (**2000**).

[77] Erichsen, J., Dolgner, K., Zaporojtchenko, V. and Faupel, F., Glass transition temperature in thin polymer films determined by thermal discharge in X-ray photoelectron spectroscopy, *Macromolecules*, 37: p. 8813 (**2004**).

[78] Strunskus, T., Kiene, M., Willecke, R., Thran, A., v. Bechtolsheim, C. and Faupel, F., Chemistry, diffusion and cluster formation at metal-polymer interfaces, *Materials and corrosion*, 49: pp. 180–188 (**1998**).

[79] Akamatsu, K. and Deki, S., Dispersion of gold nanoparticles into a nylon 11 thin film during heat treatment: in situ optical transmission study, *Journal of Materials Chemistry*, 8: pp. 637–640 (**1998**).

[80] Akamatsu, K. and Deki, S., TEM Investigation and Electron Diffracation study on Dispersion of Gold Nanoparticles into a Nylon 11 Thin Film during Heat Treatment, *Journal of Colloid and Interface Science*, 214: pp. 353–361 (**1999**).

[81] Akamatsu, K., Tsuboi, N., Hatakenaka, Y. and Deki, S., In Situ Spectroscopic and Microscopic study on Dispersion of Ag Nanoparticles in Polymer Thin Films, *Journal of Physical Chemistry B*, 104: p. 10,168 (**2000**).

[82] Faupel, F., *Metal diffusion during metallization of high-temperature polymers*, Mareel Dekker, New York (**1997**).

[83] Strunskus, T., Zaporojtchenko, V., Behnke, K., v. Bechtolsheim, C. and Faupel, F., Tailoring the Morphology of Metal/Polymer Interfaces, *Advanced Engineering Materials*, 2: p. 489 (**2000**).

[84] Faupel, F., Willecke, R., Thran, A., Kiene, M., Bechtolsheim, C. and Strunkus, T., Metal Diffusion in Polymers, *Defect and Diffusion Forum*, 143-147: pp. 887–902 (**1997**).

[85] Li, J.-L., Jia, J.-F., Liang, X.-J., Liu, X., Wang, J.-Z., Xue, Q.-K., Li, Z.-Q., Tse, J. S., Zhang, Z. and Zhang, S. B., Spontaneous Assembly of Perfectly Ordered Identical-Size Nanocluster Arrays, *Physical Review Letters*, 88: pp. 066,101–1 (**2002**).

[86] Behnke, K., Strunskus, T., Zaporojtchenko, V. and Faupel, F., Metal/Polymer Interfaces and Composite Materials Prepared by Vapor Phase Deposition, *Proc. MicroMat*, p. 1052 (**2000**).

[87] Faupel, F., Metal Diffusion in High-Temperature Polymers, *Advanced Materials*, 2: p. 266 (**1990**).

[88] Thran, A., Strunskus, T., Zaporojtchenko, V. and Faupel, F., Evidence of noble metal diffusion in polymers at room temperature and its retardation by a chromium barrier, *Applied Physics Letters*, 81: p. 244 (**2002**).

[89] Faupel, F., Strunskus, T., Kiene, M., Thran, A., v. Bechtolsheim, C. and Zaporojtchenko, V., Fundamental Aspects of Polymer Metallization, in *Materials Research Society Symposium* (**1998**).

[90] Maye, M. M., Zheng, W., Leibowitz, F. L., Ly, N. K. and Zhong, C.-J., Heating-Induced Evolution of Thiolate-Encapsulated Gold Nanoparticles: A Strategy for Size and Shape Manipulations, *Langmuir*, 16: pp. 490–497 (**2000**).

[91] Teransishi, T., Hasegawa, S., Shimizu, T. and Miyake, M., Heat-Induced Size Evolution of Gold Nanoparticles in the Solid State, *Advanced Materials*, 13: pp. 1699–1701 (**2001**).

[92] Marchi, G. D., Mattei, G., Mazzoldi, P., Sada, C. and Miotello, A., Two stages in kinetics of gold clusters in ion-implanted silica during isothermal annealing in oxidizing atmosphere, *Journal of Applied Physics*, 92: pp. 4249–4254 (**2002**).

[93] Takele, H., Schürmann, U., Greve, H., Paretkar, D., Zaporojtchenko, V. and Faupel, F., Controlled growth of Au nanoparticles in co-evaporated metal/polymer composite films and their optical and electrical properties, *European Physical Journal: Applied Physics*, 33: pp. 83–89 (**2006**).

[94] Takele, H., Greve, H., Pochstein, C., Zaporojtchenko, V. and Faupel, F., Plasmonic properties of Ag nanoclusters in various polymer matrices, *Nanotechnology*, 17: pp. 3499–3505 (**2006**).

[95] Chen, H. and Zuo, J. M., In-situ STEM observation of phase separation in ultrathin Ag/Cu alloy system, *Microscopy and Microanalysis*, 10: p. 816 (**2004**).

[96] See, K. C., Spicer, J. B., Brupbacher, J., Zhang, D. and Vargo, T. G., Modeling interband transitions in silver nanoparticle-fluoropolymer composites, *Journal of Physical Chemistry B*, 109: pp. 2693–2698 (**2005**).

[97] Joerger, R., Klaus, T. and Granqvist, C. G., Biologically produced silver-carbon composite materials for optically functional thin-film coatings, *Advanced Materials*, 12: p. 407 (**2000**).

[98] Martinu, L. and Biederman, H., Plasma deposited composite polymer-metal thin films and their optical characteristics, *Vacuum*, 36: p. 477 (**1986**).

[99] Akamatsu, K. and Deki, S., Characterization and optical properties of gold nanoparticles dispersed in nylon 11 thin films, *Journal of Materials Chemistry*, 7: pp. 1773–1777 (**1997**).

[100] Hazra, S., Gibaud, A. and Sella, C., Tunable absorption of Au-Al2O3 nanocermet thin films and its morphology, *Applied Physics Letters*, 85: p. 395 (**2004**).

[101] Salerno, M., Krenn, J., Lamprecht, B., Schider, G., Ditlbacher, H., Felidj, N., Leitner, A. and Aussenegg, F., plasmon polaritons in metal nanostructures: the optoelectronic route to nanotechnology, *Opto-Electronics Review*, 10: pp. 217–224 (**2002**).

[102] Antoine, R., Pellarin, M., Palpant, B., Broyer, M., Prevel, B., Galletto, P., Brevet, P. F. and Girault, H. H., Surface plasmon enhanced second harmonic response from gold clusters embedded in an alumina matrix, *Journal of applied physics*, 84: p. 4532 (**1998**).

[103] Lin, X. Z., Teng, X. and Yang, H., Direct synthesis of narrowly dispersed silver nanoparticles using a single-source precursor, *Langmuir*, 19: pp. 10,081–10,085 (**2003**).

[104] Halas, N., Playing with plasmons: tuning the optical resonant properties of metallic nanoshells, *MRS Bulletin*, 30: p. 362 (**2005**).

[105] Mafune, F., ya Kohno, J., Takeda, Y. and Kondow, T., Formation of gold nanonetworks and small gold nanoparticles by irradiation of intense pulsed laser onto gold nanoparticles, *Journal of Physical Chemistry*, 107: pp. 12,589–12,596 (**2003**).

[106] Mock, J. J., Smith, D. R. and Schultz, S., Local refractive index dependence of plasmon resonance spectra from individual nanoparticles, *Nano Letters*, 3: pp. 485–491 (**2003**).

[107] Caseri, W., Nanocomposites of polymers and metals or semiconductors: Historical background and optical properties, *Macromolecular Rapid Communication*, 21: pp. 705–722 (**2000**).

[108] Ferreira, F. F. and Fantini, M. C. A., Theoretical optical properties of composite metal-NiO films, *Journal of Physics D: Applied Physics*, 36: pp. 2386–2392 (**2003**).

[109] Krevelen, D. W. V., *Properties of Polymers*, Elsevier Science, Amsterdam (**1994**).

[110] McFarland, A. D. and Duyne, R. P. V., Single silver nanoparticles as real-time optical sensors with zeptomole sensitivity, *Nano Letters*, 3: pp. 1057–1062 (**2003**).

[111] Malinsky, M. D., Kelly, K. L., Schatz, G. C. and Duyne, R. P. V., Nanosphere Lithography: Effect of substrate on the localised surface plasmon resonance spectrum of silver nanoparticles, *Journal of Physical Chemistry B*, 105: pp. 2343–2350 (**2001**).

[112] Haynes, C. L. and Duyne, R. P. V., Nanosphere Lithography: A versatile nanofabrication tool for studies of size-dependent nanoparticle optics, *Journal of Physical Chemistry B*, 105: pp. 5599–5611 (**2001**).

[113] Xu, G., Tazawa, M., Jin, P., Nakao, S. and Yoshimura, K., Wavelength tuning of surface plasmon resonance using dielectric layers on silver island films, *Applied Physics Letters*, 82: p. 3811 (**2003**).

[114] Templeton, A. C., Pietron, J. J., Murray, R. W. and Mulvaney, P., Solvent refractive index and core charge influences on the surface plasmon absorbance of alkanethiolate monolayer-protected gold clusters, *Journal of Physical Chemistry B*, 104: pp. 564–570 (**2000**).

[115] Heilmann, A., Werner, J., Stenzel, O. and Homilius, F., Changes of optical and electrical properties of plasma polymer-metal composite films during thermal annealing, *Thin Solid Films*, 246: p. 77 (**1993**).

[116] Roiz, J., Oliver, A., Munoz, E., Rodriguez-Fernandez, L., Hernandez, J. M. and Cheang-Wong, J. C., Modification of the optical properties of Ag-implanted silica by annealing in two different atmospheres, *Journal of Applied Physics*, 95: p. 1783 (**2004**).

[117] Su, K.-H., Wei, Q.-H. and Zhang, X., Interparticle coupling effects on plasmon resonances of nanogold particles, *Nano Letters*, 3: pp. 1087–1090 (**2003**).

[118] Mulvaney, P., Not all that is gold does glitter, *MRS Bulletin*, p. 1009 (**2001**).

[119] Atay, T., Song, J.-H. and Nurmikko, A. V., Strongly interacting plasmon nanoparticle pairs: From dipole-dipole interaction to conductively coupled regime, *Nano Letters*, 4: pp. 1627–1631 (**2004**).

[120] Rechberger, W., Hohenau, A., A. Leitner, J. R. K., Lamprecht, B. and Aussenegg, F. R., Optical properties of two interacting gold nanoparticles, *Optics Communications*, 220: pp. 137–141 (**2003**).

[121] Akamatsu, K., Kawamura, T., Nabika, H., Deki, S., Strunskus, T. and Faupel, F., Effect of composition and structure of gold/copper bimetallic nanoparticles on dispersion in polymer thin films, *Journal of Materials Chemistry*, 12: pp. 1–6 (**2002**).

[122] De, G., Gusso, M., L. Tapfer, M. C., F. Gonella, G. M., Mazzoldi, P. and Battaglin, G., Annealing behavior of silver, copper, and silver-copper nanoclusters in a silica matrix synthesized by the sol-gel technique, *Journal of Applied Physics*, 80: p. 6734 (**1996**).

[123] Iwamoto, M., Kuroda, K., Zaporojtchenko, V., Hayashi, S. and Faupel, F., Production of gold nanoparticles-polymer composite by quite simple method, *European Physical Journal D: Applied Physics*, 24: p. 365 (**2003**).

[124] Hirai, M. and Kumar, A., Wavelength tuning of surface plasmon resonance by annealing silver-copper nanoparticles, *Journal of Applied Physics*, 100: p. 014,309 (**2006**).

[125] Rossi, G., Rapallo, A., Mottet, C., Fortunelli, A., Baletto, F. and Ferrando, R., Magic polyicosahedral core-shell clusters, *Physical Review Letters*, 93: p. 105,503 (**2004**).

[126] Chen, D.-H. and Chen, C.-J., Formation and characterization of Au-Ag bimetallic nanoparticles in water-in-oil microemulsions, *Journal of Materials Chemistry*, 12: p. 1557 (**2002**).

[127] Liu, J.-H., Wang, A.-Q., Chi, Y.-S., Lin, H.-P. and Mou, C.-Y., Synergistic effect in an Au-Ag alloy nanocatalyst: co oxidation, *Journal of Physical Chemistry B*, 109: pp. 40–43 (**2005**).

[128] k. Teo, B., Keating, K. and Kao, Y.-H., Observation of plasmon frequency in the optical spectrum of Au(18)Ag(20) cluster: The beginning of the collective phenomenon characteristic of the bulk?, *Journal of American Chemical Society*, 109: pp. 3494–3495 (**1987**).

[129] Sönnichsen, C., Franzl, T., Wilk, T., von Plessen, G. and Feldmann, J., Plasmon resonances in large noble-metal clusters, *New Journal of Physics*, 4: pp. 93.1–93.8 (**2002**).

[130] Quinten, M., Heilmann, A. and Kiesow, A., Refined interpretation of optical extinction spectra of nanoparticles in plasma polymer films, *Applied Physics B*, 68: pp. 707–712 (**1999**).

[131] Mallin, M. P. and Murphy, C. J., Solution-phase synthesis of sub-10 nm Au-Ag alloy nanoparticles, *Nano Letters*, 2: pp. 1235–1237 (**2002**).

[132] Mulvaney, P., Surface plasmon spectroscopy of nanosized metal particles, *Langmuir*, 12: pp. 788–800 (**1996**).

[133] Wei, S. H., Mbaye, A. A., Ferreira, L. G. and Zunger, A., First-principles calculations of the phase diagrams of noble metals: Cu-Au, Cu-Ag, and Ag-Au, *Physical Review B*, 36: p. 4163 (**1987**).

[134] Murani, A. P., Localized enhancement effects in Pd-Ag alloys, *Physical Review Letters*, 33: p. 91 (**1974**).

[135] Liz-Marzan, L. M., Giersig, M. and Mulvaney, P., Synthesis of nanosized gold-silica core-shell particles, *Langmuir*, 12: pp. 4329–4335 (**1996**).

[136] Hao, E., Li, S., Bailey, R. C., Zou, S., Schatz, G. C. and Hupp, J. T., Optical properties of metal nanoshells, *Journal of Physical Chemistry B*, 108: pp. 1224–1229 (**2004**).

[137] Oldenburg, S. J., Jackson, J. B., Westcott, S. L. and Halas, N. J., Infrared extinction properties of gold nanoshells, *Applied Physics Letters*, 75: p. 2897 (**1999**).

[138] Sun, Y., Wiley, B., Li, Z.-Y. and Xia, Y., Synthesis and optical properties of nanorattles and multiple-walled nanoshells/nanotubes made of metal alloys, *Journal of American Chemical Society*, 126: pp. 9399–9406 (**2004**).

[139] Liu, M. and Guyot-Sionnest, P., Synthesis and optical characterization of Au/Ag core/shell nanorods, *Journal of Physical Chemistry B*, 108: pp. 5882–5888 (**2004**).

[140] Faupel, F., Willecke, R. and Thran, A., Diffusion of Metals in Polymers, *Materials Science and Engineering, Reports: A Review Journal*, R22: pp. 1–55 (**1998**).

[141] Shibata, T., Bunker, B., Henglein, A., Zhang, Z., Meisel, D., Cheong, S. K. and Boyanov, M., The size-dependent alloying effect of metallic nanoparticles at room temperature, *Journal of American Chemical Society*, 124: pp. 1189–11,996 (**2002**).

[142] Sosa, I. O., Noguez, C. and Barrera, R. G., Optical properties of metal nanoparticles with arbitrary shapes, *Journal of physical chemistry B*, 107: pp. 6269–6275 (**2003**).

[143] Gonzalez, A. L. and Noguez, C., Influence of morphology on the optical properties of metal nanoparticles, *Journal of Computational Theory and Nanoscience*, 4: pp. 231–238 (**2007**).

[144] Mohamed, M. B., Ismail, K. Z., Link, S. and El-Sayed, M. A., Thermal reshaping of gold nanorods in micelles, *Journal of Physical Chemistry B*, 102: pp. 9370–9374 (**1998**).

[145] Link, S., Burda, C., Nikoobakht, B. and El-Sayed, M. A., Laser-induced shape changes of colloidal gold nanorods using femtosecond and nanosecond laser pulses, *Journal of Physical Chemistry B*, 104: pp. 6152–6163 (**2000**).

[146] Yu, Y.-Y., Chang, S.-S., Lee, C.-L. and Wang, C. R. C., Gold Nanorods: Electrochemical synthesis and optical properties, *Journal of Physical Chemistry B*, 101: p. 6661 (**1997**).

[147] Perez-Juste, J., Correa-Duarte, M. A. and Liz-Marzan, L. M., Silica gels with tailored, gold nanorod-driven optical functionalities, *Applied Surface Science*, 226: pp. 137–143 (**2004**).

[148] Mandal, S. K., Roy, R. K. and Pal, A. K., Effect of particle shape distribution on the surface plasmon resonance of Ag-SiO2 nanocomposite thin films, *Journal of Physics D: Applied Physics*, 36: pp. 261–265 (**2003**).

[149] Link, S., Mohamed, M. B. and El-Sayed, M. A., Simulation of the optical absorption spectra of gold nanorods as a function of their aspect ratio and the effect of the medium dielectric constant, *Journal of Physical Chemistry B*, 103: pp. 3073–3077 (**1999**).

[150] Nikoobakht, B. and El-Sayed, M. A., Preparation and growth mechanism of gold nanorods (NRs) using seed-mediated growth method, *Chemistry of Materials*, 15: pp. 1957–1962 (**2003**).

[151] Hrach, R., Novak, S. and Svec, M., Correlation between morphology and transport properties of composite films: Charge transport in composites, *Applied Surface Science*, 252: p. 5516 (**2006**).

[152] Abeles, B., Sheng, P., Coutts, M. and Arie, Y., *Adv. Phys*, 24: p. 407 (**1975**).

[153] Pecharroman, C. and Esteban-Betegon, F., New percolative BaTiO3-Ni composites with a high and frequency-independent dielectric constant, *Advanced Materials*, 13: p. 1541 (**2001**).

[154] Huang, C., Zhang, Q. M., deBotton, G. and Bhattacharya, K., All-organic dielectric-percolative three-component composite materials with

high electromechanical response, *Applied Physics Letters*, 84: p. 4391 (**2004**).

[155] Huang, C. and Zhang, Q., Enhanced dielectric and electromechanical responses in high dielectric constant all-polymer percolative composites, *Advanced Functional Materials*, 14: p. 501 (**2004**).

[156] Heilmann, A., *Polymer Films with Embedded Metal Nanoparticles*, Springer-Verlag Berlin Heidelberg (**2003**).

[157] Chelidze, T. and Guequen, Y., Pressure-induced percolation transitions in composites, *Journal of Physics D: Applied Physics*, 31: pp. 2877–2885 (**1998**).

[158] Pecharroman, C. and Moya, J. S., Experimental evidence of a giant capacitance in insulator-conductor composites at the percolation threshold, *Advanced Materials*, 12: p. 294 (**2000**).

[159] Sivarmakrishnan, S., Chia, P.-J., Yee-Chia Yeo, L.-L. C. and Ho, P. K.-H., Controlled insulator-to-metal transformation in printable polymer composites with nanometal clusters, *Nature materials*, 6: p. 149 (**2006**).

[160] Bloor, D., Donnelly, K., Hands, P. J., Laughlin, P. and Lussey, D., A metal-polymer composite with unusual properties, *Journal of Physics D: Applied Physics*, 38: pp. 2851–2860 (**2005**).

[161] Kiesow, A., Morris, J. E., Radehaus, C. and Heilmann, A., Switching behavior of plasma polymer films containing silver nanoparticles, *Journal of Applied Physics*, 94: p. 6988 (**2003**).

[162] Canet, P., Laurent, C., Akinnifesi, J. and Despax, B., Dielectric properties of gold-containing plasma-polymerized thin films, *Journal of Applied Physics*, 72: p. 2423 (**1992**).

[163] Sheng, P., Fluctuation-induced tunneling conduction in disordered materials, *Physical Review B*, 21: p. 2180 (**1980**).

[164] Gusev, A. A. and Guseva, O. A., Voltage breakdown in random composites, *Advanced Engineering Materials*, 5: p. 713 (**2003**).

[165] Augelli, V., Ligonzo, T., Masellis, M. C., Muscarella, M. F., Schiavulli, L. and Valentini, A., Electrical properties of gold-polymer composite films, *Journal of Applied Physics*, 90: p. 1362 (**2001**).

List of Figures

List of Publications

1. **H. Takele**, U. Schürmann, H. Greve, D. Paretkar, V. Zaporojtchenko, and F. Faupel, Controlled growth of Au nanoparticles in co-evaporated metal/polymer composite films and their optical and electrical properties, Eur. Phys. J. Appl. Phys., 33 (2006) 83.

2. **H. Takele**, H. Greve, C. Pochstein, V. Zaporojtchenko, and F. Faupel, Plasmonic properties of Ag nanoclusters in various polymer matrices, Nanotechnology, 17 (2006) 3499.

3. **H. Takele**, S. Jebril, T. Strunskus, V.Zaporojchenko, R. Adelung, and F. Faupel, Tuning of electrical and structural properties of metal-polymer nanocomposite films prepared by co-evaporation technique, Appl. Phys. A 92 (2008) 345.

4. **H. Takele**, A. Kulkarni, S. Jebril, V.S.K. Chakravadhanula, C. Hanisch, T. Strunskus, V. Zaporojtchenko, and F. Faupel, Plasmonic properties of vapour deposites polymer composites containing Ag nanoparticles and their changes upon annealing, J. Phys. D: Appl. Phys. 41 (2008) 125409.

5. **H. Takele**, V.S. K. Chakravadhanula, C. Hanisch, H. Greve, M. Elbahri, V. Zaporojtchenko, and F. Faupel, Tuning of plasmonic properties in polymer nanocomposites with Ag-Au and Ag-Cu bimetallic nanoclusters, submitted.

6. U. Schürmann, **H. Takele**, V. Zaporojtchenko, F. Faupel, Optical and electrical properties of polymer metal nanocomposites prepared by magnetron co-sputtering, Thin Solid Films, 515 (2006) 801.

7. U. Schürmann, W. Hartung, **H. Takele**, V. Zaporojtchenko, and F. Faupel, Controlled synthesis of Ag-polytetrafluoroethylene nanocomposite thin

films by co-sputtering from two magnetron sources, Nanotechnology, 16 (2005) 1078.

8. V. Kochergin, V. Zaporojtchenko, **H. Takele**, F. Faupel, and H. Föll, Improved effective medium approach: Application to metal nanocomposites, J. Appl. Phys., 101 (2007) 024302.

9. H. Greve, C. Pochstein, **H. Takele**, V. Zaporojtchenko, and F. Faupel; A. Gerber, M. Frommberger, and E. Quandt, Nanostructured magnetic Fe-Ni-Co/Teflon multilayers for high-frequency applications in the gegahertz range, Appl. Phys. Lett., 89 (2006) 242501.

10. V. Zaporojtchenko, U. Schürmann, H. Greve, **H. Takele**, A. Biswas, C. Pochstein, M. Frommberger, E. Quandt, A. Avasthi, R. Podschun, and F. Faupel, Polymer-metal nanocomposites for functional applications, VDI-Berichte 1920 Nanofair 2005, accepted (2006).

11. A. Biswas, R. Kunz, O. C. Aktas, M. Elbahri, R. Adelung, **H. Takele**, U. Saeed, U. Schürmann, V. Zaporojtchenko, and F. Faupel, Arrays of wire-like microstructures of Ag with visible wavelength transparent plasmonic response at near-ultraviolet and midinfrared regions, Appl. Phys. Lett., 85 (2004) 1952.